
Attosecond photoelectron spectroscopy of electron transport in solids

Elisabeth Magerl



München 2011

Attosecond photoelectron spectroscopy of electron transport in solids

Elisabeth Magerl

Dissertation
an der Fakultät für Physik
der Ludwig-Maximilians-Universität
München

vorgelegt von
Elisabeth Magerl
aus Wien, Österreich

München, den 28. 2. 2011

Erstgutachter: Prof. Dr. Ferenc Krausz

Zweitgutachter: Prof. Dr. Armin Scrinzi

Tag der mündlichen Prüfung: 31.3.2011

To my parents.

Abstract

Time-resolved photoelectron spectroscopy of condensed matter systems in the attosecond regime promises new insights into excitation mechanisms and transient dynamics of electrons in solids. This timescale became accessible directly only recently with the development of the attosecond streak camera and of laser systems providing few-cycle, phase-controlled laser pulses in the near-infrared, which are used to generate isolated, sub-femtosecond extreme-ultraviolet pulses with a well-defined timing with respect to the near-infrared pulse. Employing these pulses, the attosecond streak camera offers time resolutions as short as a few 10 attoseconds. In the framework of this thesis, a new, versatile experimental apparatus combining attosecond pulse generation in gases with state of the art surface science techniques is designed, constructed, and commissioned. Employing this novel infrastructure and the technique of the attosecond transient recorder, we investigate transport phenomena occurring after photoexcitation of electrons in tungsten and rhenium single crystals and show that attosecond streaking is a unique method for resolving extremely fast electronic phenomena in solids. It is demonstrated that electrons originating from different energy levels, i.e. from the conduction band and the $4f$ core level, are emitted from the crystal surface at different times. The origin of this time delay, which is below 150 attoseconds for all studied systems, is investigated by a systematic variation of several experimental parameters, in particular the photon energy of the employed attosecond pulses. These experimental studies are complemented by theoretical studies of the group velocity of highly-excited electrons based on *ab initio* calculations. While the streaking technique applied on single crystals can provide only information about the relative time delay between two types of photoelectrons, the absolute transport time remains inaccessible. We introduce a scheme of a reference clock signal, i.e. a well-defined electronic state localised at the crystal surface, which enables us to measure the absolute time delay of photoelectrons, and present first results obtained on this system.

Zusammenfassung

Zeitaufgelöste Photoelektronen Spektroskopie von Systemen kondensierter Materie auf der Attosekunden-Skala versprechen neue Erkenntnisse über Anregungsmechanismen und transiente Dynamik von Elektronen in Festkörpern. Diese Zeitskala wurde erst unlängst mit der Entwicklung der Attosekunden-Streak Kamera und von phasenstabilen Laserpulsen im nahen Infrarot, bestehend aus einzelnen, wenigen Zyklen des elektrischen Feldes, zugänglich gemacht. Diese Laser können isolierte Pulse im extremen Ultraviolett mit einer Dauer von weniger als einer Femtosekunde erzeugen, welche einen wohldefinierten zeitlichen Zusammenhang zum Puls im nahen Infrarot aufweisen. Damit ermöglicht die Attosekunden-Streak Kamera eine extrem hohe Zeitauflösung von einigen 10 Attosekunden. Im Rahmen der vorliegenden Arbeit wird ein neuer, flexibler Versuchsaufbau für Messungen von Elektronendynamik in Festkörpern auf der Attosekundenskala geplant, konstruiert und in Betrieb genommen. Dieser Aufbau kombiniert die Erzeugung von Attosekunden-Pulsen mit hochmodernen Methoden der Oberflächentechnologie. Mithilfe dieser neuartigen Infrastruktur werden elektronische Transportphänomene in Wolfram- und Rhenium-Einkristallen nach vorangegangener Photo-Anregung untersucht, und es wird gezeigt, dass die Methode des Streakings es auf einzigartige Weise erlaubt, ultra-schnelle Elektronendynamik in Festkörpern zu untersuchen. Es wird gezeigt, dass photo-angeregte Elektronen aus unterschiedlichen Energieniveaus, und zwar aus dem Leitungsband und dem $4f$ Zustand, zu unterschiedlichen Zeiten von der Kristalloberfläche emittiert werden. Durch systematische Variation von mehreren Parametern, im Speziellen der Photonenenergie des Attosekunden-Pulses, wird die physikalische Ursache dieser Zeitdifferenz, die kleiner als 150 Attosekunden ist, untersucht. Diese Messungen werden durch theoretische Studien der Gruppengeschwindigkeit, die auf *ab initio* Berechnungen beruhen, von hoch angeregten Elektronen ergänzt. Streaking-Experimente an Einkristallen ermöglichen lediglich die Messung eines relativen Zeitversatzes zwischen zwei Photoelektronen, die aus unterschiedlichen Niveaus angeregt werden, nicht der absoluten Dauer des Elektronentransports. Die Einführung eines zeitlichen Referenzsignals, realisiert durch einen elektronischen Zustand, der an der Kristalloberfläche lokalisiert ist, erlaubt Zugang zum absoluten Zeitversatz, erste Messungen an einem so gearteten System werden präsentiert.

Contents

Abstract	3
Zusammenfassung	5
1. Introduction	12
2. Time-resolved photoemission spectroscopy of solids	16
2.1. The photoelectric effect	16
2.1.1. Modeling photoemission	19
2.2. Conventional techniques for time-resolved photoemission spectroscopy . .	23
2.2.1. Core-hole clock spectroscopy	23
2.2.2. Time-resolved two-photon photoemission	24
2.3. Real-time photoemission spectroscopy with the attosecond transient recorder	25
3. Dynamics of the photoelectric effect	31
3.1. Theoretical description of attosecond time-resolved photoemission of solids	31
3.2. Schemes to investigate the relative time delay between two photoelectrons	34
3.3. Schemes to reference the absolute time delay between two photoelectrons	35
4. Experimental setup	38
4.1. The laser system	38
4.1.1. High harmonic generation and single attosecond pulses	38
4.1.2. Ultrashort pulse generation	41
4.1.3. Carrier-envelope phase stabilisation	42
4.2. Ultrahigh-vacuum attosecond beamline	45
4.2.1. High harmonic generation	47
4.2.2. XUV diagnostics	49

4.2.3.	Single attosecond pulse selection	52
4.2.4.	Electron detection schemes	56
4.2.5.	Vacuum layout	57
4.2.6.	Preparation tools and sample control	63
5.	Theoretical tools and data analysis	65
5.1.	Introduction to density functional theory	65
5.1.1.	Obtaining the Kohn-Sham Hamiltonian	65
5.1.2.	Solving the Kohn-Sham equations	69
5.1.3.	Calculated quantities	71
5.2.	Data evaluation	71
5.2.1.	Center of mass analysis	72
5.2.2.	Peak fitting	74
5.2.3.	Spectrogram retrieval	75
6.	Streaking experiments of solids	78
6.1.	Materials	78
6.1.1.	Tungsten and rhenium single crystals	78
6.1.2.	Xenon adlayer	80
6.2.	Relative delay between conduction band and core state electrons in clean metals	81
6.2.1.	Measurements of the influence of the XUV photon energy	84
6.2.2.	Simulation of the influence of the XUV photon energy with density functional theory	90
6.2.3.	Measurements of the influence of the probing NIR intensity	96
6.2.4.	Measurements of the influence of the sample temperature	99
6.3.	Absolute delay between core state electrons in rhenium covered with a monolayer of xenon	99
6.3.1.	Simulation of the combined system with density functional theory	100
6.3.2.	Measurements of the absolute delay	104
7.	Conclusions and outlook	108
A.	TOF detector calibration	113

B. XUV mirrors and filters	118
Bibliography	119
Data archiving	128
Acknowledgements	133
Curriculum vitae	135

1. Introduction

Time-resolved spectroscopy of electronic and nuclear photo-response in condensed matter has enabled researches to gain understanding of the dynamic behaviour of atomic and electronic structures. As shorter timescales are accessed, more fundamental processes can be investigated: lattice vibrations in a crystal persist over many picoseconds, the breaking of chemical bonds in molecules was found to be on the order of 100 femtoseconds (A. Zewail, Nobel laureate 1999 [1]). Electronic motion happens on an even faster timescale - the thermalisation of hot electrons at the Fermi edge takes 20 – 250 femtoseconds [2], charge transfer times of an electron from an adsorbed atom to the substrate are as short as 320 attoseconds, the latter one was measured in the energy domain [3]. Other fundamental effects, like screening of charges [4], image charge creation [5], build-up of plasmons [6], or build-up of non-thermalised hot electron distributions are expected to happen on an attosecond timescale as well. Although lifetimes of electronic states on the attosecond scale can be inferred from energy-resolved measurements, time-resolved measurements are necessary in order to completely capture transient electron dynamics.

The first real-time observation of electron dynamics on the attosecond timescale in solids was accomplished by A. L. Cavalieri and colleagues [7] in 2007. In a first proof of principle measurement, they excited electrons in a tungsten single crystal from the conduction band and a core state with a sub-fs extreme-ultraviolet pulse (see figure 1.1 (a, b)). In a semi-classical picture [8], both types of electrons travel to the surface after their photoexcitation, where they are probed by a few-cycle phase-controlled near-infrared pulse at the moment of their escape from the sample (c, d). The electric field of the near-infrared pulse modulates the kinetic energy of the photoelectrons depending on their release time from the crystal. Although both electrons are excited at the same time, it was found in the experiment that they escape at different times from the surface, therefore their kinetic energy signatures showed a small time delay Δt . In this experiment, the core state electrons were found to be delayed with respect to the

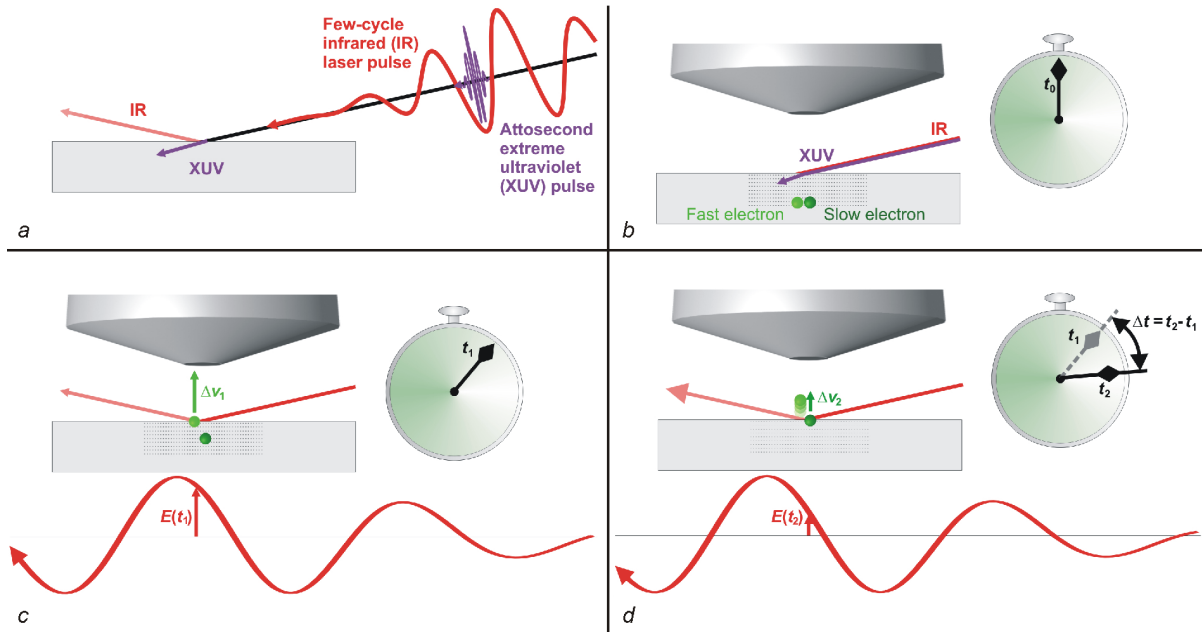


Figure 1.1.: Sketch of an attosecond streaking experiment in a solid state sample (adapted from [12]). After excitation by an ultrashort extreme-ultraviolet pulse (a) electrons travel to the surface (b) and escape from the sample at different times (c, d). The delay, Δt , can be probed with a phase-controlled near-infrared pulse, and is on the order of 100 as.

conduction band electrons by 110 ± 70 attoseconds.

Since then, this extremely small time difference has been explained with several different theoretical approaches, like the band structure of the crystal [7], the different spatial localisation of the two electrons [9, 10], and a classical transport model [11]. Although the calculated value of the delay is on the same order of magnitude in all models, their physical assumptions and included parameters deviate from each other and partly contradict each other. One aim of this thesis was to obtain further experimental and theoretical insight into the physical origins of the observed effect. In order to test some of the assumptions made in the theoretical models, several experimental parameters were varied systematically. One of the models, relying on the band structure of the investigated system, was further pursued by utilising density functional theory.

The advanced measurements which were carried out within this thesis called for a new experimental setup. Therefore, a novel attosecond beamline was designed, built, and commissioned in the framework of this thesis. In contrast to previous attosecond

setups [13, 14], this beamline was explicitly designed to investigate condensed matter systems. It combines generation and characterisation of sub-femtosecond pulses with schemes to clean, prepare, and characterise solid state samples in an ultra-high vacuum environment. Additionally, the highly flexible design allows for changing pulse properties, sample, detector, and detection geometry and is so far the only fully equipped solid state beamline for attosecond experiments on the world.

The structure of this thesis is as follows: Chapter 2 introduces the photoelectric effect and its physical models. Commonly used techniques for time-resolved photoelectron spectroscopy and their applications are discussed. The concept of an attosecond transient recorder and its application to solid state photoelectron spectroscopy is presented, and its main advantages compared to conventional techniques are clarified.

Chapter 3 reviews the first time-resolved measurement of the dynamics of the photoelectric effect and possible physical origins of the observed timing. Measurements to clarify the underlying physical processes of the relative delay in photoemission in single crystals and a concept to gain access to absolute emission times are devised.

Chapter 4 deals with the tools and techniques which were used to measure the dynamics of the photoelectric effect. Generation of high-harmonic radiation and single attosecond pulses is reviewed, the employed few-cycle laser system is briefly described. The beamline which was designed and set up in the framework of this thesis is introduced and thoroughly discussed.

The theoretical concept of modelling the observed effect and extracting delays from a measurement are introduced in chapter 5. The underlying theorems of density functional theory, which was used to simulate electronic transport in a bandstructure, are explained. This chapter also summarises the methods which were used to analyse the measured data.

The results and investigated systems are presented in chapter 6. Two different single crystal samples, tungsten and rhenium, were thoroughly investigated. The influence of different external parameters, like excitation energy, probing intensity, and temperature is discussed. Simulations based on band structure calculations done with density functional theory are used to explain the observed effects. Possible reasons for deviations between model and experiment are discussed. Additionally, a combined system of rhenium and a xenon monolayer was investigated. First results allow an estimate of the absolute transport time in a solid state system.

Finally, conclusions on the obtained results are drawn and an outline of future experiments is given in chapter 7.

In connection with this thesis, the following publications and conference contributions were obtained:

A flexible apparatus for attosecond photoelectron spectroscopy of solids and surfaces

E. Magerl, S. Neppl, A.L. Cavalieri, E. Bothschafter, M. Stanislowski, Th. Uphues, M. Hofstetter, U. Kleineberg, J.V. Barth, D. Menzel, F. Krausz, R. Ernstorfer, R. Kienberger, P. Feulner
submitted to Review of Scientific Instruments.

First attosecond pulse control by multilayer mirrors above 100 eV photon energy

M. Hofstetter, M. Schultze, M. Fiess, A. Guggenmos, J. Gagnon, E. Magerl, E. Bothschafter, R. Ernstorfer, R. Kienberger, E.M. Gullikson, F. Krausz, and U. Kleineberg
Postdeadline paper in the proceedings of the Ultrafast Phenomena XVII, 2010.

Attosecond Photoelectron Spectroscopy of Solids

E. Magerl, A.L. Cavalieri, R. Ernstorfer, S. Neppl, N. Karpovicz, M. Stanislowski, E. Bothschafter, J.V. Barth, P. Feulner, R. Kienberger, F. Krausz
Talk held at the Spring meeting of the DPG, March 2010, Regensburg, Germany.

Attosecond Photoelectron Spectroscopy in Solids

E. Magerl, A.L. Cavalieri, R. Ernstorfer, S. Neppl, P. Feulner, N. Mller, Th. Uphues, V.S. Yakovlev, A. Baltuska, B. Horvath, M. Drescher, U. Kleineberg, P.M. Echenique, R. Kienberger, D. Menzel, U. Heinzmann, F. Krausz
Poster presentation given at the conference on Ultrafast Surface Dynamics (USD6), July 2008, Banz monastery, Germany.

2. Time-resolved photoemission spectroscopy of solids

2.1. The photoelectric effect

One of the most important physical mechanisms for spectroscopy of condensed matter is the photoelectric effect [15]. Figure 2.1 illustrates the concept and the geometry of the measurement: A photon excites an electron from an occupied state in a sample into empty states above the Fermi level. Within the reduced zone scheme of band structure representation the transition is a vertical (or direct) one: The momentum of the photon can be neglected for photon energies $\lesssim 200$ eV, and no other excitations, which could shift the final momentum, take place. If the electron's final energy is higher than the vacuum level, it leaves the crystal and can be detected. Its kinetic energy distribution (with ν being the photon frequency, E_i the electron binding energy with respect to the Fermi level, and W the work function of the sample)

$$E_{kin} \leq h\nu - E_i - W \quad (2.1)$$

is an image of the joint density of states of occupied and unoccupied states of the crystal. The spectra show sharp peaks originating from core states with a well defined binding energy, wider features arise if a broad band is probed. The peaks are superimposed on a background consisting of secondary electrons which have lost energy due to inelastic scattering events in the sample.

In addition to the kinetic energy of the electrons, their angular distribution can be analysed as well. The wavevector of the detected electrons in vacuum, \vec{K} , is related to the kinetic energy via

$$|\vec{K}| = \sqrt{\frac{2mE_{kin}}{\hbar^2}} \quad \begin{array}{l} K_{\parallel} = K \sin \vartheta \\ K_{\perp} = K \cos \vartheta \end{array} , \quad (2.2)$$

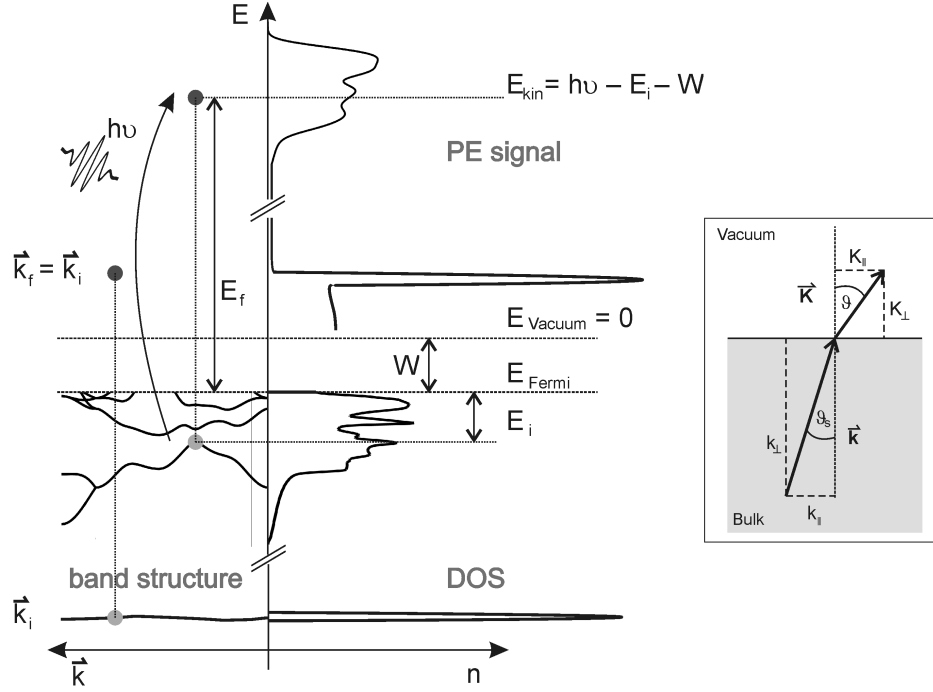


Figure 2.1.: Schematic sketch of photoemission spectroscopy. Electrons are excited from a solid state sample by photons, their kinetic energy distribution, which is characteristic of the sample, the detection angle, and the photon energy, is measured.

where m is the electron mass and ϑ the angle of the electron's wavevector in vacuum relative to the crystal surface normal. Because of the two-dimensional symmetry of the system the parallel component of the electron's wavevector is conserved across the surface to within a reciprocal lattice vector \vec{G}_{\parallel} pointing along the surface:

$$\vec{K}_{\parallel} = \vec{k}_{\parallel} + \vec{G}_{\parallel}, \quad (2.3)$$

where \vec{k} denotes a wavevector inside the sample. This allows for mapping two-dimensional projections of band structures with photoemission spectroscopy. The normal component of the wavevector inside the sample remains unknown. It depends not only on the surface potential step but also on the shape of the band structure in the sample and cannot be derived without further knowledge of the observed system.

Photoelectron spectroscopy is highly surface sensitive: Electrons which were excited by

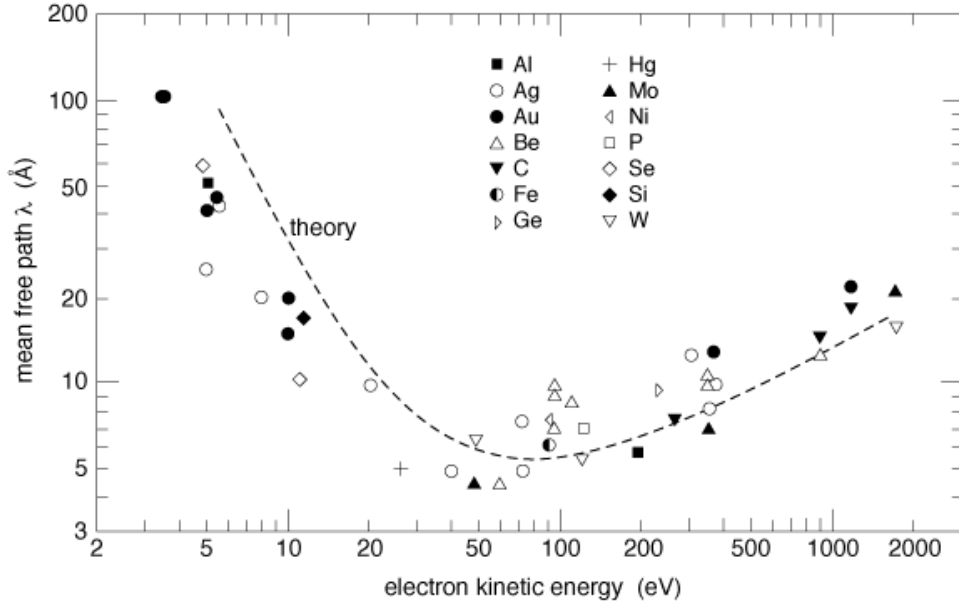


Figure 2.2.: Energy dependence of the electron inelastic mean free path of several elements and a theoretical fit [16].

a photon can scatter with both the lattice and other electrons, the latter being the main contribution [17]. If the scattering event is inelastic, the photoexcited electron alters its energy and does not contribute to the primary photoelectron peak anymore. In a semiclassical picture, the inelastic scattering can be described with a constant scattering rate, which translates itself in a velocity dependent and therefore also energy dependent, inelastic mean free path λ of the electrons. The probability of escaping the sample starting at a distance l from the surface without energy loss is proportional to [18]

$$P(l) \propto \exp\left(-\frac{l}{\lambda(E)}\right). \quad (2.4)$$

Integrating this equation shows that 63% of the total non-scattered photoelectrons origin from a surface region of $1 \cdot \lambda$. Figure (2.2) shows the inelastic mean free path (IMFP) λ of electrons for a broad range of kinetic energies and different samples [16], this graph is usually referred to as the “universal curve” of photoemission spectroscopy. The IMFP is on the order of some ten Ångstroms with a minimum of less than 10 Å at energies around 80 eV. The similar behaviour of different materials results from the fact that electron-electron scattering happens predominantly at the Fermi-edge, where

the electron density is nearly a constant for most conducting materials. Due to the small escape depth, photoemission spectroscopy requires extremely well prepared, clean surfaces whose properties have to be maintained during the measurement. This is only possible under ultrahigh vacuum conditions: Kinetic gas theory tells us that the amount of particles Δn hitting an area A per time interval t depends on the total number of particles per volume N and their mean velocity \bar{v}

$$\frac{\Delta n}{tA} = \frac{N\bar{v}}{4} = \frac{p}{4k_B T} \sqrt{\frac{8k_B T}{\pi m_{gas}}}. \quad (2.5)$$

A dimensionless sticking coefficient $0 < S < 1$ is introduced to quantify the percentage of impinging atoms which adsorb on the surface. If we assume a sticking coefficient of 1, and a coverage of $\Delta n/A \approx 6 \cdot 10^{18} \text{ m}^{-2}$ corresponding to one monolayer, we can rewrite equation 2.5 to the number of monolayers n_{mono} which are created at a pressure p (in mbar) during a time t (in s):

$$n_{mono} = pt \cdot 0.67 \cdot 10^6 \quad (2.6)$$

One monolayer assembles within one second if the pressure is in the range of 10^{-6} mbar and obscures the photoelectron signal of the sample. Even though the sticking coefficient usually is smaller than 1, pressures below 10^{-9} mbar are necessary to preserve the original surface for more than one hour and to allow acquisition of high quality data.

2.1.1. Modeling photoemission

An accurate theoretical treatment of photoelectron spectroscopy has to deal with photoemission within quantum mechanics. The main formula governing photoemission is Fermi's golden rule, which describes the transition probability w_{fi} between an initial state $|\Psi_i\rangle$ and a final state $|\Psi_f\rangle$ with an interaction Hamiltonian \mathfrak{H} within first order perturbation theory [19]

$$w_{fi} \propto |\langle \Psi_f | \mathfrak{H} | \Psi_i \rangle|^2 \delta(E_f - E_i - h\nu) = m_{fi} \delta(E_f - E_i - h\nu). \quad (2.7)$$

Energy conservation is ensured with the delta-distribution. In principle, the exact photocurrent can be derived from (2.7) if the correct many-body wavefunctions Ψ_f and Ψ_i and the Hamiltonian are known. However, as this is often mathematically not feasible, several assumptions are made to simplify the problem. The electron wavefunctions

are usually modeled as one-electron states in an effective potential, the exact shape of the wavefunctions is derived from stationary solutions of the Schrödinger equation in a static periodic lattice potential. This approach is justified in case only single electrons are excited and the investigated effects take place on timescales longer than the many-electron response of the system. Two models are normally used to describe photoemission, the three-step-model and the one-step-model. The three-step-model [8] is a phenomenological approach and breaks apart the process into three incoherent steps: excitation of the electron in a final state inside the sample, transport through the crystal, and escape through the surface barrier. The one-step-model is a rigorous description of the effect, it matches the initial state bulk wavefunction with the detected final state wavefunction [20, 21]. Scattering events in the bulk or at the surface are completely contained in the final state wavefunction.

In the three-step-model, both initial and final state are assumed as one-electron wavefunctions, either as Bloch-states or as surface states. The excitation is assumed to be direct, the momentum of the photon is neglected, and the Bloch wavevector can only change by a reciprocal lattice vector. Besides the conservation of energy and of the wavevector, selection rules are applied as well. They are equivalent to the atomic case, where the difference in angular momentum of initial and final state has to compensate the angular momentum of the photon. In a solid, the rules are more complicated and are derived from symmetry operations of the lattice, but the underlying concept is still the same. After the excitation, the internal electron current density can be expressed as

$$I_{int} = \sum_{f,i} m_{f,i} f(E_i) (1 - f(E_f)) \delta(E_f - E_i - h\nu) , \quad (2.8)$$

where the transition matrix element $m_{f,i}$ weights the contribution of the specific transition f, i and the Fermi distributions $f(E_i)$, $1 - f(E_f)$ ensure that the initial state is occupied and the final one unoccupied.

The photoelectrons propagate then in the crystal and reach the surface either with their initial energy or with a lower one. As discussed above, the main mechanism responsible for energy loss is electron-electron scattering. This is described phenomenologically with the IMFP λ , which depends on the energy of the electron and on the sample material, and which can be calculated accurately via the imaginary part of the dielectric function. Although it is specific for each material, a very general analytical expression depending on the valence electron density could be found [22, 23]. The transport and scattering is

included in the three-step-model as scattering probability g depending on the mean free path $\lambda(E)$,

$$D(E) = g(\lambda(E)) . \quad (2.9)$$

The semi-classical picture of a photoelectron traveling to the surface requires assigning a classical velocity to the electrons. It can either be assumed to be a group velocity in a high-lying band or a free-electron like velocity, depending only on the kinetic energy. Usually, the free-electron dispersion relation is employed, the group velocity is only used for very low energy electrons. The reason for this is that the shape of high energy band structures is only known from calculations and that the exact velocity of the electron so far was not of significance for experiments. In the time-resolved experiments we perform, the transport plays a crucial role. The group velocity will therefore be employed in this work also for photoelectrons with relatively high kinetic energies around 100 eV.

The transmission of the photoelectrons through the surface can be considered as scattering from the surface atom potential with a translational symmetry. The parallel component of the electron's wavevector is conserved, the normal component is discontinuous. This implies a refraction of the electron beam path. The angle ϑ outside the sample is connected to the angle inside the sample, ϑ_s , via

$$\frac{\sin \vartheta}{\sin \vartheta_s} = \sqrt{\frac{E_{kin} + W}{E_{kin}}} , \quad (2.10)$$

where the surface was modeled with a potential step W , the work function (see figure 2.1. We see that the electrons are refracted away from the surface normal which implies a maximum angle inside the sample under which electrons can still escape from the crystal. The probability of escaping the surface barrier, $T(E, \vec{k})$, is simply described with $R \leq 1$ if the energy in direction of the surface is higher than the potential step and with 0 if it is lower [24]. This simple expression of the escape probability does not explicitly include any inelastic scattering at the surface. Surface excitations like surface plasmons are known to exist and are not included within this description. The complete emission current is then

$$I_{ex} \propto \sum_{f,i} m_{f,i} f(E_i) (1 - f(E_f)) \delta(E_f - E_i - h\nu) D(E) T(E, \vec{k}) . \quad (2.11)$$

The main shortcoming of the three-step-model lies in the complete neglect of any

interference between the three steps and in the incorrect final state. The final state usually is assumed to be an eigenstate of the lattice potential, whereas in reality the electron is detected in vacuum far away from the crystal. This is overcome within the one-step-model which includes a more realistic description of this wavefunction: In vacuum near the detector an asymptotic plane wave is used, obeying the conservation of parallel crystal momentum and including a transmission probability at the surface. Inside the sample it matches a crystal wave. This is equivalent to the process underlying low energy electron diffraction, LEED. This type of final state is therefore called time-reversed LEED state [25].

Although there exist programs for calculating photoemission in the one-step-model, the modeling done in this thesis relies on the three-step-model. The final states are not known exactly even for a conventional photoemission experiment. Here, a more complicated setup is used, involving two light pulses acting on the electrons. The special geometry does not alter the properties of the final states alone, but the Hamiltonian which describes the photoexcitation becomes more complicated as well. The second light pulse should act as a probe only outside the sample, but its influence on the excited state inside the sample and on the initial states cannot be evaluated easily. Additionally, transport can be handled in the three-step-model more easily and directly than in the one-step-model.

As already mentioned, both one-step- and three-step-model use steady-state wavefunctions in their calculations. The excitation is assumed to be instantaneous, as well as electronic many-body responses as screening, image charge creation or plasmon formation. Additionally, the crystal lattice and the electronic band structure are described in a static way. On the timescale of a few attoseconds, it is not clear if these descriptions are still valid. Calculations on plasmon formation indicate that the electronic response of the system happens on a similar timescale as the observed delay of photoelectrons [6]. Moreover, the picture of a static band structure might not be valid, simulations indicate that a timescale of a few 100 attoseconds is too short for a bandstructure to manifest itself: A photoexcited electron with a high kinetic energy of ≥ 60 eV is not affected by the crystal potential [9]. However, a thorough theoretical description of time-dependent photoemission on the attosecond timescale is not worked out today. Therefore, in this thesis steady state approximations are used to describe the observed effects in a first step.

2.2. Conventional techniques for time-resolved photoemission spectroscopy

Depending on the investigated effect and its timescale, various techniques of time-resolved photoelectron spectroscopy have been developed. Two of the most commonly used techniques resolving ultrafast processes in solids, core-hole clock spectroscopy and time-resolved two-photon photoemission, will be briefly discussed. We will point out their main drawbacks concerning measurements on a sub-femtosecond timescale and will introduce the streaking technique which enables us to observe sub-femtosecond electron dynamics in real time.

2.2.1. Core-hole clock spectroscopy

Core-hole clock spectroscopy utilises precisely known decay times of an atomic core hole as reference for sub-femtosecond electron dynamics in a condensed matter system [26]. This energy-resolving technique is mostly used to investigate charge transfer times from adsorbate atoms to the electronic valence band continuum of the substrate. The physical principle is outlined in figure 2.3 (a). An x-ray pulse lifts a core electron into an excited eigenstate of the atom. The core hole will predominantly decay being filled with an electron from an energetic low lying shell, the excess energy is transferred to a third electron which leaves the system and is detected. Its kinetic energy depends on the dynamics of the initially excited electron: If this electron is still localised in the atom, its energy is well defined and the excess electron will gain the energy difference between the exciting light pulse and the level separation of core and excited state. If the initially excited electron has already left the atomic system and has decayed to a delocalised state in the continuum, the excess electron can be described as a normal Auger electron at fixed kinetic energy.

Although electron transfer times of less than 3 fs [27] down to 320 as [3] were measured with this method it is intrinsically limited to a narrow range of systems. The core hole decay time has to match the time scale of the observed effect which restricts the number of possible samples and transitions. Additionally, dynamics in single crystal systems without adsorbate cannot be accessed with this method.

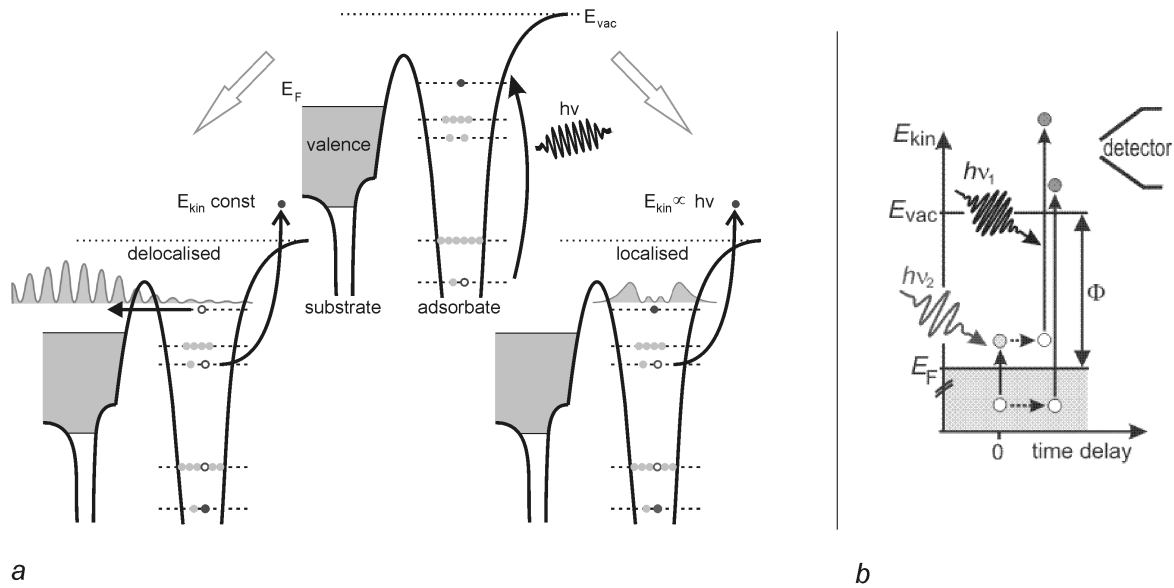


Figure 2.3.: Principle of a core-hole clock (a, adapted from [3]) and TR-2PPE measurement (b, from [33]).

2.2.2. Time-resolved two-photon photoemission

Time-resolved two-photon photoemission (TR-2PPE, for reviews see [28, 29]) is a pump-probe technique used to investigate unpopulated states between the Fermi energy and the vacuum level. This method has attracted particular interest with the availability of short laser pulses. Thermalisation times of hot electrons (250 - 20 fs [2]), lifetimes of image states (360 - 40 fs [30, 31]) and the motion of an adsorbed atom on a surface (bond-breaking times of 160 fs [32]) are among the many effects that have been investigated.

The basic technique is depicted in figure 2.3 (b): A pump pulse excites an electron to an intermediate level above the Fermi edge, a time delayed probe pulse lifts the electron to its final state above the vacuum level where it is detected. Depending on the exact geometry of the experiment and the detection scheme different information can be extracted. If the signal is angularly resolved the dispersion of the probed intermediate state can be mapped. The lifetime of the intermediate state is encoded in the peak intensity recorded at varying delay between pump and probe. Dephasing times of the intermediate state can be measured if pump and probe pulse have the same frequency

(monochromatic 2PPE), the excitation order of two or more peaks is accessible with pump and probe pulses of different colors (bichromatic 2PPE).

This method is restricted to excitation energies of less than the workfunction. 2PPE is a second-order process and is therefore much weaker than direct photoemission which has to be avoided. Highlying states above the vacuum level cannot be probed. The achievable time resolution of this technique is limited so far by the available pulse lengths in the near-infrared (NIR) and ultraviolet (UV) range. The shortest measured NIR pulses extend over 3.3 fs [34], in the UV range the limit lies at 2.8 fs [35].

2.3. Real-time photoemission spectroscopy with the attosecond transient recorder

One way to extend conventional time resolved photoelectron spectroscopy is based on the attosecond transient recorder (ATR), or attosecond streak camera, which was previously used to study the gas phase [36]. An isolated sub-fs extreme-ultraviolet (XUV) light pulse triggers the photoelectric effect while the electrical field of a few-cycle NIR pulse acts as a probe sensitive to the emission time of the photoelectron. The first step of extending this technique to solids was done by L. Miaja-Avila and colleagues in 2006 [37]. Recently, with this method they could resolve the xenon $4d(-1)$ core level lifetime of a xenon-platinum system to be 7.1 ± 1.1 fs [38]. As they used XUV pump pulses which last much longer than the period of the NIR probing field, their time-resolution is limited to the femtosecond scale. We will show that with this technique sub-fs resolution can only be achieved using isolated pump pulses with a duration of less than half a period of the probing NIR field.

In order to model the streaking process, we neglect the influence of the probe on the system prior to photoionisation and assume the electron to be a point-like particle which is excited into the continuum in an infinitely short period of time. In a first approximation, the Coulomb potential of the ionised core acting on the photoexcited electron can be neglected (strong field approximation, [39, 40]) and the motion of the free electron with a charge $-e = -1.6 \cdot 10^{-19}$ C in the NIR field, $\vec{\mathcal{E}}(t)$, is described with classical equations of motion [41].

$$\ddot{\vec{x}}(t) = \frac{-e}{m} \vec{\mathcal{E}}(t) \quad (2.12)$$

By integration we obtain

$$\begin{aligned}\vec{v}(t) &= \frac{-e}{m} \int_{t_0}^t dt' \vec{\mathcal{E}}(t') + \vec{v}_0 \\ &= \frac{e}{m} \vec{\mathcal{A}}(t) + \vec{v}_0 - \frac{e}{m} \vec{\mathcal{A}}(t_0).\end{aligned}\quad (2.13)$$

If we look at the final velocity, \vec{v} , of the electron when it is detected, meaning we let t go to infinity, the first term in the last line of (2.13) vanishes, and the initial velocity of the electron gets modified proportional to the vector potential $\vec{\mathcal{A}}(t_0)$ of the NIR laser field at the moment of the electron release. The final velocity of the electron is different from its initial one only if it is released during the NIR pulse, otherwise it does not absorb any radiation.

We rewrite equation (2.13) in terms of the kinetic energy of the detected electron

$$\begin{aligned}E_{kin} = \frac{m |\vec{v}|^2}{2} &= \frac{m}{2} (v_0^2 + \mathcal{A}^2(t_0) - 2v_0\mathcal{A}(t_0) \cos(\beta)) \\ &= \frac{m}{2} \left(v_0^2 + \frac{\mathcal{A}^2(t_0)}{2} \cos(2\gamma) \pm \mathcal{A}(t_0)v_0 \cos(\gamma) \sqrt{1 - \frac{\mathcal{A}^2(t_0)}{v_0^2} \sin^2(\gamma)} \right) \\ &= E_0 + 2U_p(t_0) \cos(2\gamma) \pm \alpha_L \sqrt{8E_0U_p(t_0)} \cos(\gamma).\end{aligned}\quad (2.14)$$

Here, we have chosen the coordinate system in a way that the NIR field is polarised along the x-axis (inset in figure 2.4). β is the angle between the initial velocity and the laser vector potential, which is rewritten to γ , the angle between the final (detected) velocity and the vector potential, α_L is a factor of $\sqrt{1 - 2U_p/E_0 \sin^2(\gamma)}$. E_0 is the initial kinetic energy. U_p is the ponderomotive energy,

$$U_p(t) = \frac{e^2 \mathcal{E}^2(t)}{4m \omega^2} = \frac{e^2 \mathcal{E}_0^2(t)}{4m \omega^2} \sin^2(\omega t + \phi_{CEP}), \quad (2.15)$$

the quiver energy of the electron in the external NIR field, with $\mathcal{E}_0(t)$ being the envelope of the NIR pulse, ω its angular frequency, and ϕ_{CEP} the phase between the carrier and the envelope. U_p is on the order of a fraction of an eV for the NIR intensities on the investigated sample ($\approx 5 \cdot 10^{11}$ W/cm² at 800 nm). Compared to the initial kinetic energy due to the XUV pulse, which is a few tens of eV, the contribution of the ponderomotive energy is negligible. We can therefore neglect the second term in the last line of (2.14) and set $\alpha_L \approx 1$. If we now put the detector along the laser polarisation, $\gamma = 0$, the kinetic energy reduces to

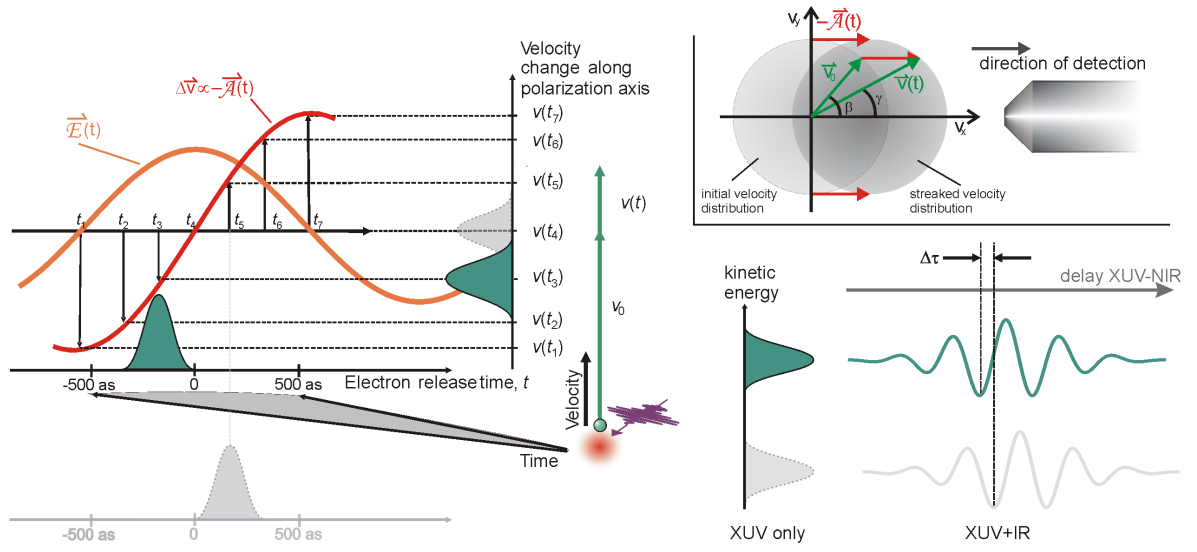


Figure 2.4.: Mapping of the electron release time to a velocity shift in a streaking experiment and the corresponding geometry (inset). Depending on the vector potential of the streaking field at the moment of release, electrons experience a shift of their velocity, which can be used to measure a delay $\Delta\tau$ of their emission times (adapted from [41, 13]).

$$E_{kin} = E_0 + \sqrt{8E_0 U_p(t_0)}. \quad (2.16)$$

The influence of the NIR pulse results in a modulation of the electron's kinetic energy: The release time t_0 of the electron is translated into an energy shift. Figure 2.4 shows how this shift can be used to resolve electron dynamics on a sub-femtosecond timescale. If t_0 is varied systematically by delaying the two pulses with respect to each other, the kinetic energy of the electron will trace out the NIR vector potential. Two electrons released at different times due to intrinsic dynamics of the probed system will result in two traces of the vector potential which are shifted by the delay in emission. This unique mapping of time to energy, resulting in a sub-fs time resolution, is only possible if the emission of the electron wave packet is restricted to less than a half-cycle of the NIR probe field. In case of longer emission times or longer XUV pulses, the energetically overlapping portions of the wave packet interfere and sidebands of the NIR laser are created [42].

In reality, we do not deal with a point-like particle, but with an electron wave packet which reflects both the properties of the exciting XUV pulse and the excitation dynamics of the system. As a consequence, it is rather described with an initial time-dependent momentum distribution $n_e(\vec{p}_i, t)$. The deflection of the final momentum distribution due to the NIR vector potential reads then

$$\sigma(\vec{p}) = \int_{\mathbb{R}} dt n_e \left(\vec{p} - \frac{e}{c} \vec{A}(t), t \right). \quad (2.17)$$

Instead of a narrow delta-peak a broad feature is measured whose width depends on both the initial electron distribution and the XUV properties. Usually, in gas phase systems, an instantaneous response of the electrons to the XUV excitation and discrete energy levels can be assumed. Figure 2.5 (a) shows the streaking effect on an electron bunch centered at two consecutive zero transitions of the NIR vector potential, using a Fourier transform limited XUV pulse. Due to the finite temporal width of the electron bunch the strength and sign of the NIR field varies over the bunch length. Electrons in the trailing edge will be accelerated, while electrons in the leading edge are decelerated. The energy width will therefore be broader than for the NIR-free case. At the next zero transition, the sign of the vector potential is reversed, resulting in deceleration in the trailing edge and acceleration in the leading edge of the electron bunch. The resulting distribution is again broadened, but its shape and width is exactly the same as for the previous zero crossing (if the gradient of the electrical field is also the same).

The situation with the initial momentum distribution featuring a linear chirp is illustrated in figure 2.5 (b). The mechanism for acceleration and deceleration in the trailing and leading edges of the electron remains the same, but in contrast to the chirp-free situation, the broadening of the peak is now different. In one case, the chirp and the effect of the NIR field add up, while they partly compensate in the other case. The resulting peak will therefore display a different width for consecutive zero-crossings of the vector potential.

A theory of the streaking effect in the gas phase was developed during the last years. Within certain approximations, both the NIR and XUV pulses can be characterised completely [43, 44, 45, 46]. The extension of this technique to condensed matter introduces new challenges not only to the experimental side but also to the interpretation of the obtained data. Instead of single, atomic energy levels, a complicated band structure is involved when solids are investigated. Each excited

electron is interacting not only with the laser pulses, but also with the collective response of the system. Furthermore, electrons originating from the broad conduction band result in a photoelectron peak consisting of incoherent contributions of the individual initial states. Additionally, the observed electrons are excited in layers very close to the two-dimensional surface, which behaves slightly different compared to the three-dimensional bulk due to lattice relaxation and surface reconstruction, and whose

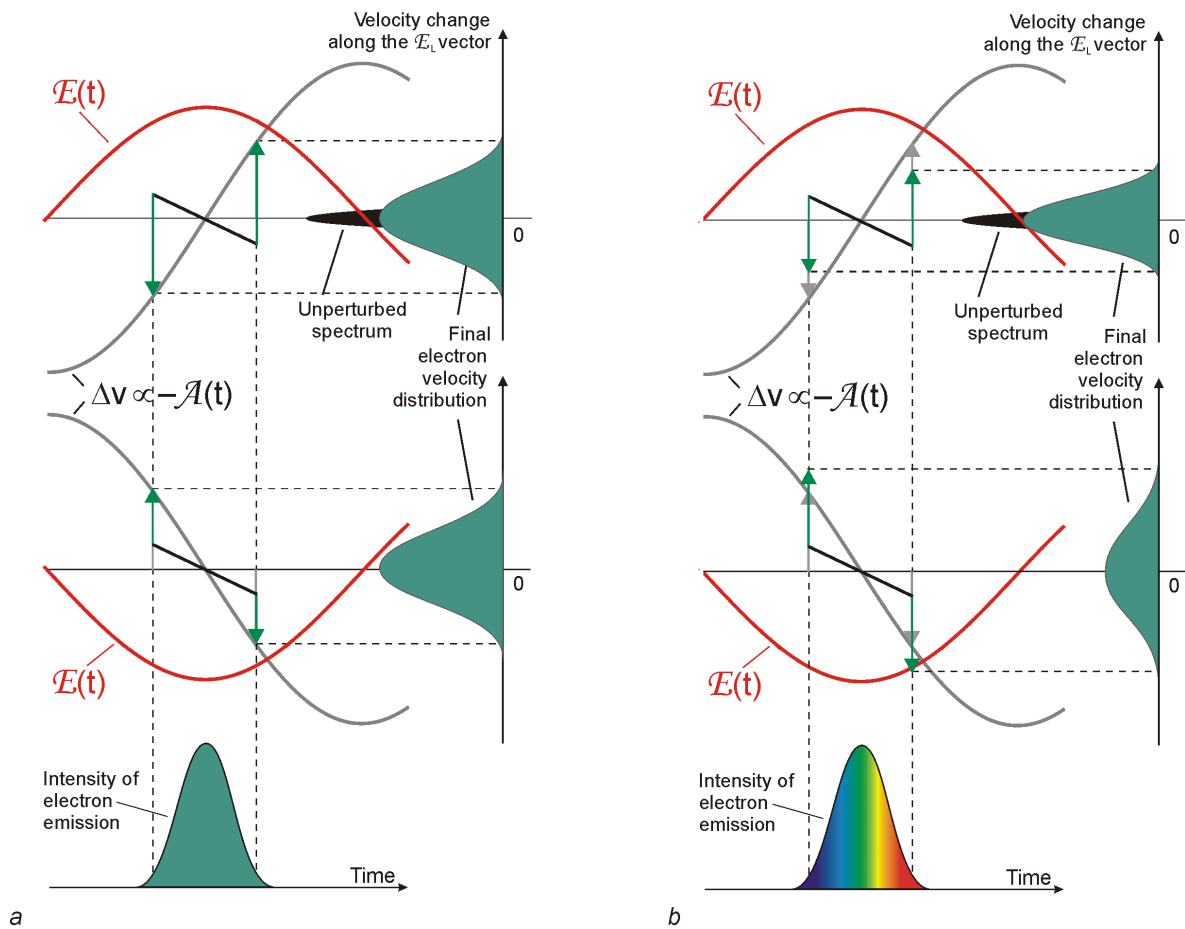


Figure 2.5.: Streaking of a bandwidth-limited (a) and of a linearly chirped (b) electron pulse at subsequent zero-crossings of the NIR vector potential. The measured streaked velocity distribution gets broadened compared to the non-streaked one depending on the sign of the electrical field and the chirp of the emitted electron wave packet (adapted from [13]).

properties are difficult to obtain theoretically. New concepts of dealing with streaking of these states have to be developed. However, core states display properties very close to atomic systems and therefore allow for characterisation of the XUV pulse. Furthermore, in the framework of the strong field approximation the time shift between two streaking traces of a solid can be used to gain insight into mechanisms and dynamics of processes involved in photoemission.

3. Dynamics of the photoelectric effect

3.1. Theoretical description of attosecond time-resolved photoemission of solids

The concept of the ATR was applied to resolve electron dynamics in condensed matter in 2007 by A. L. Cavalieri and colleagues [7]. They investigated the photoelectric effect on a tungsten (110) surface with a 300 as XUV pulse at 90 eV and a streaking NIR pulse of 5.7 fs at 702 nm. The angle of incidence was set to Brewster's angle of the NIR to minimise reflections on the surface which could disturb the streaking geometry. The electrons were collected along the surface normal, refer to figure 1.1 (a). The XUV pulse excites photoelectrons from the $4f$ states and the conduction band at a time t_0 (fig. 1.1 b). They assume that the electrons travel then to the surface without being influenced by the NIR field, which will be thoroughly discussed within this thesis. Due to their different velocities in the crystal the electrons will reach the surface at different times and feel different NIR fields there. The faster ones will reach the surface at a time t_1 , at a later time $t_2 = t_1 + \Delta t$ the slower electrons escape at a different phase of the streaking field (1.1 (c, d)). In the experiment, Cavalieri et al. demonstrated that the kinetic energy of both types of photoelectrons follow the vector potential of the NIR pulse and that the ATR is applicable to the solid state, their results are depicted in figure 3.1. Furthermore, the two traces indeed are shifted with respect to each other in time, the conduction band electrons were found to escape earlier than the $4f$ electrons by 110 ± 70 as.

To date, several theoretical explanations for the origin of this delayed photoemission have been published, and rather different models and explanations are given. This thesis presents measurements which further pursue the physical background of the time shift, therefore the main concepts of these publications are summarised here. In the original article, two concepts following the three-step-model were compared: classical ballistic transport of free electrons and transport in the band structure of tungsten. The kinetic

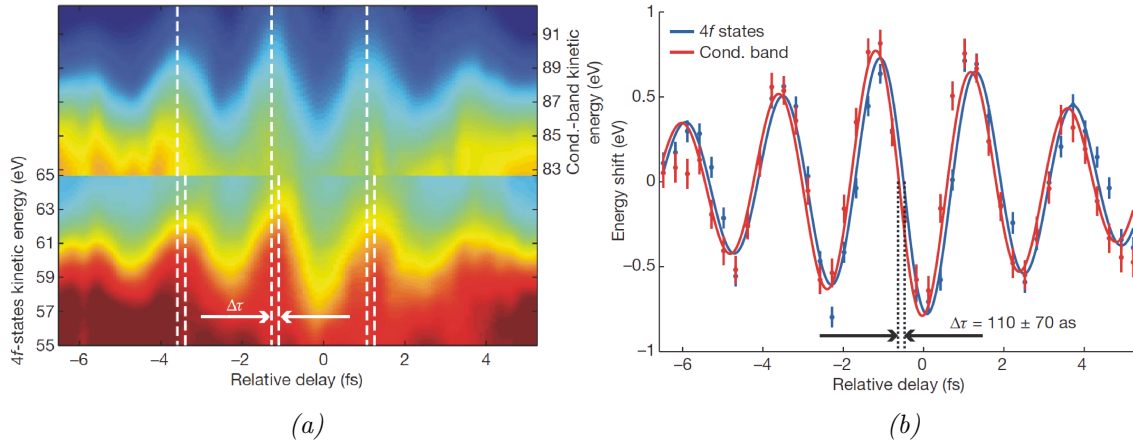


Figure 3.1.: Results of the first streaking experiment in condensed matter [7]. Both $4f$ and conduction band electrons, at central kinetic energies of 56 and 83 eV respectively, follow the NIR laser vector potential (a). The centers of energy of their traces show a delay of 110 ± 70 as between the $4f$ and the conduction band electron (b).

energy of the photoelectrons is centered at 85 eV for electrons excited from the conduction band and at 58 eV for ones from the $4f$ states. Their emission depth is limited due to the inelastic mean free path to 4 and 5 Å. Using the dispersion relation for free electrons, this leads to a time delay of 38 as, much smaller than the measured one and outside the error bars of the experiment. The authors also calculated the velocities via the gradient of the band structure. Here, one assumes that the excited electrons travel to the surface in the crystal potential. Using density functional theory to compute the high-lying bulk band structure in direction of the surface normal, the time delay due to different group velocities was found to increase to 90 as, matching the experimental result very well.

C.-H. Zhang and U. Thumm [10] calculate within the one-step-model of photoemission the transition matrix coupling the initial states of the crystal to the final Volkov states. They model the initial states as a sum over atom-like orbitals for the deeply bound and localised $4f$ states, the conduction band is represented as plane waves in the jellium model. With this model, they find that the delay is a consequence of the interference between $4f$ states originating from different layers: They varied the emission depth of both initial states and found a dependence of the timing on this only for the $4f$ states. As the conduction band is completely delocalised within their model, the escape depth

cancels out of the equations. The time delay extracted of this calculation is 110 as, if the escape depth is set to 5 Å, which is an excellent agreement with the experimental data and with calculated IMFP of tungsten [23].

Another approach was followed by A. K. Kazansky and P. M. Echenique [9]. They solve the nonstationary 1D-Schrödinger equation in the first Born approximation. They include the effect of the XUV pulse on the initial state, for the final state the NIR laser, a pseudopotential representing the crystal potential, the interaction between the final state and the remaining hole, and a damping factor for the inelastic mean free path are taken into account. The initial state was obtained by solving the equation with the crystal potential and the hole interaction for localised states, for delocalised states the hole interaction was neglected. They find different escape times depending on the spatial qualities of the initial states: for localised states the escape time depends on their initial positions in the slab. They further compared the delay between localised electrons excited to different energies. There, the delay was found to be 10 as for an energy difference of 27 eV, indicating that a band structure is not playing a role for the excited states. Finally, the delay between localised states at an average escape depth of 5 Å and delocalised states was found to be 85 as, again in good agreement with the measured data.

A rather different concept was pursued by C. Lemell and colleagues [11]. They model the electron transport classically by solving the Langevin equation of motion for a large ensemble of point-like particles. They include the force of the streaking field, a stochastic influence of scattering and a surface potential working on each electron. The optical properties of the sample are included in the momentum change due to the stochastic scattering. The momentum distribution of the initial bound states is taken from photoemission data for the $4f$ states and from density functional theory calculations for the conduction band. To model the spatial distribution of the starting positions of the electron trajectories two different cases were distinguished: The $4f$ states and the localised part of the conduction band (the $5d$ subband) were assumed to be formed of gaussian peaks around the atomic core positions. For the delocalised states of the conduction band again the jellium model was used. The main results of this calculation is the following: A significant amount of the conduction band electrons gets inelastically scattered due to plasmon losses in the crystal and escapes at a lower energy. Because the plasmon energy coincides with the energy spacing between conduction band and $4f$ states, the $4f$ photoelectron peak is consisting of direct $4f$ electrons and scattered

conduction band electrons. The scattered electrons have a larger emission depth and therefore delay the overall emission time of the $4f$ trace. Depending on the emission depth they find a time delay between 20 and 42 as, the latter one being at the lower bound of the experimental result.

One crucial point in the experiment is the behaviour of the streaking field inside the metal and its possible effects on the measurement. Cavalieri et al. did not take into account any streaking effect inside the crystal at all. Due to the high refractive index of the metal the field is bent towards the surface normal and propagates inside the sample under an angle of $\approx 14.5^\circ$. Therefore, the direction of streaking inside the crystal is almost parallel to the surface and does not severely alter the effect outside the metal. As a consequence of the different models used in the other articles, the influence of the NIR laser field inside the sample is also included by different mathematical means, but the underlying concepts are comparable. The effect of the NIR intensity decays exponentially inside the sample and works only on the final states. Both initial states are not influenced by the laser pulse at all. An explicit dependence of the delay on the NIR intensity could not be found in any of the theoretical models.

3.2. Schemes to investigate the relative time delay between two photoelectrons

All explanations given for the origin of the delay so far rely on fundamentally different physical concepts. The measurements presented in this thesis were conceived to shed light on the physical foundations of the observed delay in photoemission. Although there are no explicit predictions on the outcome of an measurement with significantly different parameters than in the initial experiment, it is possible to construct experimental schemes which test the different models.

The concept of transport of final states in a band structure given by [7] and the effects due to different initial states investigated by [9, 10] can be easily tested. The observed delay should not change with the energy of the exciting XUV pulse if only the properties of the initial states are responsible for the effect. In contrast, any dependence on the final states should manifest itself in different delays for different XUV energies. We therefore vary the energy of the attosecond pulse between 90 and 130 eV and measure the time delay of tungsten (110) at three different energies in this range. Over this interval, the

escape depth of the electrons varies only on the order of 1.5 Ångstroms [23]. The problem of obscuring the variation of the delay due to a final state effect with a variable escape depth is therefore excluded.

The effect can be entangled with the optical plasmon loss in tungsten as pointed out by C. Lemell [11]. Therefore, we do not only investigate tungsten, but also a second metal, rhenium (0001), where the plasmon loss does not overlap with a photoelectron feature [47]. Again, measurements at different XUV energies are performed to discriminate between an initial state or a final state effect. Additionally, comparing the results on tungsten and on rhenium should offer valuable clues on possible material dependent properties of the time delay.

In addition to the experimental work, theoretical calculations are done as well. The band structure of bulk tungsten and rhenium is calculated with density functional theory and is used to predict the time delay at different XUV energies within the three-step-model. A possible influence of different initial states due to different bandwidths of the XUV pulse is captured in these calculations as well as different acceptance angles of the detector. The results can be used to further test the band structure theory using different surface orientations of the investigated crystals.

Another crucial point of the work presented here was to confirm the assumptions concerning the influence of the NIR pulse on the experiment and to strengthen the experimental facts that the laser field does not influence the time delay. The intensity of the laser is still very strong in the topmost layers of the crystal. However, its direction is almost parallel to the crystal surface due to the high refractive index. Still, the exact mechanism of refraction in the first layers where the Fresnel formulas are not valid are not known exactly. For this reason, measurements at different NIR intensities were taken. Any influence of the streaking field should be visible either directly in the delay or in any other parameters obtained from the data. The results obtained on the single crystal metal surfaces are presented in chapter 6.2.

3.3. Schemes to reference the absolute time delay between two photoelectrons

Up to now, only the relative timing between two photoelectrons originating from an average escape depth could be investigated. The absolute emission time between

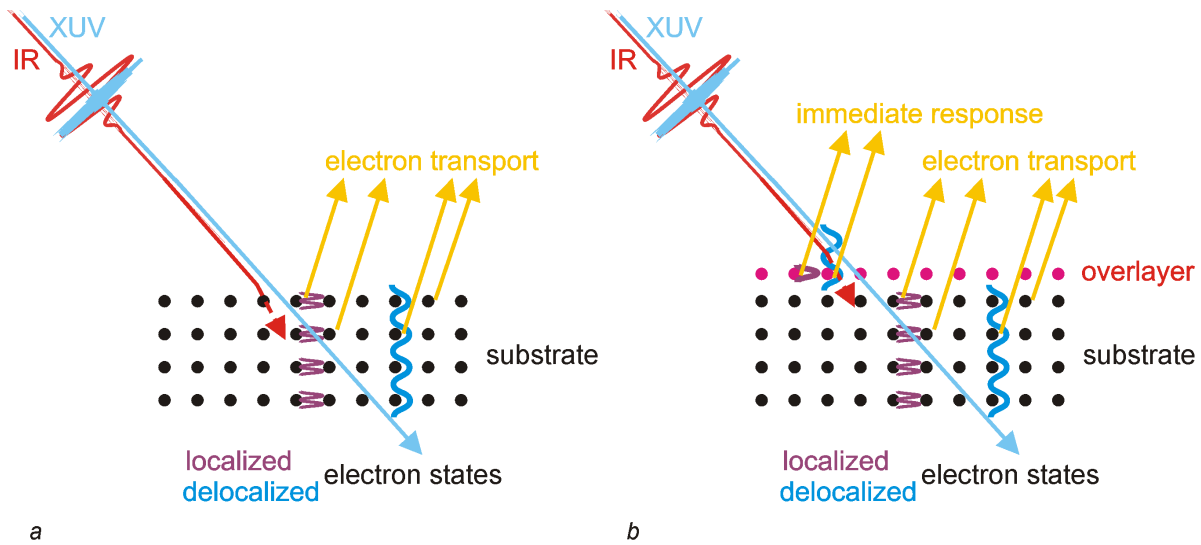


Figure 3.2.: Concept of relative (a) and absolute (b) timing of the escape time of photoelectrons in a solid state streaking experiment (courtesy of P. Feulner).

generation of photoelectrons and their escape is not accessible with the schemes employed so far. Already in the initial article, the conceptual idea of getting access to the absolute transport time of the photoelectrons was formulated. J. C. Baggesen explicitly proposed two model systems which could lead to a measurement of the absolute delay [48]. They eliminate the effect of transport for one type of electrons and to use this streaking trace as a timing reference for other traces. Baggesen suggested to use an electronic reference state which is located outside the investigated crystal. Image potential states or a single layer on top of a crystal can be used for this purpose. Image potential states [21] arise if a charge is put in front of a conducting surface. Although their properties are well understood, this system is not too easy to prepare and its behaviour can be disturbed by both the streaking laser and the low energy electrons excited by above-threshold-ionisation due to the NIR pulse (these electrons are usually referred to as ATI electrons).

The approach followed in this thesis is illustrated in figure 3.2. On top of a crystal a monolayer of a different material is grown. The photoelectrons of this topmost layer immediately feel the influence of the NIR laser after they are excited by the XUV pulse. Any time delay due to transport is removed. Electrons from the substrate experience a similar transport scenario like in the uncovered crystal. After excitation, they have to

travel through the substrate until they are streaked by the NIR field. If the photoelectron peaks of the two materials do not overlap in energy, the absolute delay of the substrate electrons can be measured this way.

The reference layer has to fulfill three main requirements: Firstly, mixing of electronic states between substrate and adsorbate layer should be minimised. Secondly, it must be possible to resolve the energy levels of substrate and reference with a broadband XUV pulse. Thirdly, reproducible growth of a single layer of the reference material on the substrate has to be feasible.

The first condition is most easily fulfilled if rare gases are used as a reference. They interact with any substrate only via the van-der-Waals force. There is no chemical bond involved, the atoms of both substrate and gas are only weakly polarised and the electronic properties remain almost unperturbed. The justification of this approach is discussed in detail in chapter 6.3. To satisfy the second and third condition, a suitable rare gas has to be selected. Xenon was used in this thesis, its properties are given in chapter 6.1. First measurements on a combined system of rhenium and xenon were done, the results are presented in chapter 6.2.

4. Experimental setup

In the first section of this chapter, the concepts of ultrashort pulse generation are reviewed and the used laser system is briefly described. The second, and main section deals with the beamline which was designed and set up specifically for the experiments carried out within this thesis and which offers the possibility to investigate electron dynamics in various solid state systems on the attosecond timescale.

4.1. The laser system

4.1.1. High harmonic generation and single attosecond pulses

In order to realise an attosecond transient recorder as described in the previous chapter, isolated, single attosecond pulses are necessary. Conventional solid state laser systems have carrier wavelengths on the order a few 100 nanometers up to some micrometers [49, 50]. The shortest pulses available with such a laser are on the order of several femtoseconds [51]. To achieve pulse lengths of 300 attoseconds, a carrier wavelength of less than 90 nanometer is required. This regime can be reached with nonlinear frequency conversion: Focussing a high-intense laser pulse on a gaseous target produces high-order harmonics of the fundamental carrier frequency up to an order of 1000 [52]. Under certain conditions, the harmonic radiation can be used to isolate single attosecond pulses.

The process of high harmonic generation (HHG) was described by P. Corkum [53] in a semiclassical three-step model (see figure 4.1 (a - c)): When a laser pulse with an intensity on the order of 10^{14} W/cm^2 hits an atom, the Coulomb potential of the core gets bent due to the strong electric field. Now, an electron wave packet can tunnel through the potential barrier and appear in the continuum (a). There it is accelerated classically and describes an oscillating trajectory following the vector potential of the laser field (b). With a small probability the electron can recombine with the parent ion, producing a photon (c). As this process is coherent, the generated high harmonics

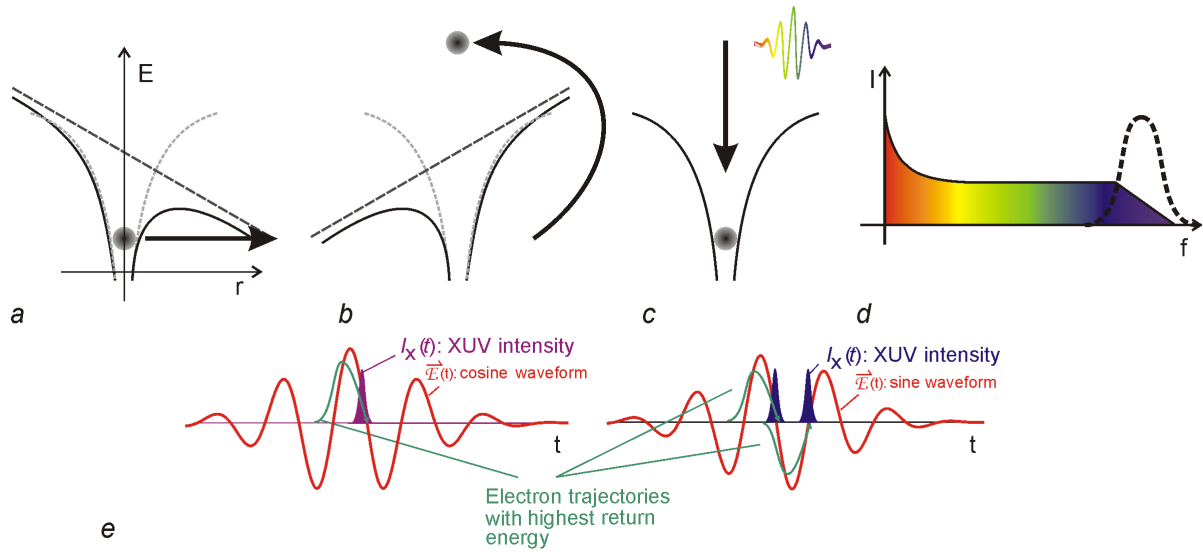


Figure 4.1.: Concept of attosecond pulse generation with an ultrashort laser pulse: semi-classical three-step model of high-harmonic generation with an electron from a noble gas atom in an external electrical field (a-c), schematic HHG spectrum, an energy filter isolates high-energy XUV bursts in the cut-off region (d), generation of single or double attosecond pulses in the cut-off region depending on the NIR carrier-envelope phase (e, adapted from [13]).

co-propagate with the fundamental laser pulse and form a beam which can be used for experiments. The spectra obtained from this process show an exponentially decaying part at low photon energies, a pronounced plateau with distinct peaks at odd harmonics of the driving laser at intermediate energies, and a quickly decaying cut-off at the high frequency end (d).

The maximum photon energy produced by recombination depends on the ionisation potential I_P of the target atom and on the averaged kinetic energy the electron has accumulated during acceleration in the electric field, $U_P(t_0)$, depending on its time of release t_0 :

$$E_{phot,max} = I_P + 3.17 U_P(t_0) \quad (4.1)$$

This formula is the result of a semiclassical calculation [53]. A quantum-mechanical treatment leads to a factor of ≈ 1.3 for the ionisation potential [54]. Further investigation

shows that electrons participating in the HHG process are created near to maxima of the NIR electrical field and that they recombine close to zero-crossings of the field, this can be seen out of a semiclassical analysis, the results agree with a quantum mechanical calculation given in [55]. These bursts of XUV radiation occur with twice the driving laser frequency but with varying signs of their Fourier amplitudes, explaining why only odd harmonics show up in the plateau.

The situation is different in the cut-off region if the NIR pulse is sufficiently short and consists of only a few cycles: Here, the phase between the carrier wave and its envelope (carrier-envelope phase, CEP) starts playing a crucial role. In a first, simplified picture, two extreme situations can be distinguished: If the phase is set in a way that the field maximum is located at the maximum of the envelope, this is usually referred to as “cosine-pulse”, then one single XUV burst with an energy higher than the ones generated by the other field peaks is produced there (4.1 (e)). In case of a “sine-pulse”, where two field maxima with similar amplitudes are present, two identical bursts with little less energy than in case of the cosine-pulse are produced. The fact that the highest energy photons can be confined temporally in only a single XUV burst opens now the possibility to single attosecond pulses: Putting an adequate energy filter centered at the cut-off region into the XUV beam spectrally and thus temporally isolates the highest energy photons, yielding an isolated pulse (4.1 (d)). This is done with a combination of an ultra-thin metal foil and a specifically designed multi-layer mirror, which has a non-zero reflectivity in the XUV range of interest. In case an NIR pulse consisting of only one or two optical cycles is used for HHG, the mechanism gets more complicated and single pulses can be generated with several settings of the CE phase [34].

It is clear that this mechanism only works reproducibly if the electrical field inside the envelope is the same for subsequent NIR pulses. The CEP has to be stabilised in the driving laser [56, 57]. This is done with two feedback loops in the laser system, the procedure is described in the next section. Once the phase is locked, each NIR pulse will not only produce the same HHG spectrum, but the final attosecond pulse will always have the same timing relation to the NIR laser pulse envelope. Also, the pulse of the NIR laser has to consist of only a few cycles to make sure that really only one XUV burst is produced with the highest harmonics, not a pulse train. Therefore, few-cycle laser pulses and XUV bursts created via HHG are invaluable tools for streaking measurements.

Looking at HHG not only on an atomic scale, but also on the scale of a macroscopic ensemble, propagation effects have to be considered: Firstly, the generated XUV-beam

can be reabsorbed by the gas. Secondly, due to the Gouy effect the phase of the focused NIR pulse gets shifted by $\pi/2$ across a distance of twice the Rayleigh range. This leads to incoherence of harmonics generated at different positions along the laser path. Thirdly, the contributions of the target gas and the free electrons to the refractive index lengthen the NIR pulse and result in different phase velocities of NIR and XUV. These three effects set certain constraints to HHG and the experimental environment: Reabsorption of the XUV beam can be minimised by confining the target gas to a small, well defined volume and lowering the pressure of the environment to $\approx 10^{-2}$ mbar or lower. The Gouy-shift and the dephasing can be compensated by choosing a proper pressure and interaction length in the gas target [58, 59]. These aspects have to be considered when designing a setup for HHG.

4.1.2. Ultrashort pulse generation

The mechanism responsible for HHG puts the basic constraints on a laser system which is used for streaking experiments: The pulses should consist of only a few cycles of the carrier field, the intensity in the focus should be on the order of 10^{14} W/cm², and the carrier-envelope phase has to be stabilised.

The laser system used for the experiments presented here consists of a carrier-envelope phase-stabilised oscillator, a chirped pulse amplification (CPA) system (modified Rainbow oscillator, refer to [60] for details; Femtopower Compact Pro, Femtolasers GmbH, Wien) and an additional broadening step with a neon-filled hollow-core fibre with a final chirped mirror compressor. The system was thoroughly described in [51], here only the main components are shortly explained.

The Kerr-lens mode locked oscillator delivers pulses of ≈ 7 fs duration with a pulse energy of 2 nJ (average power of 140 mW) at a repetition rate of 70 MHz. The spectrum ranges from 600 to 1050 nm, the carrier wavelength is at 800 nm. The mirrors in the cavity are chirped mirrors for dispersion control, an additional pair of glass wedges is put into the cavity for external tuning of the dispersion. After the cavity, the beam is focussed into a nonlinear crystal for self phase modulation (SPM) and difference frequency generation (DFG). Both dispersion control and nonlinear interaction in the crystal are necessary for the CEP stabilisation, which will be explained in the next section.

After the oscillator the pulses are stretched to ≈ 10 ps with a block of heavy flint glass (SF57) and several reflections on chirped mirrors which pre-compensate for high order

dispersion occurring during the amplification. The stretched pulses are then amplified in a nine-pass CPA system based on Ti:Sapphire. Here, the pulses are amplified to ≈ 1 mJ, corresponding to 3.8 W, in a 4 mm Brewster-angle cut Ti:Sapphire crystal which is cooled to 190 K to minimise thermal lensing. The repetition rate is reduced to 3 kHz with a Pockels cell. The CPA system is pumped with 20 W using a frequency doubled diode pumped Nd:YLF laser at 527 nm (Photonics Industries, DM 30-527).

The amplified pulses are compressed to ≈ 23 fs with a hybrid compressor [51]: The amount of glass in the beam path inside the prism compressor was set to let the pulse leave with a slight negative chirp. This residual chirp is removed with a set of chirped mirrors. That way, the shortest pulse does not appear inside the last prism, but at the mirrors. If the prisms compress the pulse completely, SPM occurs inside the last prism due to the high intensity reached there. Due to the pre-chirp of the pulses, this would narrow the spectrum [61], making it difficult to achieve pulse lengths of only a few cycles.

The Ti:Sapphire crystal in the amplifier cannot support the complete spectrum of the seed pulses because of gain narrowing during the amplification process. After the CPA stage the pulses typically have a bandwidth of ≈ 70 nm, compared to > 400 nm which are delivered by the oscillator. To obtain pulses shorter than 5 fs, an additional broadening has to be set up: Focussing the beam through a hollow-core fibre filled with a rare gas introduces SPM. A fibre, filled with 1.8 bar Neon, with an inner diameter of $200 \mu\text{m}$ and a length of 1 m leads to a spectrum reaching from 400 to 1000 nm. The throughput is slightly above 50%, the pulse energy after the fibre is $500 \mu\text{J}$. Right after the fibre a pair of wedges is used to control the pulse length for high harmonic generation.

The pulses are recollimated after the fibre and then compressed to sub-4 fs with a final set of chirped mirrors. Right after the final chirped mirror compressor, the laser enters a vacuum tube through a thin glass window, whose group delay dispersion was pre-compensated in the last compressor stage. The vacuum at this stage is kept at $\approx 10^{-4}$ mbar, ensuring that no pulse lengthening due to the dispersion of air can take place anymore.

4.1.3. Carrier-envelope phase stabilisation

Phase stabilisation of the oscillator

As was already mentioned, a fixed relation between the electrical field and its envelope is imperative for reproducible single attosecond pulse generation. The spectrum of a pulse

train from a mode-locked oscillator resembles a frequency comb with single, narrow lines at

$$f_n = n \cdot f_{rep} + f_{CEO}, n \in \mathbf{IN} \quad (4.2)$$

The comb lines are separated by the repetition rate, f_{rep} , the whole comb is shifted from zero by f_{CEO} , the carrier-envelope offset (4.2 a). Converting this to the time domain, it is easy to see that the phase inside the envelope is shifted from one pulse to the next one by

$$\Delta\phi_{CEP} = 2\pi \frac{f_{CEO}}{f_{rep}}, \quad (4.3)$$

as displayed in figure 4.2 (a). f_{CEO} arises from different group and phase velocities inside the oscillator cavity. Even if the whole cavity was put into vacuum the gain medium would still cause a non-zero phase shift. Furthermore, both repetition frequency and carrier-envelope offset fluctuate randomly due to perturbations to the laser like vibrations or temperature shifts. These perturbations affect both the length of the cavity and its refractive index, and are therefore directly translated to the frequency comb. To keep a fixed comb, the stabilisation of f_{CEO} is of primary interest. The fluctuations of f_{rep} are on a far longer time scale than the ones of f_{CEO} [62] and can be minimised for the purpose here by using rigid, small optical mounts and covering the oscillator.

The first problem in a phase stabilisation scheme is the access to the value of the carrier-envelope phase of the laser pulse. Normal measurements are sensitive to the intensity and cannot give any information of the phase value. Mixing light fields in a nonlinear crystal however gives rise to interference terms and thus to a phase sensitive signal. Two nonlinear effects are used for phase stabilisation: difference frequency generation or second harmonic generation (SHG) and self phase modulation. A second frequency comb is generated in a periodically poled lithium niobate crystal, doped with magnesium oxide (PPLN), either by DFG or by SHG [63]. The new comb lines follow the relationship of

$$\begin{aligned} f_{SHG} &= 2k \cdot f_{rep} + 2f_{CEO} \\ f_{DFG} &= (k - l) \cdot f_{rep} \quad k, l \in \mathbf{IN}. \end{aligned} \quad (4.4)$$

At the same time, the fundamental comb gets broadened in the crystal due to SPM. As a consequence, both combs overlap and mix with each other (figure 4.2 (b)). The

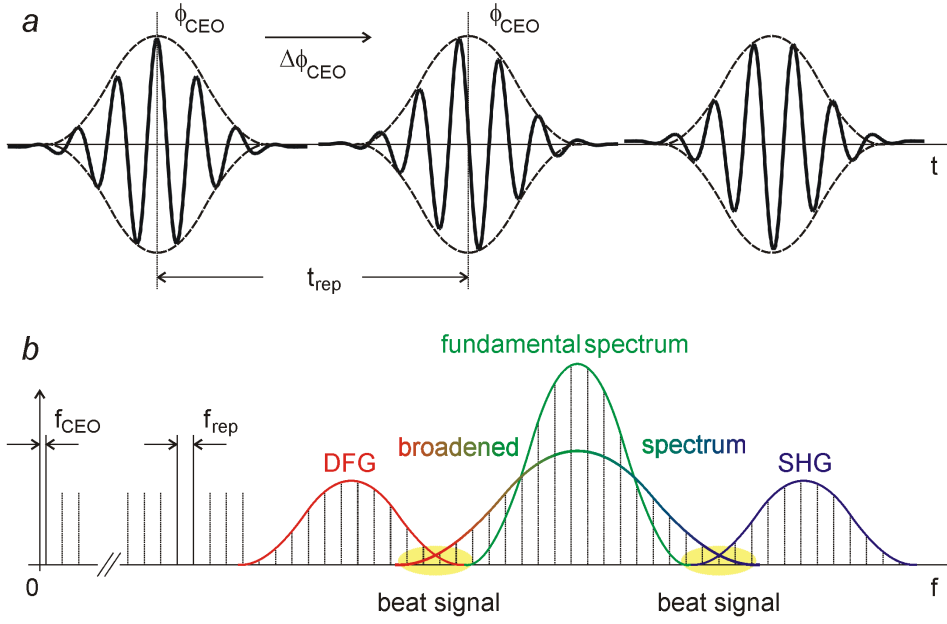


Figure 4.2.: CEP slip between subsequent pulses (a): a non-zero shift of the frequency comb lines f_{CEO} causes a shift of the CE phase. Spectra necessary to generate a beat signal (b): components of a (broadened) fundamental spectrum overlap with components of an DFG or SHG spectrum.

signal arising in the overlapping area now explicitly contains f_{CEO} ,

$$\begin{aligned} (2k \cdot f_{\text{rep}} + 2f_{\text{CEO}}) \otimes (n \cdot f_{\text{rep}} + f_{\text{CEO}}) &= (2k - n) \cdot f_{\text{rep}} \pm f_{\text{CEO}} \\ ((k - l) \cdot f_{\text{rep}}) \otimes (n \cdot f_{\text{rep}} + f_{\text{CEO}}) &= (k - l - n) \cdot f_{\text{rep}} \pm f_{\text{CEO}}, \end{aligned} \quad (4.5)$$

and can be detected after spectral filtering with a photodiode. In principle, the comb generated by DFG is per se phase-stabilised. However, as its intensity is very weak and its spectrum is shifted far in the infrared, it cannot be used further to directly seed the laser system. Which comb is produced depends on the orientation and period of the crystal and its resulting phase matching conditions. In the oscillator system described here, the DFG is used. This scheme is called f-to-0f interferometer.

Once the phase value can be detected, it has to be stabilised (using software and electronics from MenloSystems): The measured phase signal is compared with a fixed frequency, f_{ref} , of a quarter of the repetition rate of the oscillator. Depending on the deviation from the reference, a proportional-integral (PI) controller gives a feedback to

an acousto-optic modulator (AOM) placed into the pump beam inside the oscillator. The AOM introduces a small amplitude modulation to the pump beam by diffracting a small amount of the power out of the beam path. The change in pump energy slightly shifts the group velocity and, mainly, changes the phase shift directly because of a different Kerr effect in the gain material [64].

This closed loop in the oscillator, the so-called “fast loop”, produces a pulse train with the same CEP for every fourth pulse. The Pockels cell in the multi-pass amplifier, which works as a pulse picker, is locked to the external reference frequency as well, making sure that every pulse leaving the CPA system has the same phase value.

Phase stabilisation of the amplifier

Although the oscillator delivers a CEP locked signal, the phase at the fibre output is drifting on a long time scale of several seconds because of intensity fluctuations in the amplifier and pointing instabilities in the compressor. A second phase-locking loop is therefore necessary. After the broadening step in the hollow-core fibre, a reflection of one of the wedges is used to send a fraction of the pulse to a f-to-2f interferometer. Here, SHG in a beta-bariumborate (BBO) crystal is used to generate a second frequency comb. The initial comb after the fibre is already broader than one octave, so no SPM mechanism is necessary here, and the light fields can mix directly in the crystal. The signal in the overlapping part of the two combs is detected with a spectrometer. The software controls the position of one prism pair in the compressor of the CPA system, introducing a different dispersion depending on the amount of glass inserted.

Those two loops can stabilise the absolute phase to less than 0.2 rms for several hours, if environmental perturbations like acoustical noise or vibrations are minimal.

4.2. Ultrahigh-vacuum attosecond beamline

The ATR has produced results with unprecedented time resolution of various effects mainly in the gas phase [42, 44, 36, 65]. In a first proof of concept experiment in 2007, A.L. Cavalieri and colleagues [7] showed that the technology of attosecond streaking is also applicable to the solid state. The apparatus used for this measurement fulfilled only the very basic requirements for surface science experiments. It was one main goal of this thesis to develop a new, flexible attosecond setup providing an

ultrahigh vacuum environment and sophisticated solid state sample preparation and characterisation schemes, which are necessary for streaking measurements of condensed matter, and which is at the same time capable of doing gas phase experiments as well.

The main challenge lies in the combination of HHG in the gas phase and surface sensitive photoelectron spectroscopy on single crystals. To obtain a clean surface for more than one hour, the base pressure in the surrounding experimental area has to be on the order of 10^{-10} mbar. Typical pressures inside the HHG target exceed 10^2 mbar. A pressure gradient of more than 12 orders of magnitude has therefore to be maintained during the experiments. Additionally, it has to be possible to generate attosecond pulses at different photon energies to investigate the dependence of the observed effects on the exciting XUV energy. This implies varying focal lengths and intensities of the NIR on the HHG target as well as the possibility to observe the spectrum of the XUV radiation over a broad spectral range. Moreover, the XUV multilayer mirror, which isolates a single attosecond pulse, has to be exchanged easily, as for each XUV photon energy an individually designed mirror has to be used.

Several other requirements which are not specific for surface experiments, but for attosecond experiments in general, have to be fulfilled: The vibrational level of the setup has to be kept as low as possible. Vibrations might not only introduce a jitter in pointing, but may significantly decrease the time resolution of the ATR. To maximise the XUV flux on the target, reabsorption in the residual target gas of HHG has to be minimised. This puts an upper limit on the ambient pressure of the HHG chamber.

In order to be able to acquire high quality streaking data of a large variety of samples as a function of several external parameters, the following advanced design goals were defined for the new beamline:

- ultrahigh vacuum conditions at the sample
- variable XUV energies
- monitoring of the XUV spectrum
- quick exchange of XUV mirror, solid sample and consumables
- extended sample preparation and characterisation
- angular resolution of the detected signal

- variable detection schemes
- possibility to perform gas phase experiments

The work resulted in a new beamline, referred to as AS3, the only completely equipped ultrahigh vacuum single attosecond beamline for solid state experiments currently in operation [66]. An overview of the setup is given in figure 4.3. High harmonics are generated in a gas target, the residual NIR pulse and the XUV radiation co-propagate through a differential pumping system, pass a spectrometer for XUV characterisation and go through a filter which spatially separates the NIR and the XUV. Inside the experimental chamber, a double mirror isolates a single attosecond pulse out of the XUV radiation, introduces a delay between XUV and NIR pulses, and focusses both beams on the target. The excited photoelectrons are observed with a detector which can be rotated around the sample for angular resolution. The samples are cleaned, prepared, and characterised in a second chamber. Each part is thoroughly described within the next sections. The pumping scheme of each component is covered in one single section, handling the vacuum layout of the complete beamline.

4.2.1. High harmonic generation

The laser beam enters the AS3-beamline through an iris and is focussed on the HHG target with a spherical mirror in a z-folded geometry. The target is a nickel tube, sealed on top, supplied with the target gas from the bottom, in which the laser drills its own hole. The generated XUV beam and the residual NIR co-propagate then in direction of the experimental chamber.

The z-geometry serves two purposes: Firstly, the small angle on the focussing mirror minimises astigmatism. Secondly, this geometry makes it easy to vary the distance between target and focussing mirror and keeping alignment simple at the same time. The variation of the focal length is necessary to achieve a wide range of reachable cut-off energies: According to equation (4.1), the cut-off depends on the ionisation potential of the target gas and the NIR laser intensity. The ionisation potential can be changed by using different rare gases. To tune the laser intensity, three different options are available: The beam can be attenuated using either a transmission filter or an iris, or the focal spot size can be varied by using different focussing optics. Attenuation with a filter is impossible for few-cycle pulses, the necessary material would significantly increase the

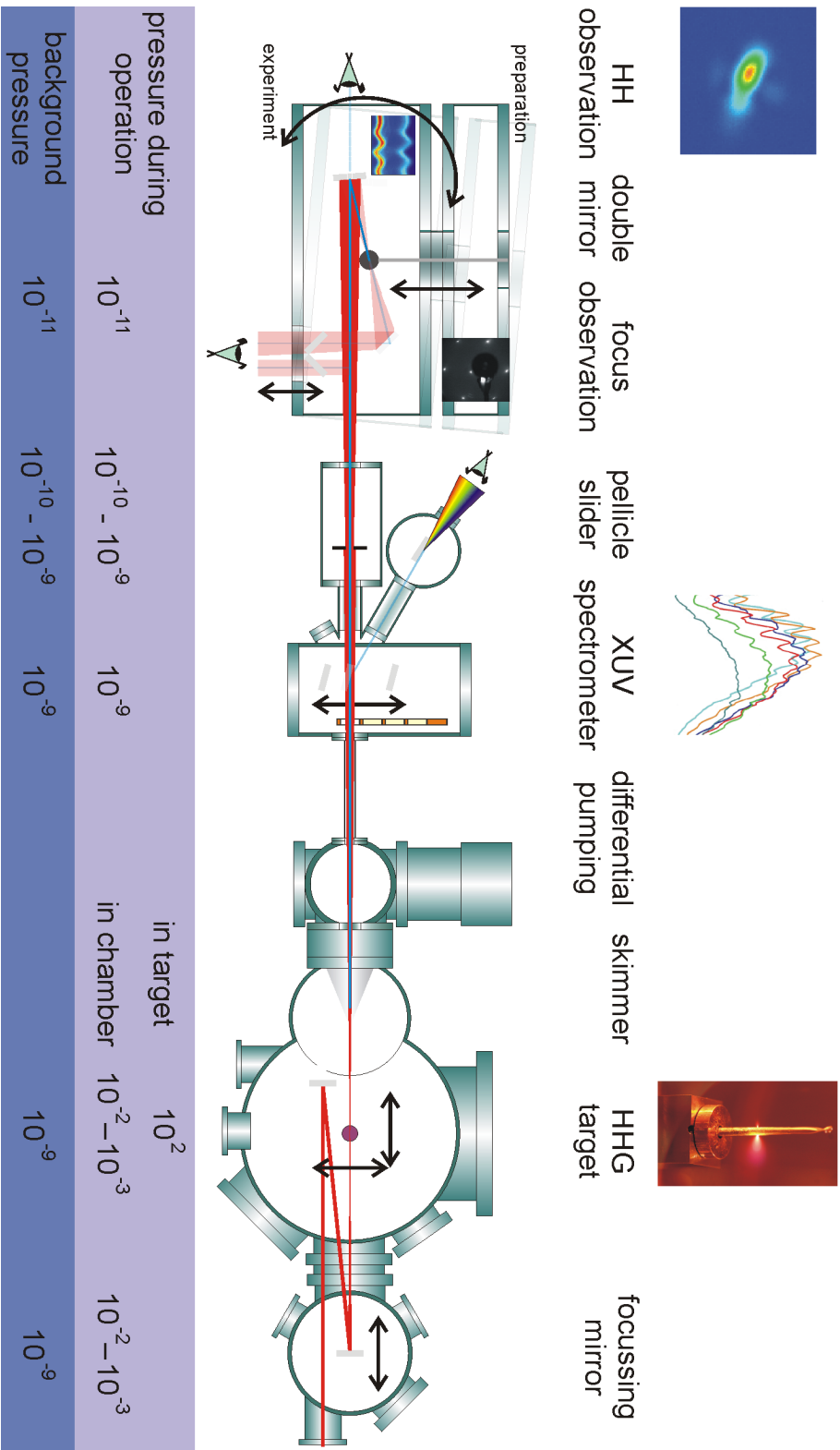


Figure 4.3.: Schematic drawing of the ASS3 beamline at MPQ.

pulse length and prohibit single attosecond pulse generation. An iris can be used only in a limited range for fine-tuning. Making the aperture too small results in a bad mode quality of the NIR beam and in inefficient HHG. Introducing mirrors with different focal lengths omits these problems.

The focussing mirror is placed in its own small vacuum chamber, whose position along the beam path can be set according to the chosen focal length. This way, a single large chamber is avoided, which would have increased the pump-down times of this regularly vented part. The focal length can be varied between 30 and 80 cm in arbitrary small steps (only limited by the used mirrors).

The gas target is made of a nickel tube, which is mounted on two translation stages for alignment (Micos VT-80 50, MTS 65). Using a small metallic tube to contain the target gas has two advantages. The gas is enclosed in a very small volume, making it possible to reach the necessary pressure for efficient HHG with a low gas flux. Additionally, the thin nickel tube is soft enough to be easily deformed by hand. The tube can be squeezed to the optimum thickness where the phasematching conditions are optimal and the highest XUV flux is achieved.

The results presented in this work were obtained with a focal length of 55 or 60 cm, resulting in a spot diameter at $1/e^2$ of $\approx 90 \mu\text{m}$ and a maximum intensity of $5.7 \cdot 10^{14} \text{ W/cm}^2$. High harmonics were generated in neon with a pressure between 200 and 300 mbar in the target. For the experiments presented in this thesis, the cut-off was tuned between 90 and 130 eV, higher energies are still possible.

4.2.2. XUV diagnostics

As explained previously, the position and shape of the HHG cut-off, which defines the properties of the attosecond pulse, depends on the intensity and the CEP of the NIR laser. Theoretically, both quantities could be set once for one desired XUV wavelength and the setup has to be changed only for different XUV energies. However, small variations in the NIR laser performance due to thermal drifts or minimal changes in the beam path happening on a daily basis make a repeated adjustment of the HHG setup necessary. Therefore, a fixed installed XUV spectrometer is needed to check the properties of the generated high harmonic radiation. A home-made spectrometer was built which is capable to monitor XUV radiation in the desired energy region between 80 and 140 eV.

Two grazing incidence gold-palladium mirrors are mounted on a translation stage perpendicular to the beam path (Micos, VT-80 75). One mirror reflects the beam directly on a detector, the other one directs the beam on a grating, which disperses the high energy region on the detector. The orientation of the gold mirrors is aligned once, under vacuum only their position perpendicular to the beam can be changed. Small variations of the beam path can be corrected with the orientation of the grating and the position of the detector. The tip angle, meaning horizontal alignment, of the grating can be adjusted via a rotational feedthrough. The detector is mounted on a sliding mechanism and connected to the grating chamber with a highly flexible bellow. It can be moved along and perpendicular to the beam path to make sure the XUV spectrum is found.

The used grating is a gold-coated flat-field grating from Hitachi (No. 001 – 0437, [67, 68]). It nominally supports a bandwidth of 15 nm, from 5 to 20 nm, corresponding to 250 to 62 eV. Although the efficiency of the grating drops significantly outside that interval a weak signal might still be observed there. The grating is concave with a variable groove spacing which disperses the spectrum on a flat plane perpendicular to the propagation axis instead of a cylindrical surface. Therefore, the observed spectra do not have to be corrected for any distortions or imaging errors.

The detector is a double chevron plate, coated with caesium iodide for an enhanced sensitivity in the XUV range, with a phosphor screen on the back (Beam Imaging Solutions, BOS-40). The image on the screen is monitored with a digital camera (Point Grey, Flea2) and can be recorded with a computer. Instead of the MCP/Phosphor-system a back-illuminated CCD (Roper Scientific, Pi-SX) can also be attached to the spectrometer.

In front of the spectrometer, a 450 nm thick zirconium filter can be brought into the beam path to completely block the NIR radiation. A second filterslider contains four insets for filters to suppress different regions of the XUV spectrum. Silicon and aluminium are used to calibrate the spectra: Their steep edges in their XUV-transmission allow to identify the wavelength regions around 60 and 100 eV. Palladium or zirconium are used to optimise the shape of the XUV spectrum in the cut-off region. The thickness of these filters usually is 200 nm, their transmission functions are depicted in the appendix. One inset is usually occupied by an $\approx 500 \mu\text{m}$ slit. This enhances the resolution of the spectrometer.

Because of the grazing incidence on the mirrors the direct spot is not optimal for maximising the XUV intensity. Therefore, a second MCP/Phosphor system, similar to

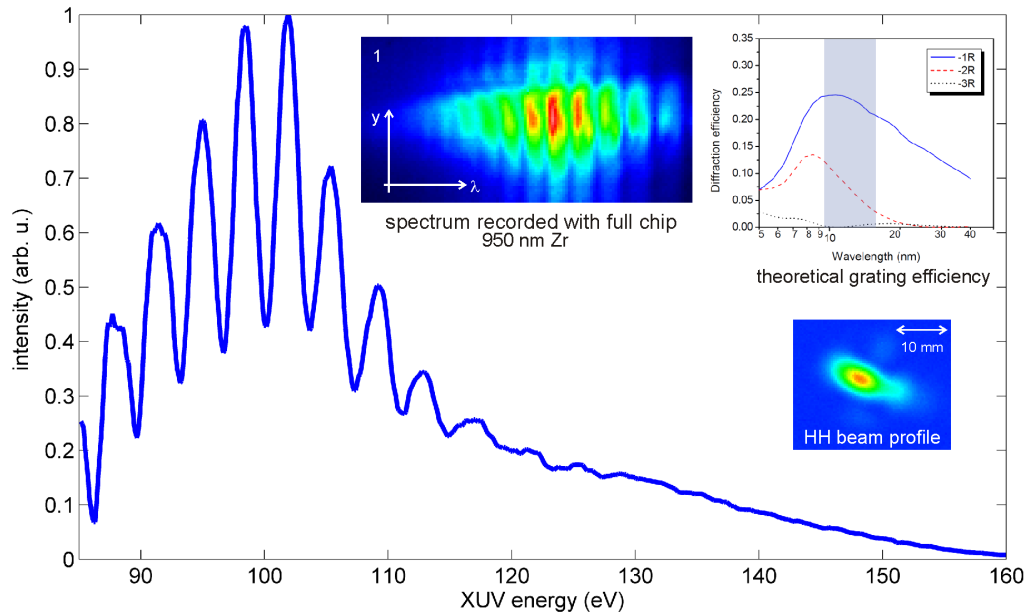


Figure 4.4.: Spectrum of high-order harmonics generated with a phase-stabilised NIR laser in Ne. The insets show the theoretical efficiency curve of the used flat-field grating (blue curve, the spectral region of interest between 80 eV and 130 eV is highlighted), a full-chip recording of the dispersed radiation obtained with 950 nm of Zr, and the direct spot of the XUV beam. The graph of the spectrum is obtained by integrating along the y -axis of the full-chip recording and correcting for the transmittivity of the metal foil.

the one in the spectrometer, is mounted at the backside of the experimental chamber. This one is then used to optimise the XUV flux. This second detector is in normal operation partly obscured by the double mirror. Both experimental and preparation chamber can be rotated using airpads to send the beam to this detector.

An XUV spectrum recorded with 55 cm focal length of the NIR pulse in neon is displayed in figure 4.4. A CCD detector was used for this measurement, the integration time was set to 0.5 s, 950 nm of zircon were used to block the NIR pulse, the NIR laser was phase-stabilised. The spectrum was obtained by integrating along the spatial y -axis of the CCD chip, a similar acquisition with a silicon filter was used to calibrate the wavelength axis. The amplitude of the individual harmonics is a combined effect of

the filter transmission and the intensity of the spectral components. The zirconium filter has a linear rising edge from 70 – 95 eV, explaining the linear increase of the harmonic amplitude at the low energy side. At high energies, the filter transmission is approximately constant, whereas the harmonic amplitude drops due to the HHG process itself. A calculated efficiency curve for the first order (blue curve in 4.4, obtained from Hitachi) shows that the reflectivity varies only by $\approx 14\%$ over the spectral region of 80 – 130 eV and does not severely influence the shape of the spectra.

4.2.3. Single attosecond pulse selection

A clean streaking experiment requires an isolated attosecond pulse to be filtered out of the high harmonic radiation. The XUV and the NIR pulses have to be isolated spatially, and the relative timing between the isolated XUV pulse and the NIR pulse has to be adjusted reproducibly. These requirements are fulfilled with two components: the pellicle filter and the double mirror stack.

The co-propagating high harmonic and NIR beams pass a nitrocellulose pellicle, 2, 5 or 15 μm thick, whose inner part is replaced with a metal foil (figure 4.5 (a)). The metal filter, 200 nm of zirconium or palladium, blocks the central part of the NIR completely, while the outer pellicle is transparent for the NIR pulse. Because the divergence of the XUV beam is much smaller than the one of the NIR the high energy part of the high harmonic radiation is completely confined to the diameter of the metal foil. This part is only weakly attenuated by the filter. The stronger diverging low-energy part of the harmonic radiation is blocked by the pellicle.

The pellicle is mounted in a filter slider, which can carry two filters (figure 4.5 (b)). Its position along the beam direction is fixed, it can be moved in the plane perpendicular to the beam path to overlap its position with the XUV spot. The vertical position is controlled with a manipulator, the horizontal one by moving the whole chamber via a sliding mechanism. Directly in front of the pellicle a motorised iris tunes the intensity of the NIR incident on the sample. The iris is mounted on a three-axis manipulator and can be aligned independently of the pellicle.

After the pellicle, the annular NIR pulse and the small XUV beam hit the double mirror. This is a spherical two-component mirror, where the central part is bored out and coated with a special multi-layer coating [69]. The layer structure is designed individually for each central XUV energy and width and sets the properties of the reflected isolated

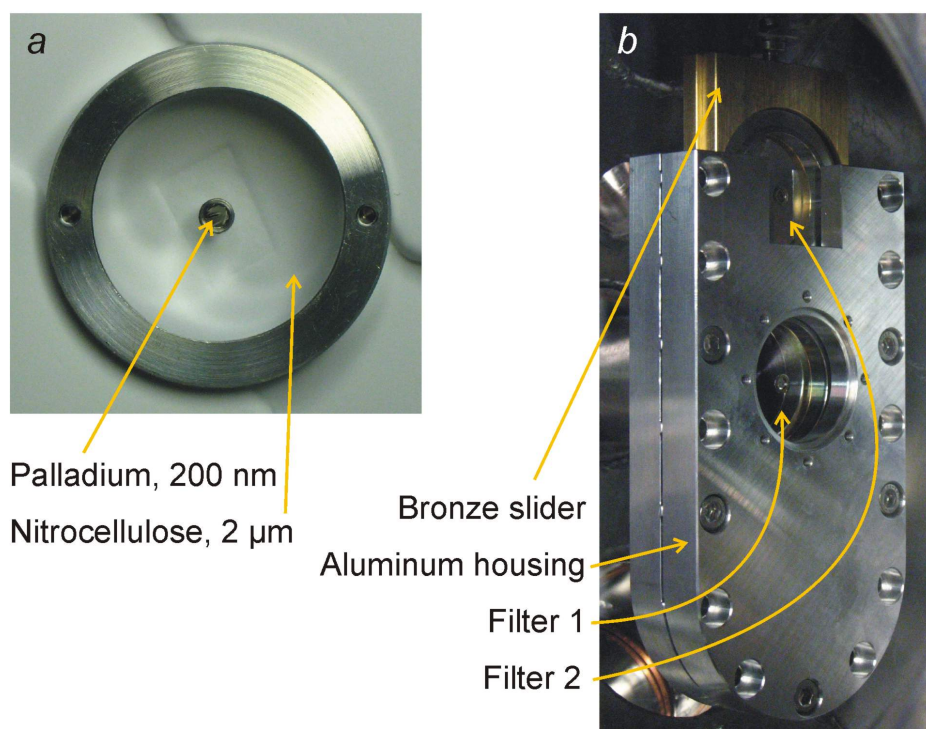


Figure 4.5.: Spatial separation of the XUV and NIR pulses is done with a combination of a pellicle and a metal foil (a), UHV pellicle slider (b).

attosecond pulse. Together with the metal inset in the pellicle it filters out the cut-off region of the spectrum with a flat phase, ensuring that no chirp is introduced which would broaden the XUV pulse in time. A measured reflectivity curve of a 130 eV mirror with 4 eV bandwidth together with 200 nm of palladium is shown in figure 4.6 (a). One clear gaussian peak appears at the desired central energy with a maximum reflectivity of 8%, the outer part is coated with 13 nm of boron carbide and reflects the NIR pulse. A high NIR intensity obtained with a regular silver coating would immediately burn and destroy the solid state sample. Therefore, a coating with a much lower reflectivity of $\approx 20\%$ at 700 nm was used here. All XUV-mirrors were designed and manufactured by M. Hofstetter.

A photo of the complete double mirror stack can be seen in figure 4.6 (b), the stack, its mounting and the loadlock were designed by E. Bothschafter and R. Ernstorfer. The outer mirror is mounted in a 1 inch tip-tilt mirror mount which can be moved with two

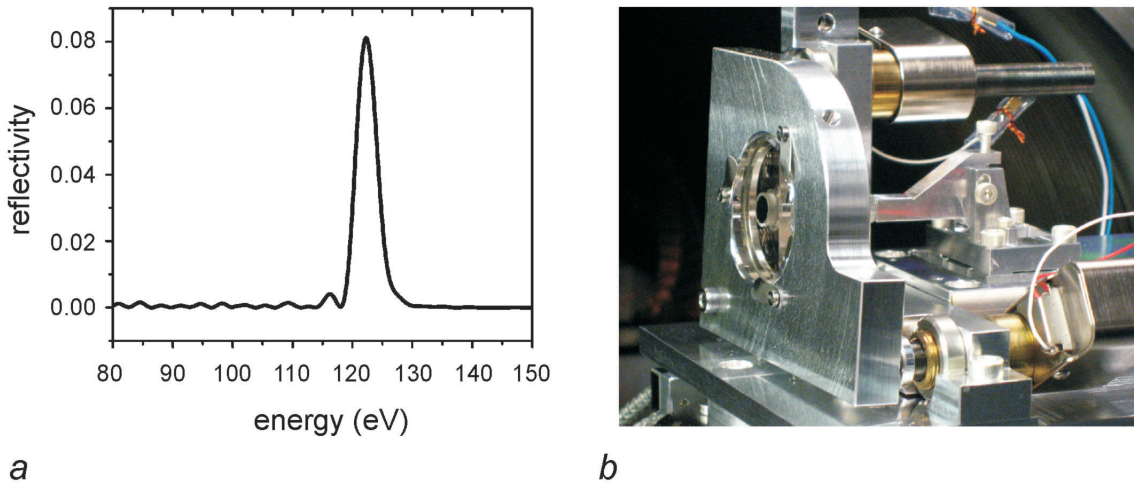


Figure 4.6.: Reflectivity curve of an XUV mirror (a, courtesy of M. Hofstetter) and double mirror setup (b). The outer mirror reflects the streaking NIR pulse, the inner one isolates a single attosecond pulse from the HHG radiation and introduces a temporal delay between the two pulses.

motorised screws (Pico motor, New Focus). Those motors are used to spatially overlap the reflection of the outer mirror with the one of the inner mirror. The inner mirror is glued to a small rod which is attached to a piezo translation stage (PI Hera 621 modified for UHV). This stage moves the inner mirror with respect to the outer one along the beam path and thus introduces a temporal delay between the XUV and the NIR. The stage has a range of $100\ \mu\text{m}$ and a nominal resolution of $0.2\ \text{nm}$, corresponding to a minimal temporal delay step of $60\ \text{as}$. The double mirror assembly is mounted on a stack of piezo stages (Nanomotion, the resolution of the encoders is $100\ \text{nm}$, with current software settings a resolution of $1\ \mu\text{m}$ is achieved) which allows for aligning the reflected beams on the solid sample. The complete mirror stack is attached on a home-built linear feedthrough and can be retracted out of the main experimental chamber in a load-lock which is separated from the main chamber with a CF-250 valve to exchange the mirror without breaking vacuum in the main chamber. This scheme will be discussed in the section dealing with the vacuum design of the beamline.

Due to the load-lock, the arm of the linear feedthrough, supporting the double mirror stack, has a length of $\approx 64\ \text{cm}$. Considering that the inner and outer mirror must not move by more than $3\ \text{nm}$ relative to each other (corresponding to a timing jitter of

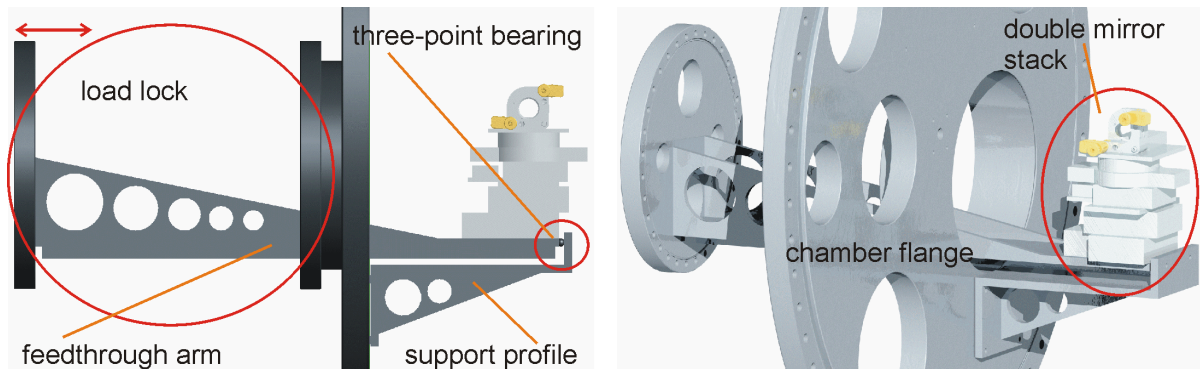


Figure 4.7.: Retraction mechanism of the double mirror. The long feedthrough necessary to position the double mirror at the correct position is shortened with a stainless steel profile mounted inside the chamber. For sake of clarity, the bellow of the feedthrough and the valve separating the loadlock from the main chamber are not shown

10 as), this long arm could be detrimental to the time resolution of the experiment. To avoid oscillations of the mirror setup, the feedthrough arm is designed as rigid, stainless steel angle, which is reinforced on the sides with plates. Inside the chamber, an extra supporting arm serves as joist for the feedthrough, shortening the arm to an effective length of only 23 cm. The mirror stack is not mounted directly on the feedthrough arm but on an extra stainless steel piece which is connected to the feedthrough arm with a system of rigid compression springs. This and a three-point bearing at the meeting plane of the extra piece and the support arm ensures that the stack is moved to exactly the same position every time it was retracted. Figure 4.7 shows the design of the mechanism.

In order to align the spatial overlap of the two mirrors on a daily basis the reflected beam is sent out of the UHV chamber and focussed on a camera (Point Grey, Fly2). Due to the double mirror structure the two spots form an interference pattern, the spots are overlapped by making this pattern symmetric. To test the symmetry, the temporal overlap is changed by adjusting the delay between the two pulses. Both temporal and spatial overlap are already pre-aligned outside the chamber so that only fine tuning is necessary for the experiment.

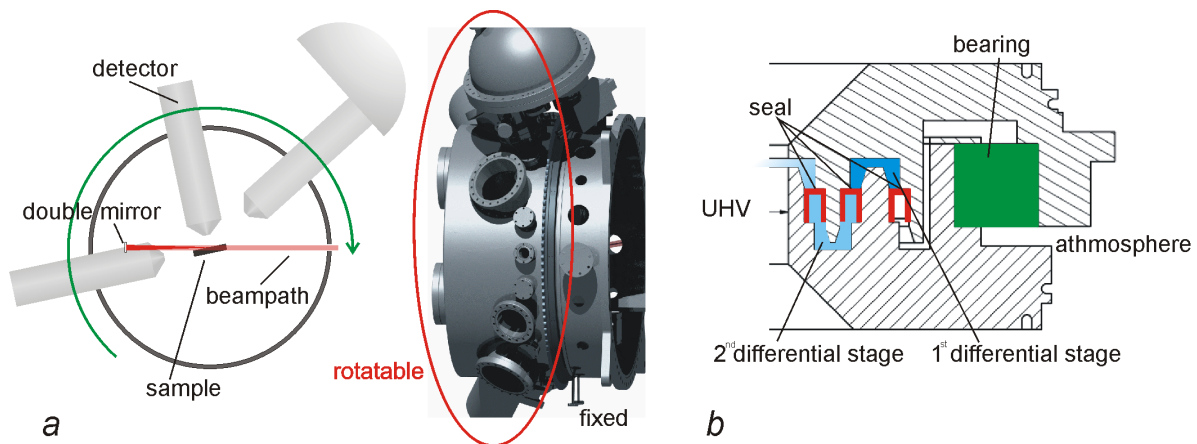


Figure 4.8.: Concept of rotating flanges (a) and of their dynamic sealing (b). The design allows for angular resolution and for detector exchange without venting, UHV conditions can be maintained even during rotation due to the differential pumping of the dynamic sealing.

4.2.4. Electron detection schemes

The design of the electron detection was done for angular resolution and fast exchange between individual detectors (figure 4.8 (a)). The experimental chamber has a rotatable part, where all electron detectors are mounted. The connection to the fixed part with the double mirror is made with a large dynamical sealing which works as rotational feedthrough, which was designed by P. Feulner. The axis of rotation is along the axis of the sample manipulator, which allows for angle-resolved measurements. The orientation and the distance of each detector relative to the sample can be fine-tuned with a manipulation system. As a consequence of the beam path and the required space of the feedthrough the detectors and the manipulator axis form an angle less than 90 degrees. The angle depends on the size of the mounting flange and ranges between 10° for a CF 40 flange and 24° for a CF 200 flange. The detectors used in this thesis were mounted on CF 160 flanges, corresponding to an angle of 20° . This is compensated by mounting the sample under the same angle.

Currently, there are two electron detectors installed, a custom time-of-flight (TOF) spectrometer (product by S. Kaesdorf) and a hemispherical analyser (SPECS, Phoibos 150). The measurements presented in this thesis were obtained with the TOF detector,

therefore only the physical concept underlying this detector is described in this section.

An electron-TOF detector measures the flighttime t of electrons starting from a trigger signal until the electrons are detected on a MCP. The TOF detector used here is energy resolving, it integrates over the spatial dimensions of the electron source, the acceptance angle varies between $\pm 2^\circ$ and $\pm 22^\circ$ depending on the settings of the electrostatic lens. If the distance d between sample and MCP is known, the kinetic energy (in eV) of the electrons ideally is related to their velocity v via

$$E_{kin} = \frac{m}{2e} v^2 = \frac{m}{2e} \frac{d^2}{t^2}. \quad (4.6)$$

Deviations from this relation may arise if an electrostatic lens inside the detector is used which serves as bandpass filter. This results in a slight distortion of the above relation, which depends both on the lens settings and the energy of the detected electrons. The exact calibration of the TOF detector is given in the appendix.

The signal obtained from the MCPs is electronically processed in several ways: The multiscaler card used in this setup has a resolution of 100 ps (FAST ComTec P7888), yielding an excellent relative energy resolution of less than 0.3 % in the range of interest. Before the signal is sent to the multiscaler it is amplified by a preamplifier (40 dB, 5 GHz) and processed with a constant fraction discriminator.

4.2.5. Vacuum layout

The pumping scheme of the AS3 beamline is displayed in figure 4.9, together with the values of the pressure during operation and in 'standby' mode. For sake of clarity, the pressure gauges in the main chambers are not indicated in this drawing. The gas load of the HHG process naturally divides the beamline in a high vacuum part (HV, $10^{-3} - 10^{-9}$ mbar) near the gas target and a ultrahigh vacuum part (UHV, $< 10^{-9}$ mbar) at the sample. The operating pressure in the UHV part is with 10^{-11} mbar two orders of magnitude lower than in the first experiment in 2007 [7]. In comparison to the previous setup, the pressure in the HHG chamber could be also decreased by almost a factor of two and usually is at $5 \cdot 10^{-3}$ mbar. The pressure gradient between the high and ultrahigh vacuum parts is maintained only via differential pumping. A separating window cannot be introduced as it would be detrimental to the pulse length of both the NIR and XUV beam.

Despite the fairly high pressure in some parts of the beamline during operation, which

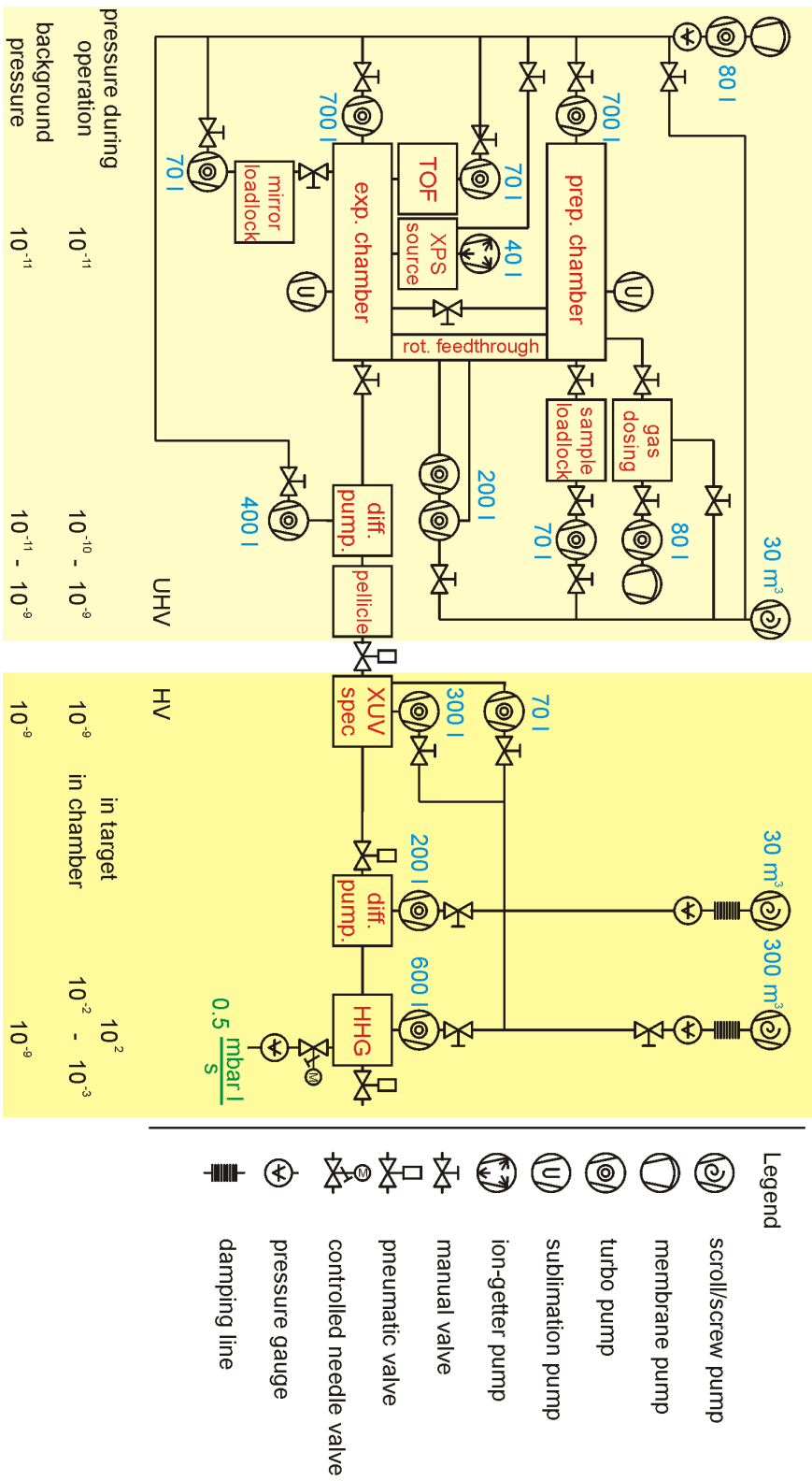


Figure 4.9.: Schematic vacuum layout of the AS3 beamline at MPQ, pressure values are given in mbar.

can reach 10^{-2} mbar, the complete beamline was designed to be UHV compatible. The base pressure without any load is below $5 \cdot 10^{-9}$ mbar everywhere in the setup. Normal materials would outgas at this value and contaminate the used optics and filters. All parts were therefore made out of materials suitable for UHV. Furthermore, all chambers of the UHV part of the beamline and main elements of the HV part are electro-polished. This minimises surface roughness on the inside of the chambers, lowers the amount of adsorbed gas atoms, and thus reduces the end pressure. Additionally, the pump-down time can be reduced. Venting is done with clean, liquid nitrogen on the UHV side of the beamline, with dry, clean nitrogen supplied from the houseline on the HV side. This reduces contaminations due to dirt or dust to a minimum.

The turbo pumps are attached directly to the chambers without any tubing in between, which minimises conductance losses. To reduce vibrations from the pumps, which could introduce jitter on the timing between the XUV and the NIR pulses, all large turbo pumps have magnetic bearings. The prepumps are not directly in contact with the vacuum setup, but the connecting hoses are guided through reservoirs filled with sand, which efficiently damp the vibrations. The optics which guide the beam to the experimental chamber are mounted on separate breadboards and are isolated from the vacuum chambers via bellows. This further minimises vibrations of the optical setup. Relative movements of the optics due to mechanical stress in the chambers during pump-down of the beamline are also omitted this way.

The layout for the HV part of the beamline is governed by the gas load of the HHG process. The pressure in the target, p_{HHG} , and the size of the hole in the Nickel tube, A_{spot} , define the gas flow of the HHG target into the chamber. The diameter of the focal spot of the NIR laser is approximately $90 \mu\text{m}$, using this the gas flow, q_{pV} , through two areas of that size is [70]

$$q_{pV} = p_{HHG}^2 \frac{A_{spot} \bar{v}}{4} \approx 0.5 \frac{\text{mbar l}}{\text{s}}, \quad (4.7)$$

where \bar{v} is the mean velocity of neon atoms at 300 K. In reality, this value is going to be a lower bound for the flow that has to be pumped. The hole size increases because the target is shifted along the beam axis to smooth out the edges which occur during burning the hole. As the pressure is kept constant, the net mass flow increases.

To efficiently pump the gas load, two turbo pumps with a differential pumping stage in between are used. Most of the load is pumped by a 600 l turbo pump directly at the HHG chamber (Leybold MAG W 600). This pump was chosen because it has a fairly good

throughput and maintains a pressure of $\approx 10^{-3}$ mbar with a load of 0.5 mbar l/s. Directly behind the HHG chamber, a differential pumping stage is realised with a skimmer with an opening of 1.5 mm. It prevents high gas flow out of the HHG chamber in direction of the experiment. After the skimmer a 200 l turbo pump (Pfeiffer TMU 200 MP) pumps the residual gas load of the HHG process.

Between the 200 l pump and the next element in the beamline, the XUV spectrometer, a 635 mm long CF16 tube was put in as a second differential pumping stage. This ensures that the residual gas through the skimmer is kept near the 200 l pump and does not travel further down the beamline. The pressure after this stage was measured as a function of the pressure in the HHG chamber. Figure 4.10 shows that there is almost no gas load of the HHG process present in the XUV spectrometer. When the pressure in the HHG chamber rises from $2 \cdot 10^{-4}$ mbar to $6 \cdot 10^{-3}$ mbar, the pressure in the spectrometer increases only from $6.9 \cdot 10^{-8}$ to $7.7 \cdot 10^{-8}$ mbar. This measurement was done without installing a pump at the spectrometer. An even better performance is reached in the final setup, where a pressure of below $5 \cdot 10^{-9}$ mbar can be maintained.

The XUV spectrometer is pumped with a 300 l turbo pump (Leybold MagW 300) at the mirrors and a 70 l pump (Pfeiffer TMU 071 YP) at the grating. The grating is pumped separately because the initial alignment of this part can be done independently of the rest of the beamline. Venting the part with the filters has to be done very slowly and carefully in order not to break the ultrathin foils. Additionally, if a CCD is used, the detector has to be pumped continuously to maintain proper vacuum conditions.

All turbo pumps in this part are backed with a 30 m³ scroll pump (Busch Fossa 0030), without gas load the backing pressure is at $5 \cdot 10^{-3}$ mbar. During experiments the 600 l pump at the HHG chamber is backed with a 300 m³ screw pump (Leybold Screwline SP 250). This does not significantly alter the pressure in the HHG chamber but reduces the backing pressure of all other turbo pumps and therefore lowers their driving current.

The transition from HV to UHV is done with a 400 l pump (Pfeiffer TMU 400 MPH) between the pellicle and the experimental chamber. The nitrocellulose pellicle emits water when it is pumped and contaminates the UHV. However, both the pellicle and the metal filter inset cannot be baked. Therefore, an empty chamber is put after the pellicle and serves as last differential pumping stage. This chamber is baked, the water from the pellicle is efficiently pumped there. Usually, a base pressure of 10^{-10} mbar can be achieved there after bakeout.

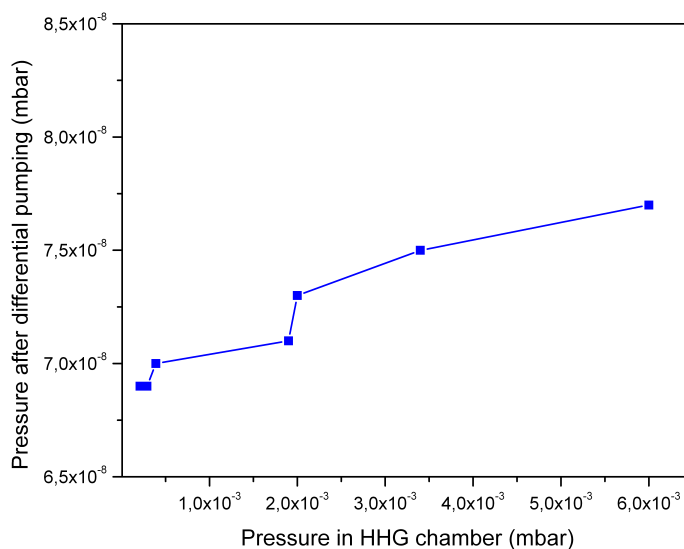


Figure 4.10.: Pressure after the differential pumping stage as a function of pressure in the HHG chamber. While the pressure right at the gas target varies by more than one order of magnitude, only a relative deviation of 12% can be measured after the differential pumping. Please note the different scales on the x - and y -axis.

The experimental chamber is not vented on a regular basis and does not have to handle any gas load. Therefore, a single 700l turbo pump (Leybold MAG W 700 iP) is sufficient to achieve UHV conditions in a reasonable amount of time despite the size of the chamber (volume of $\approx 0.4\text{m}^3$). To achieve pressures in the 10^{-11} mbar range, an additional liquid-nitrogen cooled titanium-sublimation pump (VAb TVP 40K, LN200) is attached to the chamber. This pump is operated only during experiments. A second, identical scheme pumps the preparation chamber. The whole UHV part is also baked to efficiently pump water, which sets one lower limit to the pressure. Baking is done with heattapes locally attached to the chambers and detectors and a programmable controller (Horst, R2500). Usually, the experimental chamber is heated to 100 C, the preparation chamber to 200 C for 4 – 5 days. The temperature on the experimental side is limited by the piezo motors and the multilayer mirror, which cannot withstand higher temperatures without being damaged.

To ensure the operation of the MCP in the TOF detector and the filament in the XPS source also when the pressure in the experimental chamber is high (in case gaseous

targets are investigated), those two parts are pumped differentially. A 70l turbo is attached to the TOF detector directly at the detector, and a 40l ion getter pump is mounted on the XPS source. The gas dosing system and the gas target are pumped separately, each by a turbo pump station (Pfeiffer HiCube 80 Eco).

The double-mirror and the sample can be exchanged via two loadlocks. The complete mirror stack can be pulled out of the chamber through a CF 250 port and separated from the experiment with a valve. This way, only the small volume is vented and has to be baked afterwards. The manipulator is pumped with a 70l turbo pump, the backing is done with the same turbo pump station as for the UHV system (complete design by E. Bothschafter and R. Ernstorfer). The sample can be transferred to a linear feedthrough and retracted in a separate CF 40 cross in case the sample has to be changed. This cross is pumped with a 70l turbo. The cross is vented with pressurised nitrogen, which is kept running until the cross is pumped down again. The high flow of pure nitrogen prevents water from entering the load lock. Therefore, the loadlock does not have to be baked after venting, allowing for a sample exchange in about one hour.

The turbo pumps of the UHV part are backed with a combined system of a 70l turbo pump and a membrane pump (Pfeiffer HiCube 80 Eco). If the chambers have to be evacuated from atmospheric pressure, the turbo pump station is by-passed and a scroll pump (Busch Fossa 0030) pumps the high gas load.

Another crucial point in terms of vacuum design is the dynamic sealing of the rotational feedthroughs for the experimental and preparation chamber. The connection between the fixed and rotational parts of the chambers has to isolate the vacuum against the atmospheric pressure and at the same time support a relative rotation between those parts. The concept of these feedthroughs was devised by P. Feulner (E20, TUM), figure 4.8 (b) in the previous subsection shows a sketch of the design: The motion is guided with a bearing at the atmospheric side. Three sealing rings with a leak rate of 10^{-4} mbarl/s per ring isolate the vacuum chamber from the environment. The space between the sealings is used for differential pumping with a 200l split flow turbo pump (Pfeiffer TMH 261, split flow model). The pressure is monitored only at the high vacuum stage near the pump, here a value of 10^{-6} mbar is maintained. This level ensures UHV conditions of 10^{-10} mbar inside the chamber for all times, even during rotation of the feedthroughs.

The pressure in the setup is monitored continuously both in the vacuum chambers and in the backing lines. Piezo resistive sensors are used for the backing line, full range sensors and cold cathodes for the HV part, cold cathodes and ion gauges for the UHV

chambers. Additionally, two quadrupole mass spectrometers (Pfeiffer QMG 220 Prisma Plus) are attached to the experimental and preparation chamber to analyse residual gases.

4.2.6. Preparation tools and sample control

The sample is cleaned and prepared in a separate chamber which can be isolated from the experimental chamber with a valve. The preparation chamber is equipped with a sputter gun (SPECS, IQE 11/35) for cleaning. Different gases can be fed to the sputter gun via a home-built gas dosing system. This dosing system in combination with a flow controller (S. Neppel, TUM, E20) is also used for adsorbing gases on the sample. An evaporator (S. Neppel, TUM, E20) allows for depositing solid materials. The necessary mass flux for a controlled layer growth of different materials is calibrated in temperature programmed desorption measurements (TPD) with a desorption sensor. Details on the preparation tools will be given in S. Neppel's thesis. The crystal structure of the surface can be measured with LEED (SPECS, ErLeed 100/150), analysis of the surface composition can be done with XPS (SPECS, XR50), the latter one is situated in the experimental chamber.

The sample is mounted on a manipulator with four degrees of freedom, three translational ones and one rotation around the manipulator axis. The mounting flange of the manipulator can be rotated as well to reach all preparation and diagnostic tools. Both rotational motions and the translation along the axis are motorised. The manipulator has a travel range of 1 m along its axis and of 6 cm in the plane perpendicular to it. A rotation of 360° of both sample and manipulator flange is in principle possible and only restricted in the latter case by equipment attached to the chamber.

The design and the construction of the manipulator and the sample head was done by S. Neppel and P. Feulner (TUM, E20), details will be given in S. Neppel's thesis. The manipulator is a stainless steel tube with a silver rod soldered on the end. The head carrying the sample is connected to the silver head with screws and is isolated electronically from it by a sapphire plate. The silver end has a fan-like capillary structure inside, where liquid helium or nitrogen used for cooling is distributed efficiently, the sapphire plate ensures efficient heat transfer to the head. Two filaments below the sample are used for radiative heating of the crystal or for electron bombardment if the sample is put on high voltage (1 kV). The temperature range achieved with this setup

extends from 20 K up to 3000 K and is limited on the high end by the thermionic current provided from the two filaments.

The temperature of the sample is measured with two pairs of thermocouples. A type T (tungsten/rhenium) thermoelement is spotwelded to the sample and connected to copper wires with gold contacts. To get the reference of the thermoelectric voltage for the connecting point, the circuit is symmetrised by inserting a tungsten wire between one gold contact and the rhenium. The temperature of the connecting point is measured with a second type K (chromel/alumel) thermocouple and is used to correct the thermoelectric voltage measured at the sample. With this floating reference, one is flexible to chose the thermoelement at the sample appropriate to the desired temperature range and accuracy. As a part of the manipulator, the temperature control was also done by P. Feulner and S. Neppl, for details please refer to S. Neppl's thesis.

5. Theoretical tools and data analysis

Within the framework of this thesis, not only experimental work was done, but the origin of the delayed photoemission was also investigated theoretically. The model of transport of the photoelectrons in a band structure was further pursued. Additionally, the electronic coupling between the substrate material and a rare gas reference layer was investigated qualitatively. Density functional theory was used as a theoretical tool for both tasks utilising the commercially available software package WIEN2k [71]. The basic assumptions of density functional theory are described in the first subsection of this chapter. The way of deriving the formalism is adapted from [72].

Also, the concept of data processing and how parameters like the relative delay between two photoelectron peaks or laser pulse parameters can be extracted out of a streaking measurement is explained in the second subsection this chapter.

5.1. Introduction to density functional theory

5.1.1. Obtaining the Kohn-Sham Hamiltonian

The theoretical treatment of solid state systems within quantum mechanics is an extremely difficult task because of the high number of particles involved. The complete Hamiltonian for such a system of more than $6 \cdot 10^{23}$ particles,

$$\begin{aligned}
 \mathfrak{H}_{full} = & \underbrace{-\frac{\hbar^2}{2} \sum_i \frac{\Delta_{\vec{R}_i}^2}{M_i}}_{\mathfrak{T}_{nuc}} - \underbrace{\frac{\hbar^2}{2} \sum_i \frac{\Delta_{\vec{r}_i}^2}{m}}_{\mathfrak{T}_e} - \\
 & - \underbrace{\frac{1}{4\pi\epsilon_0} \sum_{i,j} \frac{e^2 Z_i}{|\vec{R}_i - \vec{r}_j|}}_{\mathfrak{V}_{e-nuc}} + \underbrace{\frac{1}{8\pi\epsilon_0} \sum_{i \neq j} \frac{e^2}{|\vec{r}_i - \vec{r}_j|}}_{\mathfrak{V}_{e-e}} + \underbrace{\frac{1}{8\pi\epsilon_0} \sum_{i \neq j} \frac{e^2 Z_i Z_j}{|\vec{R}_i - \vec{R}_j|}}_{\mathfrak{V}_{nuc-nuc}}, \quad (5.1)
 \end{aligned}$$

consists of the kinetic energies of nuclei and electrons, \mathfrak{T}_{nuc} , \mathfrak{T}_e , the Coulomb attraction between electrons and nuclei, \mathfrak{V}_{e-nuc} , and the Coulomb repulsion between electrons and electrons, \mathfrak{V}_{e-e} , and nuclei and nuclei, $\mathfrak{V}_{nuc-nuc}$, respectively. Capital letters denote the masses and position vectors of the nuclei, Z_i is the atomic number, small letters denote the position vectors of the electrons.

A Schrödinger equation with this Hamiltonian is impossible to solve exactly, several approximations can be made in order to obtain a simplified Hamiltonian. Depending on the specific problem different assumptions enter the approximations, which lead to a reasonable simplification of the initial operator. One approach, the so-called density functional theory (DFT), is mainly used in solid state physics.

The first step, which can be made in essentially all fields not only within DFT, is the Born-Oppenheimer approximation: It is assumed that the nuclei are much heavier than the electrons and stay fixed at their positions. This removes the first term in (5.1) and reduces the last one to a constant. The remaining Hamiltonian,

$$\mathfrak{H} = \mathfrak{T}_e + \mathfrak{V}_{e-e} + \mathfrak{V}_{ext}, \quad (5.2)$$

can now be divided in two parts: firstly, the kinetic energy of the electrons and the electron-electron interaction; secondly, the potential energy of the electrons in the field of the nuclei. The first part is independent of the specific problem and takes the same shape for all systems. Information on the system is only contained in the second part, describing the interaction of the electrons with an external potential. Now, the two Hohenberg-Kohn theorems, which are the foundation of DFT, can be applied [73]. They state the following:

1. There is a one-to-one correspondence between the external potential V_{ext} of a many-electron system and its ground state density $\rho(\vec{r})$. Consequently, the ground state expectation value of any observable is a unique functional of the exact ground state electron density.

2. The ground state total energy functional can be written as

$$E_{V_{ext}}[\rho] = \langle \Psi | \mathfrak{T}_e + \mathfrak{V}_{e-e} | \Psi \rangle + \langle \Psi | \mathfrak{V}_{ext} | \Psi \rangle = F_{HK}[\rho] + \int d\vec{r} \rho(\vec{r}) V_{ext}(\vec{r}), \quad (5.3)$$

where the Hohenberg-Kohn functional $F_{HK}[\rho]$ is universal for any many-electron system. $E_{V_{ext}}$ reaches its minimal value for the ground state density ρ corresponding to a specific V_{ext} .

The first theorem tells us that we can reconstruct the unique external potential if a ground state electron density is given. The density of the ground state contains exactly the same information as the full wavefunction: We are allowed to work with the density and its functionals only, reducing the problem to 3 spatial coordinates, instead of $3N$ coordinates in the initial N -particle Hamiltonian in (5.2). The second theorem allows for using the variational principle of Rayleigh-Ritz to find the ground state density of a system. Additionally, it provides an explicit expression for the contribution of the external potential to the total energy. However, the exact shape of the Hohenberg-Kohn density functional remains unknown.

Therefore, we look now only at $F_{FK}[\rho]$, meaning we are not dealing with operators any more, but with functionals. To obtain the exact value of the kinetic and potential energy of a many-electron system, one has to include electron-electron interaction, the so-called exchange and correlation energies. Exchange is a consequence of the Pauli principle, which prohibits two electrons with parallel spins being in the same quantum state. Correlation in this context here is the complete electron-electron interaction without exchange. Both result from the initial Hamiltonian due to the shape of the Coulomb operator and the fact that the full Hamiltonian is acting on a non-separable wavefunction. The Hohenberg-Kohn functional is rewritten in a way that allows for using known quantities from single-particle approximations: Let

$$\begin{aligned} F_{HK} &= T + V \\ E_{sp} &= T_0 + V_0 \end{aligned} \tag{5.4}$$

be the Hohenberg-Kohn energy functional, F_{HK} , depending on the kinetic and potential energy functionals, T and V , of the full system, and the single particle energy functional, E_{sp} , of a non-interacting system which does not account for exchange and correlation. The Hohenberg-Kohn functional can be rewritten to

$$F_{HK} = T_0 + V_0 + V_{XC} \tag{5.5}$$

with V_{XC} being the (unknown) exchange-correlation contribution which is missing in the single particle functionals. The total energy is accordingly

$$E_{V_{ext}} = T_0 + V_0 + V_{XC} + V_{ext}. \tag{5.6}$$

We can interpret this total energy functional as energy functional of a non-interacting

electron gas, with the Kohn-Sham Hamiltonian of

$$\begin{aligned}\mathfrak{H}_{KS} &= \mathfrak{T}_0 + \mathfrak{V}_0 + \mathfrak{V}_{XC} + \mathfrak{V}_{ext} \\ &= -\frac{\hbar^2}{2m_e} \Delta_{\vec{r}} + \frac{e^2}{4\pi\epsilon_0} \int d\vec{r}' \frac{\rho(\vec{r}')}{|\vec{r} - \vec{r}'|} + \mathfrak{V}_{XC} + \mathfrak{V}_{ext}\end{aligned}\quad (5.7)$$

acting on a single-particle wave function. The exchange-correlation operator is obtained with the variation of the exchange-correlation energy:

$$\mathfrak{V}_{XC} = \frac{\delta V_{XC}[\rho]}{\delta \rho}. \quad (5.8)$$

If we now use the second theorem of Kohn and Sham, we can construct the ground state density, $\rho(\vec{r})$, of an N-electron system

$$\rho(\vec{r}) = \sum_{i=1}^N |\phi_i\rangle \langle \phi_i| \quad (5.9)$$

out of the solutions $|\phi_i\rangle$, which solve the Kohn-Sham equation with the N lowest energies:

$$\mathfrak{H}_{KS} |\phi_i\rangle = \epsilon_i |\phi_i\rangle. \quad (5.10)$$

We have now achieved two things: We have reduced the initial $3N$ coordinates to 3, and we have to solve only single-particle Schrödinger equations, where the procedure is well known. Additionally, the solution is in principle exact. Apart from the Born-Oppenheimer approximation made in the beginning, no interactions are excluded. However, the calculated wavefunctions $|\phi_i\rangle$ are not real electron wave functions and do not have any physical meaning. The only physical quantity is the density.

We still did not give an explicit expression of the exchange-correlation interaction, whose form is not known. This is the second point where approximations enter DFT. A possible approximation is the local density approximation (LDA) which assumes that the local exchange-correlation energy $\epsilon_{XC}(\rho(\vec{r}))$ of a small volume depends only on the local density and is as strong as the exchange-correlation of a uniform electron gas. This can be calculated numerically

$$V_{XC}^{LDA} = \int d\vec{r} \rho(\vec{r}) \epsilon_{XC}(\rho(\vec{r})) \quad (5.11)$$

This assumption works reasonably well not only for systems with a slowly varying density but also for others. The next logical extension is to take not only the local density but

also the gradient into account. This is then called generalised gradient approximation (GGA) and is the mostly used approach today [74]. Both methods are implemented in different flavors in WIEN2k, it is indicated for each calculation which one was used.

5.1.2. Solving the Kohn-Sham equations

In equation (5.7), both the exchange-correlation and the Coulomb interaction depend on the electron density, which again depend on the wavefunctions. This is a self-consistency problem and is solved in an iterative procedure, the so-called self-consistency cycle: An initial ρ_0 is guessed, which determines the complete Hamiltonian. The solutions are used to derive a density ρ_1 , which is compared with the initial one. If the difference between those two is larger than the desired convergence value, the procedure is repeated with ρ_1 as starting point. This is done until the density converges to a final ρ_f which generates a Hamiltonian that gives within a tolerance interval the same ρ_f as a solution.

In order to solve a Schrödinger equation like (5.7) in a periodic potential one usually expands the wavefunctions ϕ_i in a complete basis set which has the same periodicity as the potential:

$$\phi_{\vec{G}}^{\vec{k}}(\vec{r}) = \sum_{\vec{G}} c_{\vec{G}}^{n,\vec{k}} \exp\left(i(\vec{k} + \vec{G}) \cdot \vec{r}\right). \quad (5.12)$$

\vec{G} and \vec{k} are vectors in reciprocal space, \vec{G} is a reciprocal lattice vector, \vec{k} is restricted to the first Brillouin zone. The sum has to be truncated, which means we take only a finite number of vectors up to a maximum length $|\vec{G}|_{max}$ into account. This basically determines the spatial resolution of the result. The $|\vec{G}|_{max}$ eigenvalues found to each basis function correspond to different energy bands at a fixed \vec{k} .

In case of solid state problems it is reasonable to use two different sorts of basis functions, depending on if they should represent the wavefunction near an atomic core or far away from it: Very close to a nucleus, the solution will be oscillating rapidly due to the strong Coulomb potential. Far away, we expect it to behave more smoothly. Consequently, we divide space in two regions: each atom is surrounded by a sphere S with radius R_{MT} , the so-called muffin-tin radius. The remaining space is called the interstitial region, I . In the interstitial, the wavefunctions are represented as plane waves, inside the spheres, they are described by a superposition of atom-like functions. There are different methods which atom-like functions are chosen and how their boundary conditions at the

interface to the interstitial are set. Depending on the basisfunctions the diagonalisation of the Kohn-Sham Hamiltonian has to be done formally in different ways. Also, the result might converge slightly better or worse to the exact solution. The set of basisfunctions therefore affects the obtained result, and it should be paid attention to which basis was used when different results are compared. In WIEN2k, the basis functions, which are mostly used, are linearised augmented plane waves (LAPW):

$$\psi_{\vec{G}}^{\vec{k}}(\vec{r}) = \begin{cases} \frac{1}{\sqrt{V}} \exp(i(\vec{k} + \vec{G}) \cdot \vec{r}) & \vec{r} \in I \\ \sum_{l,m} \left(A_{l,m}^{\vec{k}+\vec{G}} u_l(r, E_{1,l}) + B_{l,m}^{\vec{k}+\vec{G}} u'_l(r, E_{1,l}) \right) Y_m^l(\theta, \phi) & \vec{r} \in S \end{cases} \quad (5.13)$$

V is the volume of the unit cell, l, m are the quantum numbers of angular momentum, u_l are solutions to the radial part of the Schrödinger equation for a free atom, with $E_{1,l}$ being the eigenvalue of the desired band, and Y_m^l are spherical harmonics. The coefficients $A_{l,m}$ and $B_{l,m}$ are determined via the boundary condition that the overall wavefunction has to behave smoothly in value and in slope at the interface to the interstitial. The matching can be done exactly only for an infinite number of l . In reality, the cut-off G_{max} of the plane waves and l_{max} of the angular functions are comparable, if their number of nodes per unit length is the same. This sets $l_{max} = R_{MT}G_{max}$. This is not a strict mathematical condition, it is only a reasonable limit, but it should be considered when a DFT calculation is set up.

The above basis set behaves reasonably well for almost all states, only valence states with d and f characters are difficult to describe. Therefore, for these states an - optional - local orbital (lo) defined for a particular l and m with a specific $E_{2,l}$ can be added:

$$\psi_{lo}^{lm}(\vec{r}) = \begin{cases} 0 & \vec{r} \in I \\ (A_{lm}^{lo} u_l(r, E_{1,l}) + B_{lm}^{lo} u'_l(r, E_{1,l}) + C_{lm}^{lo} u_l(r, E_{2,l})) Y_m^l(\theta, \phi) & \vec{r} \in S \end{cases} \quad (5.14)$$

Here, the coefficients have to make sure that the local orbital vanishes at the sphere boundary (but not its slope) and that the local orbitals are normalised.

The potential is represented as a superposition of basisfunctions as well, following the same splitting in muffin tin and interstitial regions as the wavefunction. WIEN2k does not make any approximations here, the potential is included exactly, making the program a so-called full-potential code. Additionally, all calculations include scalar relativistic corrections, the Darwin s-shift and relativistic mass enhancement. Spin-orbit coupling can be considered where necessary.

5.1.3. Calculated quantities

In the framework of this thesis, the WIEN2k package is mainly used to calculate two properties: the band structure and the valence electron density of a specific system.

The band structure is calculated to compare measured time delays with values obtained from computed transport times in a crystal potential. Although the energy eigenvalues of the Kohn-Sham equation are eigenvalues of an imaginary single-particle system and not one-electron energies of the electron in the solid, they represent the band structure below the Fermi-edge reasonably well. As DFT was developed to calculate quantities of a system in its ground state, it is questionable, in what extent band structure calculations above the Fermi energy are valid. Usually, the dispersion shows high agreement with experimental values, only the absolute value along the energy axis might be displaced. This can in principle be corrected with some scaling after comparisons with measurements like inverse photoemission are made [75].

The spatial distribution of the valence electron density is compared for clean metal surfaces and metal surfaces with an additional layer of xenon on top. If there is a significant electronic influence of the xenon adlayer on the metal and vice versa, this is going to show up in a redistribution of the outermost electrons. Additionally, this should also be visible in the density of states (DOS) of occupied states, which is therefore calculated via the band structure as well.

5.2. Data evaluation

If a spectrogram like the one displayed in figure 3.1 is recorded, there are several ways how to extract information of it. In case of gas phase streaking experiments, the FROG-CRAB method (frequency resolved optical gating for complete reconstruction of attosecond bursts) has proven to be an accurate and stable routine [45, 46]. However, solid state targets cannot be treated with the same theoretical tools a priori due to their different electronic structure. The FROG-CRAB algorithm assumes every trace in a spectrogram to be a coherent superposition of electrons. In case of the conduction band in a metal, this is obviously not true as the photoelectron peak is composed of a large number of different electronic states, which cannot interfere with each other. Therefore, other methods are applied within this thesis.

A synthetically generated spectrogram of two electron peaks on top of a quadratic

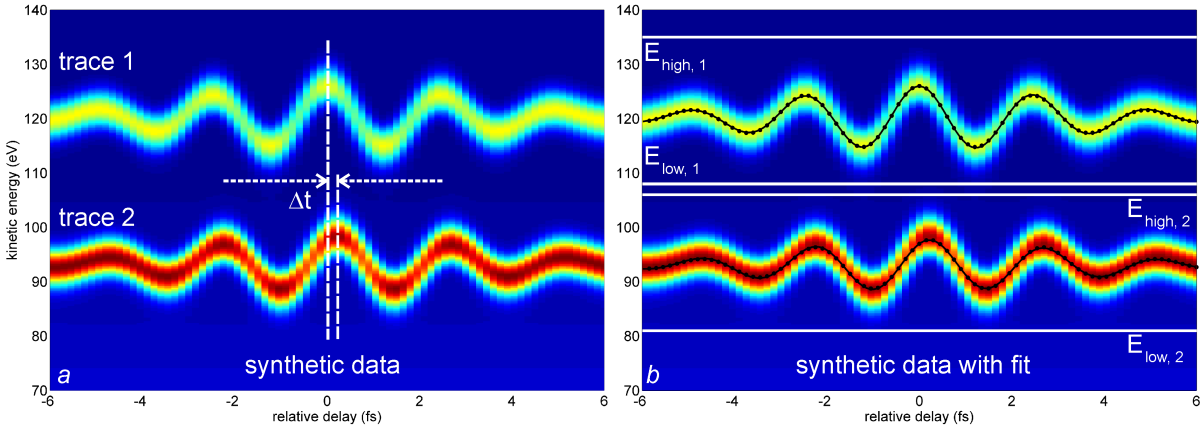


Figure 5.1.: Synthetically generated spectrogram of two streaked photoelectron peaks centered at 120 and 93 eV respectively, with a quadratic background. The time delay between the traces was set to 200 as. The regions of interest for each trace along the energy axis are indicated with horizontal lines E_{high} and E_{low}

background is displayed in figure 5.1 a, where the time difference between the two traces was set to be 200 as for demonstration purposes. In order to get the timing of the different photoelectron features in a measured spectrogram, different assumptions on the peaks, their shapes and their behavior in the streaking field can be made. We applied three different analysis methods: The center of mass analysis, a peak fitting method, and the analytical solution of the Schrödinger equation in the strong field approximation. It is indicated for each result with which method it was obtained.

5.2.1. Center of mass analysis

The center-of-mass (COM) is an extremely versatile and unbiased approach to get timing information of a spectrogram. In order to calculate the COM of a streaking trace the spectrogram is divided in regions of interest along the energy axis, $E_{low} - E_{high}$, confining an individual photoelectron trace, see figure 5.1 b. The COM of each trace is then calculated for each time step t_i via the first moment of the electron count signal, *counts*, of the TOF detector:

$$COM(t_i) = \frac{\sum_{E_{low}}^{E_{high}} counts(E, t_i) \cdot E}{\sum_{E_{low}}^{E_{high}} counts(E, t_i)}. \quad (5.15)$$

The COM itself does not assume any shape of the photoelectron peaks, no parameters which could bias the result, are introduced here. Additionally, it is relatively insensitive to any background.

The calculated positions of the COM in each trace and for each time step are displayed as filled circles in figure 5.1 b. They are then used for a fit of the NIR vector potential: According to equation (2.14), the kinetic energy of the electrons is directly proportional to the NIR laser vector potential. Therefore, the calculated COMs of each trace can be used to form a laser pulse along the delay axis:

$$\begin{aligned} E_{kin1}(t) &= \Delta E_1 \exp\left(-\frac{(t-t_0)^2}{\Delta T_{NIR}^2}\right) \sin(\omega t + \beta t^2 + \phi_0) + \delta E t + E_1 \\ E_{kin2}(t) &= \Delta E_2 \exp\left(-\frac{(t-t_0)^2}{\Delta T_{NIR}^2}\right) \sin(\omega t + \beta t^2 + \phi_0 + \phi_{12}) + \delta E t + E_2 \end{aligned} \quad (5.16)$$

$\Delta E_{1,2}$ describe the streaking amplitude of the respective trace. They have to be set differently in each trace because the streaking strength also depends on the mean kinetic energy of the streaked electron. t_0 denotes the maximum of the NIR pulse envelope, ΔT its FWHM pulse length. ω is the carrier angular frequency, β accounts for possible chirp, which could have originated in the HHG process. ϕ_0, ϕ_{12} are CEP values whose meaning will be clarified in the next paragraph. δE accounts for a linear tilt of the whole trace, caused by space charge due to low energy electrons. E_1 and E_2 finally are the mean kinetic energies of the electrons in each trace. The resulting fit is displayed as solid line in figure 5.1 b.

Usually, the fitted streaking amplitude can not be directly translated to the amplitude of the NIR vector potential. If the peaks sit on a background, as they do in solid state streaking measurements due to inelastically scattered electrons, the amplitude of the COM fit is according to its definition smaller than the one of the original signal. This can be seen in the lower energetic trace in figure 5.1 b, where the filled circles do not exactly follow the streaking trace, especially around zero relative delay. This effect is enhanced in real, measured data, where the inelastic background is larger than the displayed one. The COM fit can in principle be scaled to follow the measured trace, but this can only give a rough idea of the order of magnitude of the NIR field, not an accurate

value. The intensity can be retrieved accurately only with the peak fitting method or the solution of the Schrödinger equation.

In the fit here, the pulse center in time is assumed to be identical for both pulses, the timing is extracted from different CE phase values, ϕ_0 and ϕ_{12} . ϕ_0 denotes the phase of the first trace, ϕ_{12} is a deviation in the second trace from this value. The timing difference is extracted out of ϕ_{12} . This is not the correct physical picture. The CE phase remains the same for all traces, only the time zero of the envelope changes. It turned out to be very difficult to get reasonable fits for that: The change of time zero of the envelope is on the order of attoseconds whereas the absolute time zero ranges on the femtosecond scale. This results in a fit of a sum of two parameters which differ by a factor of 100. It is possible to obtain reasonable fitting results with this, but the starting parameter have to be chosen very carefully and the fit needs a lot of iterations. The algorithm reacted much more sensitively on changes in the CE phase. Both fitting methods were applied to the same synthetically generated spectrograms, they return the same time delay if it is smaller than 300 as. Therefore, the method described with equation (5.16) was chosen.

The parameters of equation (5.16) are optimised in a global fit with a least squares algorithm provided by Matlab. Standard error bars of the time delay are calculated out of the 95% confidence intervals of the fit. For more than two traces, another function of the form (5.16) is added, the overall procedure remains the same.

5.2.2. Peak fitting

To overcome the problem that the traces found with the COM analysis have to be scaled in amplitude to follow the NIR vector potential, the streaking spectrograms can be fitted with different peak functions. Here, the spectrogram is again divided into different regions of interest, but instead of calculating the COM, the energy spectrum is fitted with a specific peak function: The peak fits optimises the parameters for a given peak shape within the region of interest for each trace and for each delay step individually. There are no links between the parameters, only the general peak shape remains the same throughout the whole trace (but can be chosen differently for different traces). These functions can include some basic background as well, e.g. a symmetric Gaussian peak on a second-order polynomial background was used for some of the results presented in this thesis:

$$y = a_1 \exp \left(-4 \ln 2 \left(\frac{E - a_3}{a_2} \right)^2 \right) + a_4 + a_5 E + a_6 E^2, \quad (5.17)$$

where the parameters a_1 to a_3 denote the peak amplitude, the FWHM width, and the peak center, and the parameters a_4 to a_6 define the background. Once all peaks are defined, their maxima serve as sampling points for fitting the shape of the NIR pulse. The following procedure is the same as for the COM. The traces found here follow the measured ones without any scaling. The parameters for the NIR pulse, especially its amplitude $\sim \Delta E_{1,2}$, can be therefore used for further investigations.

5.2.3. Spectrogram retrieval

The most severe restrictions of the peak fitting methods are that the properties of the XUV pulse are not taken into account at all and that the spectrogram is sliced in pieces along the delay axis and not treated as whole. One way to overcome these problems is to construct a spectrogram according to the analytical results of the time dependent Schrödinger equation in an external field and optimise the parameters until the resulting spectrogram resembles the measured one. This was done by N. Karpowicz, a member of our research group, his retrieval method was used for most of the results presented in this thesis.

If we neglect the influence of the Coulomb potential of the ionised system on the free electron (strong field approximation), the time dependent Schrödinger equation in an external laser field

$$\frac{1}{2} \left(\hbar \vec{\nabla} - \frac{e}{c} \vec{\mathcal{A}}_{NIR} \right)^2 |\psi\rangle = i \partial_t |\psi\rangle \quad (5.18)$$

can be solved yielding the Volkov solutions:

$$\begin{aligned} |\psi(t)\rangle &= \exp(-i\phi_v) |\psi(t_0)\rangle \\ \phi_v &= \frac{1}{2} \int_{t_0}^t dt' \left(p - \frac{e}{c} \mathcal{A}_{NIR}(t') \right)^2 \\ &= \int_{t_0}^t dt' \left(E_0 + \sqrt{2E_0} \mathcal{A}_{NIR}(t') + \frac{1}{2} \mathcal{A}_{NIR}^2(t') \right) \end{aligned} \quad (5.19)$$

The first term in the Volkov-phase ϕ_v describes the initial state with energy E_0 , the second term is the streaking process due to the NIR laser, the third term accounts for

asymmetries in the streaking curve, which are visible only for very high NIR intensities. In the second term we applied the Coulomb gauge which allows us to set the divergence of the vector potential equal to zero. The energy E_0 of the unstreaked electron depends on the ionisation potential of the electrons and the XUV photon energy. In the algorithm, the XUV photon energy is fixed to the central energy of the multilayer mirror. A linear drift for space charge, which was added to the NIR vector potential for the peak fits, is included here as well.

The Schrödinger equation above did not include the shape of the electron wave packet when it is released into the NIR field. It is reasonable to assume that it will resemble the features from the XUV pulse. The complete, streaked wave packet will therefore look like this in the time domain:

$$\Psi(t) = I_{XUV}(t) \exp(-\beta_{XUV}t^2) \exp(-i\phi_v) \quad (5.20)$$

For the intensity profile of the XUV pulse, $I_{XUV}(t)$, a gaussian or a hyperbolic secants function is chosen. β_{XUV} takes into account that the XUV pulse has an intrinsic chirp due to the HHG mechanism. The NIR field has a similar shape as in equation (5.16)

$$\mathcal{A}(t) = \mathcal{A}_0 \exp\left(-\left(\frac{t-t_0}{\Delta T}\right)^2\right) \sin(\omega t + \beta_{NIR}t^2 + \phi_0) \quad (5.21)$$

In order to retrieve an energy spectrum from equation (5.20) the wave packet is Fourier transformed, the absolute square is equivalent to one trace of the measured spectrogram. Two or more traces are then added together to construct the complete spectrogram. For each trace, the parameters of the NIR field are the same except for t_0 which essentially gives the time delay between the traces. Almost all parameters of the XUV wave packet are different for each trace, only the XUV central energy and the pulse length are set to the same values.

The parameters showing up in equations (5.20) and (5.21) are then optimised in a least squares algorithm. To enhance the streaking with respect to the background, the least squares algorithm uses the derivative along the delay axis to calculate the deviation between measured and retrieved spectrogram. The error for the relative time delay is again calculated via the 95% confidence interval.

In the procedure shown here, all initial states have delta like energy levels. It is possible to replace the single energy level with a calculated density of states. The kinetic energy of the unstreaked electron E_0 is then a superposition of several delta peaks with different

amplitudes. This DOS is kept fixed during the least squares algorithm. It is indicated explicitly when this was used instead of a single ionisation potential.

6. Streaking experiments of solids

6.1. Materials

The results presented here in this thesis were measured on two different systems, on clean, single-crystal metal surfaces, and on clean, single-crystal metal surfaces coated with a single layer of a rare gas. The properties of each system are described in the following subsections.

6.1.1. Tungsten and rhenium single crystals

Two metals were investigated in the frame of this work, tungsten and rhenium. Both provide a core state which can be excited with the available XUV energies, and the separation between core state and conduction band is large enough to resolve both peaks with broadband attosecond pulses.

Tungsten is a transition metal, atomic number 74, with 6 valence electrons. A photoelectron spectrum, recorded at 1.487 keV (Al $k\text{-}\alpha$) is shown in figure 6.1 (courtesy of S. Neppl). It features a broad conduction band of 10 eV and sharp core states at ≈ 32 eV ($4f$) and 37 eV ($5p_{3/2}$) below the Fermi energy. The $4f$ states are split because of spin-orbit coupling. A convolution of the spectrum with a 4–6 eV broad gaussian peak results in two broad peaks from the core states and the conduction band respectively. The individual components cannot be resolved anymore, the conduction band broadens to an ≈ 14 eV feature. The two peaks are separated by 29 eV and can clearly be distinguished. The work function of the tungsten (110) surface is on the order of 5 eV [76].

The crystal structure of tungsten is bcc, with a lattice constant of $a = 3.17$. Figure 6.2 (a) shows the first Brillouin zone of the reciprocal lattice and the (110) surface, which was investigated. The separation between two bulk layers along the (110) direction is $a/\sqrt{2} = 2.24 \text{ \AA}$.

Rhenium is the next element after tungsten in the periodic table (atomic number 75,

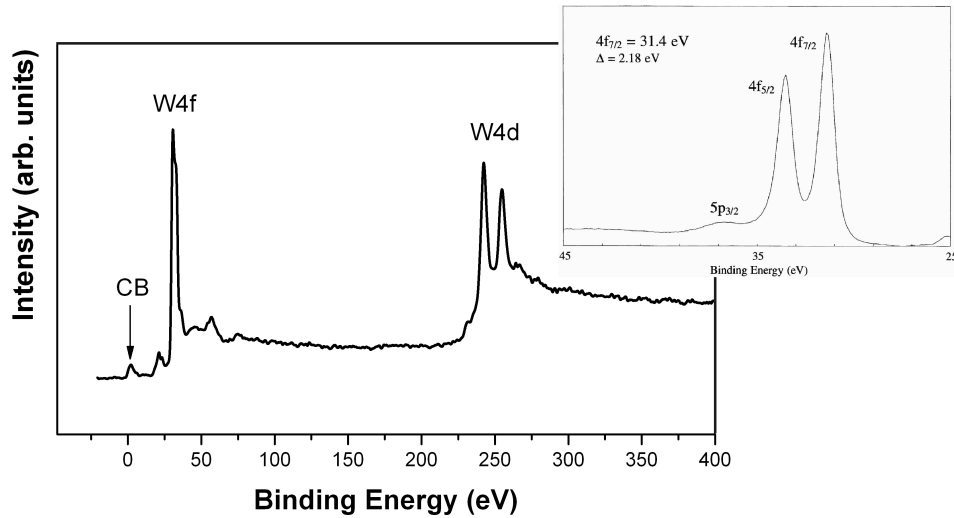


Figure 6.1.: Spectrum of a clean $W(110)$ surface, recorded with $Al\ K\text{-}\alpha$ radiation (courtesy of S. Nepl, inset adapted from [77]).

7 valence electrons). It features a similar photoelectron spectrum like tungsten: The conduction band is 10 eV broad, the core states lie at 41 eV binding energy. The core states originate from the atomic $4f$ level, again split due to spin-orbit coupling. The next core levels ($5s$) lie at much higher binding energies than the ones in tungsten (99 eV) and are not observed in the streaking measurements. The two $4f$ states merge again to one feature when the spectrum is convolved with a 4 – 6 eV gaussian peak. The conduction band and the $4f$ core states are separated by 41 eV, 12 eV more than in pure tungsten. The work function of poly-crystalline rhenium is 4.72 eV [76].

Rhenium has an hcp crystal structure, the lattice constants are $a = 2.76\ \text{\AA}$ and $c = 4.46\ \text{\AA}$. The first Brillouin zone and the investigated (0001) surface are displayed in figure 6.2 (b). The separation between two layers in the bulk along the (0001) direction is $c = 2.23\ \text{\AA}$.

The cleaning procedure for both samples is very similar [79, 80]. The samples were sputtered with argon ions at 1 kV for about 30 - 60 minutes to remove surface impurities and adlayers, the ion current measured during the procedure was $\approx 30\ \mu\text{A}$. Afterwards, the crystal was flashed several times to 2000 K to restore the crystal structure. The main contaminant remaining on the surface is carbon. Cleaning cycles of annealing in oxygen at $6 \cdot 10^{-7}$ mbar and 1600 K were repeated up to 20 times to ensure that the

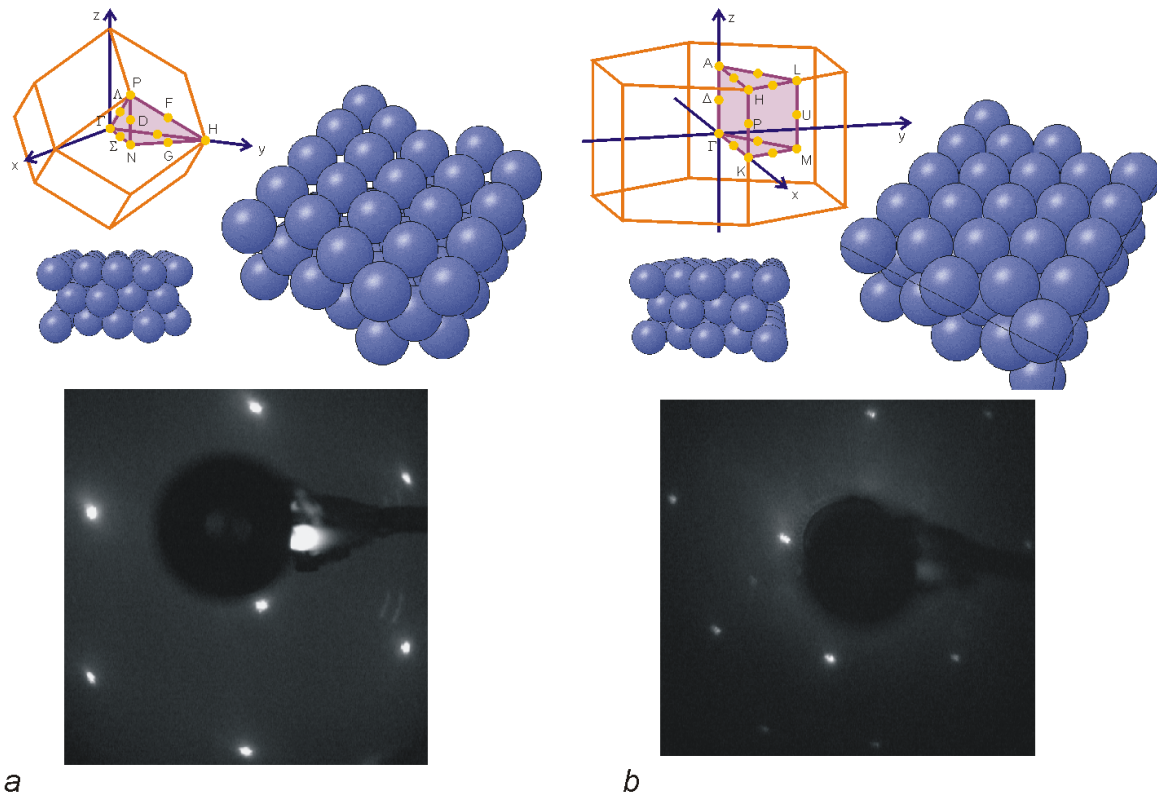


Figure 6.2.: First Brillouin zone with irreducible wedge and top and side view [78] of a bcc (110) (a) and an hcp (0001) (b) surface. In the lower panel LEED measurements of W(110) and Re(0001) are displayed.

carbon is completely removed. Finally, the sample is flashed to 2200 K for 5 – 6 times to desorb the remaining oxygen. A LEED pattern of a cleaned W(110) surface is displayed in figure 6.2 (a), the hexagonal LEED pattern of the hcp surface of Re(0001) is shown in figure 6.2 (b). Both patterns exhibit sharp diffraction peaks on a low background. Additionally, side-maxima between the main peaks, indicative of impurities, are missing. Both features are a sign of a clean surface geometry.

6.1.2. Xenon adlayer

A single monolayer of rare gas was used to reference the absolute timing of the photoelectrons. Neon, argon, and xenon can provide energy levels which do not overlap with the ones of the metal substrates. Xenon was used because of its high van-der-Waals

constant, which is comparable to an inter-atomic binding energy. In order to grow a layer of a rare gas on a surface, the substrate has to be cooled until it the gas de-sublimates on the crystal. Those temperatures are below 90 K for all rare gases [81]. Xenon has the highest sublimation temperature, at 73 K, which makes the cooling of the crystal much easier. Additionally, a reasonable high NIR laser intensity can be used in the streaking experiments without losing the prepared layer.

To prepare a xenon monolayer, the substrate crystal is cleaned as described in the previous section, right before the layer preparation the crystal is flashed once again to 2400 K to ensure a perfectly clean surface. The sample is cooled down with liquid helium to below 40 K. Via the gas-dosing system, a dosage of ≈ 0.24 mbar·s xenon is put on the crystal. It was shown with thermal desorption measurements that this results in approximately one monolayer. To remove the excessive adsorbed gas, the sample is heated slowly to 73 K for W(110) and to 65 – 77 K in case of Re(0001) with a rate of 1 K/s. At these temperatures, the multilayer structure desorbs and only the monolayer is left [81, 82]. For details please refer to S. Neppl's thesis.

6.2. Relative delay between conduction band and core state electrons in clean metals

Figure 6.3 shows two measured spectra of a clean W(110) surface. The red one was obtained using a monochromatic synchrotron source (measurements done by S. Neppl at Bessy, details will be given in his PhD thesis), the black one was recorded with a 4.5 eV broad XUV pulse at MPQ. Due to the different excitation and detection schemes the spectra have different shapes. The $5p$ and $4f$ core states at a binding energy of ≈ 30 eV can only be resolved using the synchrotron source, the broad XUV pulse causes the three peaks to appear as a single one. The peak ratio between the conduction band and the core states is not exactly the same in the two spectra. This is due to different acceptance angles of the two detectors used in the measurements which influence the intensity of the conduction band signal. The synchrotron spectrum shows a very weak and broad feature at around 50 eV binding energy. This can be attributed to the plasmon loss of the $4f$ states. No such feature can be found below the conduction band. The authors of [11] claimed that the plasmon loss of the conduction band spectrally overlaps with the $4f$ states and therefore influences the measured time delay. The measurements here show

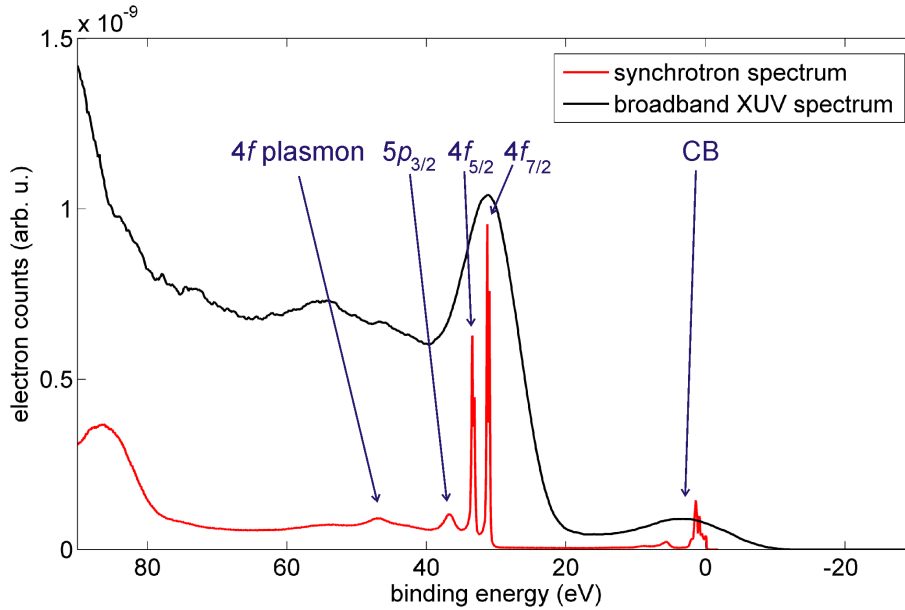


Figure 6.3.: Spectra of clean $W(110)$ measured with a broadband XUV pulse, photon energy $E_C = 130.8$ eV, bandwidth $\Delta_E = 4.5$ eV, and with a synchrotron source (BESSY), photon energy 130 eV.

that the plasmon of the conduction band is too weak to be detected. Its influence on the delay between conduction band and $4f$ is therefore neglected in the further discussion.

Both spectra show a background rising towards higher binding energies which is made of inelastically scattered electrons. The background in a streaking measurement consists of this inelastic background and of ATI electrons induced by the NIR field. Both contributions are independent of the relative delay between NIR and XUV pulses: As the component of the streaking field pointing towards the detector can be neglected inside the sample, the inelastically scattered electrons are efficiently streaked only after they are emitted from the surface. The escape time of those electrons does not have a fixed relation to the NIR field anymore, therefore a clear streaking cannot be observed, and the inelastic background is not influenced by the relative delay between NIR and XUV pulses. The contribution due to ATI electrons results from an integration of the complete NIR pulse and is therefore insensitive to the timing between NIR and XUV pulses as well. Already in the supporting online material of the first publication of A. L. Cavalieri and colleagues [7], it was shown by Fourier analysis that no component corresponding

to the frequency of the NIR field can be found in the background.

Figure 6.4 (a) shows three spectra of a streaking measurement on tungsten. Depending on the relative time delay between the two pulses, the spectra are up- or downshifted (red, green) with respect to a reference recorded outside the temporal overlap of the two pulses (blue). As expected, the background is slightly larger in the downshifted spectrum due to the larger contribution of the ATI electrons. In figure 6.4 (b), the unstreaked spectrum is displayed together with the retrieved one using the time dependent Schrödinger equation and a fit with a gaussian on a second-order polynomial background. Both analysis methods reproduce the peak position in an excellent way. The method based on peak fitting also gives the correct peak heights, the peak amplitudes returned by the Schrödinger equation are too low because the algorithm does not include any background. Both methods are not capable of reproducing the exact peak shape. A different peak fit, e.g. an asymmetric gaussian on top of a Shirley-type background [83], should be adequate to capture all details of the dataset. However, it was found empirically that the symmetric peak shapes result in a much more robust algorithm, therefore they were used to analyse the delay. In order to further improve the agreement of the spectrogram retrieval with the exact shape of the measured features, the background has to be considered explicitly and has to be subtracted from the signal before running the retrieval algorithm. However, it turned out that all analysis methods yield comparable results with respect to the relative time delay between the two photoelectron peaks, independent of the treatment of the background. This is not surprising as the delay depends on the peak positions, whereas the background influences the peak shape, which is giving information about the chirp of the emitted wave packet. An explicit dependence of the extracted delay on the extracted chirp could not be found using different analysis methods, therefore the background was not subtracted from the signal and was not taken into account explicitly.

In the following subsections, the relative delay between the emission of the two photoelectron peaks is investigated as a function of different external parameters. The delay is measured at XUV energies of $E_C = 93.5$ eV, bandwidth $\Delta_E = 6.8$ eV, $E_C = 122.3$ eV, $\Delta_E = 4$ eV and $E_C = 130.8$ eV, $\Delta_E = 4.5$ eV in tungsten and at $E_C = 93.5$ eV, $\Delta_E = 6.8$ and $E_C = 129.5$ eV, $\Delta_E = 5.6$ eV in rhenium. The intensity of the streaking field is varied between $\approx 50 \cdot 10^9$ and $\approx 600 \cdot 10^9$ W/cm². Finally, a short summary of measurements at different sample temperatures is given. The results indicate that a model including exclusively either an initial state or a final state effect

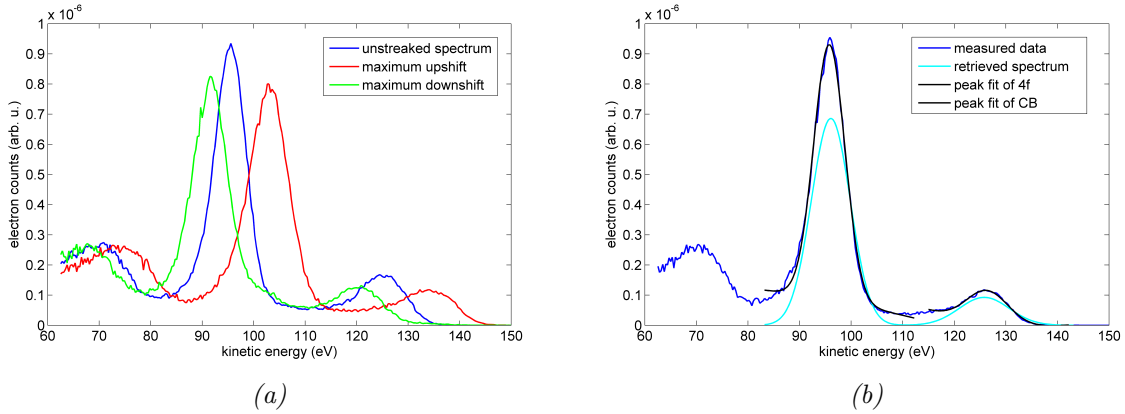


Figure 6.4.: Measured spectra of W(110) at different relative delays between XUV and NIR pulses (a). Measured, retrieved and fitted spectrum of W(110) at a relative delay of 6 fs between XUV and NIR pulses (b). XUV energy: $E_C = 130.8$ eV, bandwidth $\Delta_E = 4.5$ eV.

cannot describe the observed dynamics. The delay was found to be independent of the applied streaking field strength as well as of the crystal temperature.

Compared to previously published results [7], the experimental geometry is slightly changed. The XUV and NIR pulses are incident on the sample near Brewster's angle, the electron detector points along the surface normal. The axis of polarisation does not lie in the plane of incidence as it was the case in the published setup but is tilted by 20 degrees resulting in a small field component of 6% along the crystal surface. This is a consequence of the geometry of the new experimental chamber.

6.2.1. Measurements of the influence of the XUV photon energy

Figure 6.5 shows three measured and retrieved spectrograms of a tungsten (110) surface recorded at XUV photon energies of $E_C = 93.5$ eV, $\Delta_E = 6.8$ eV (a), $E_C = 122.3$ eV, $\Delta_E = 4$ eV (b), and $E_C = 130.8$ eV, $\Delta_E = 4.5$ eV (c) respectively, the reflectivity curves of the used XUV mirrors are given in the appendix. The presented data at $E_C = 130.8$ eV were obtained by E. Bothschafter and S. Neopl. The delay axis of each spectrogram indicates the relative timing between NIR and XUV pulse, negative values meaning the NIR pulse hits the sample first.

The displayed data are the raw measured ones converted to the energy domain, refer to the appendix for details, no smoothing and no background subtraction was done. Compared to previously published data [7], the photoelectron peak amplitude compared to the background level was significantly enhanced. This is a consequence of the higher repetition rate of the laser, the improved vacuum environment, and the transmission function of the time-of-flight detector. Especially the ultrahigh vacuum conditions in the experimental chamber reduce the background of the photoelectron signal. Test measurements in the non-baked system (pressure $\approx 10^{-9}$ mbar) show comparable quality to the data in the old setup, the background between the conduction band and the $4f$ peak rises and forms a broad shoulder at the low-energy side of the conduction band peak. The lower background pressure manifests itself also in a smaller amount of space charge. Within this work, the term space charge refers to low energy electrons excited by the NIR pulse. Residual gases like carbon or carbonmonoxide, which adsorb on the surface, might locally change the work function and therefore increase the number of space charge electrons. This cloud of slow electrons manifests itself in an upshift of the photoelectron spectrum if the NIR field is turned on. Under typical experimental conditions, this shift was 3 eV in the old setup, the maximum upshift observed with the new apparatus is less than 2 eV. Additionally, the change of this shift during one measurement was found to be on average only 0.05 eV.

The integration time of each time step in the spectrograms in figure 6.5 was 20 s (a), 30 s (b), and 35 s (c), the delay between the NIR and the XUV pulses was varied in steps of 300 as (a), 200 as (b), and 150 as (c). Each spectrogram was recorded in one sweep starting from negative delays. The data analysis revealed no systematic drifts induced by this method owing to the high stability and the excellent vacuum conditions of the setup. The electrostatic lens was used in all measurements, the applied voltage was adjusted to shift the enhancing part of the transmission function to the region of the two photoelectron peaks. All displayed spectrograms were recorded at room temperature.

Examination of the different spectrograms shows that the relative peak height of the conduction band decreases with increasing photon energy. This is in agreement with tabulated cross sections [84] and synchrotron measurements. In the spectrogram recorded at 93.5 eV, the width of the peaks is larger than in the other two data sets because the bandwidth of the XUV mirror was 6.8 eV in this case instead of 4 and 4.5 eV in the other ones. The measured and retrieved spectrograms show a chirp with an absolute value on the order of $\approx 10 \text{ fs}^{-2}$ in the XUV pulse, a positive one at 93.5 eV (a) and a

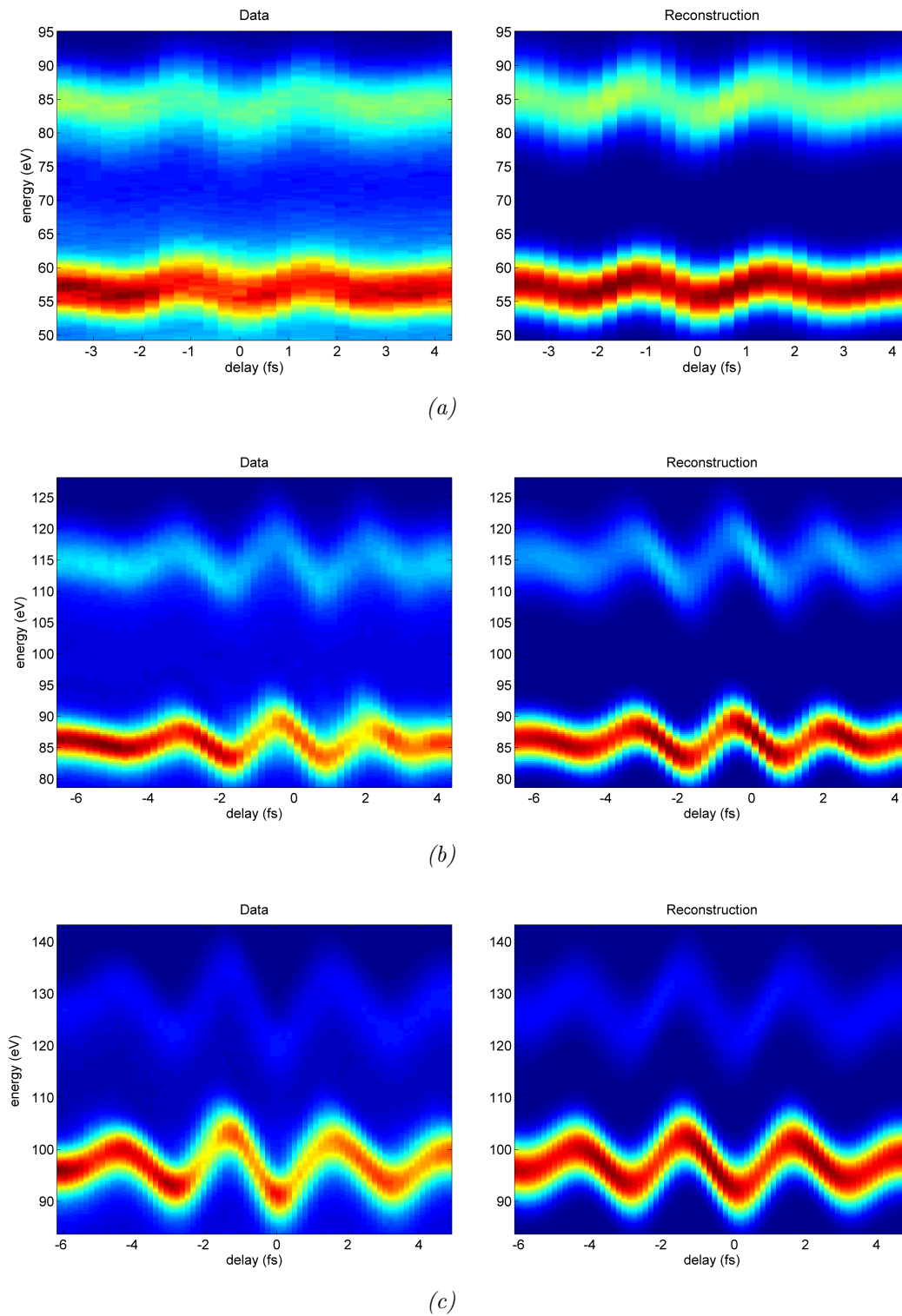


Figure 6.5.: Retrieved and measured spectrograms of $W(110)$.

XUV energy: $E_C = 93.5$ eV, $\Delta_E = 6.8$ eV (a), $E_C = 122.3$ eV, $\Delta_E = 4$ eV (b), and $E_C = 130.8$ eV, $\Delta_E = 4.5$ eV (c).

negative one at 122.3 eV and 130.8 eV (b, c). This chirp can be seen in the asymmetry of the streaking traces of both conduction band and $4f$ states. So far, it is not clear why the chirp changes sign. To rule out possible explanations like the HHG mechanism, influence of the phase of the XUV mirror, or the photoemission process itself, the exact peak shape has to be evaluated, and reference measurements in the gas phase have to be done. This is subject of future investigations. The amplitude of the modulation of the peaks increases with increasing XUV photon energy. This modulation is directly proportional both to the XUV photon energy and to the applied NIR electrical field (equation 2.16), where the latter one can be larger for higher photon energies without obscuring the $4f$ peak with ATI electrons. The modulation depth can be directly seen in the peak fits given in figure 6.6. Here, each peak was fitted with a gaussian function on top of a second-order polynomial background.

In figure 6.6, it is visible that the two photoelectron traces are delayed with respect to each other. The conduction band electrons escape earlier than the core state electrons, their relative time delay gets smaller with increasing XUV energy. Figure 6.7 summarises the measurements on tungsten at different photon energies. The plotted delays are averages over several measurements, which were analysed with the retrieval algorithm. The error bars describe the statistical errors assigned to the fitting algorithm. The delay decreases from 78 ± 10 as at 93.5 eV to 44 ± 3 as at 120 eV and 22 ± 11 as at 130 eV. The delay at 93.5 eV agrees with the first result measured on tungsten, where the delay was measured to be 110 ± 70 as at an XUV photon energy of 90 eV. Compared to this result, the errorbar could be significantly reduced due to the improved experimental conditions. In figure 6.7, the expected time delay assuming a classical, free-electron like transport in the metal is plotted as well as a function of XUV energy, details on how the classical delay is calculated are given below. Although this calculated delay shows a decreasing behaviour as well, the measured delays are much larger and show a stronger decrease with photon energy than the calculated ones. The error bars of the different measurements do not overlap with each other and also do not include the classical result.

As a comparison, results obtained on Re(0001) are displayed in the graph as well. The corresponding data are depicted in figure 6.8, the integration time was set to 20 s (a) and 30 s (b), the delay was varied in steps of 300 as and 100 as at XUV energies of $E_C = 93.5$ eV, $\Delta_E = 6.8$ eV and $E_C = 129.5$ eV, $\Delta_E = 5.6$ eV respectively. In case of the 129.5 eV pulse the sample temperature was set to 40 K. These spectrograms show similar behaviour to the ones on tungsten. The conduction band peak drops as well

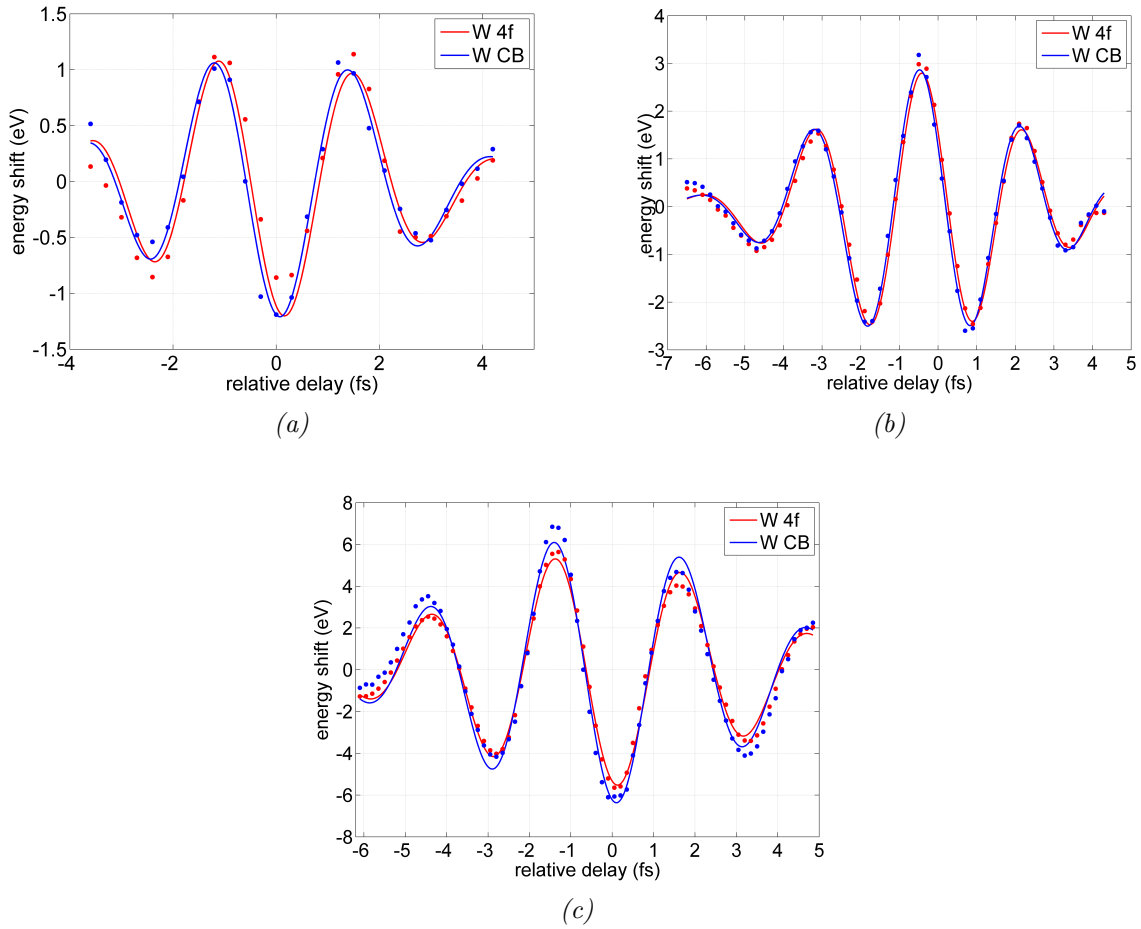


Figure 6.6.: Peak fits of the CB and 4f states of W(110).

XUV energy: $E_C = 93.5 \text{ eV}$, $\Delta_E = 6.8 \text{ eV}$ (a), $E_C = 122.3 \text{ eV}$, $\Delta_E = 4 \text{ eV}$ (b), and $E_C = 130.8 \text{ eV}$, $\Delta_E = 4.5 \text{ eV}$ (c).

with increasing photon energy, and the modulation depth of the peaks increases as a consequence of the larger applied NIR field strength and the increased XUV photon energy. Interestingly, the XUV chirp at 130 eV has a positive sign, in contrast to tungsten where it is negative. However, a direct comparison between all parameters of the two datasets is not valid because two different XUV mirrors with different bandwidths were used in the experiment. A systematic investigation of this effect has to include measurements in the gas phase which serve to characterise the XUV and NIR pulses.

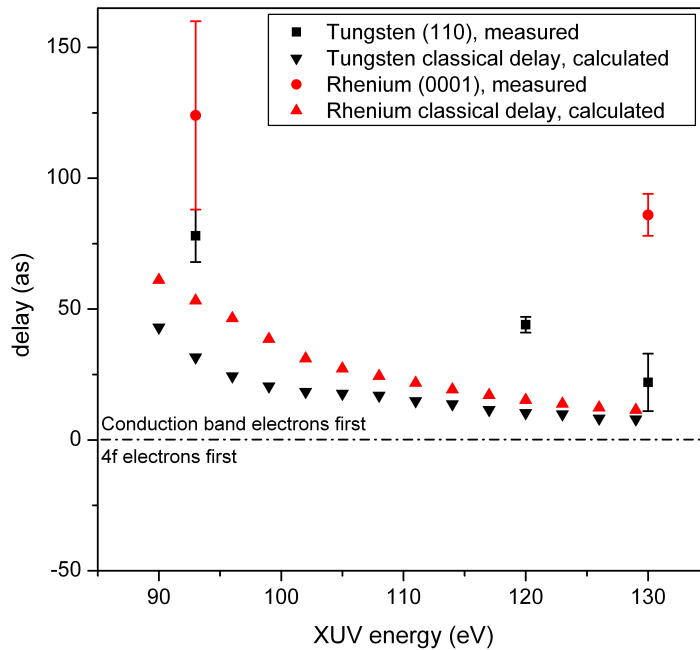


Figure 6.7.: Relative time delay between CB and 4f states measured on a W(110) (black) and a Re(0001) (red) surface as a function of XUV energy.

The datasets on rhenium were analysed with the peak fit. The measured delay at $E_C = 93.5$ eV, $\Delta_E = 6.8$ eV is 124 ± 36 as, and 86 ± 8 as at $E_C = 129.5$ eV, $\Delta_E = 5.6$ eV. Only two datasets could be used to evaluate the delay at 93.5, a single one at 129.5 eV. Compared to the data obtained on tungsten, the noise level was slightly higher in this particular measurement run, explaining the large error bar at 93.5 eV. The delay shows a decreasing trend as well although the error bars still overlap. Again, the calculated time delays assuming classical transport lie well below the measured values and outside the error bars. Here, the calculated delay decreases much stronger than the measured one. The most striking feature is the huge difference in the delay between tungsten and rhenium at 130 eV. The classical approach fails to explain these values. Models including only the mean escape depth of the electrons and the nature of the initial states should be able to reproduce the trend of a decreasing delay as it results from the decrease in the IMFP of the localised 4f electrons. However, the IMFP differs only by 0.5 \AA for tungsten and rhenium at 130 eV, and it is smaller for rhenium. An

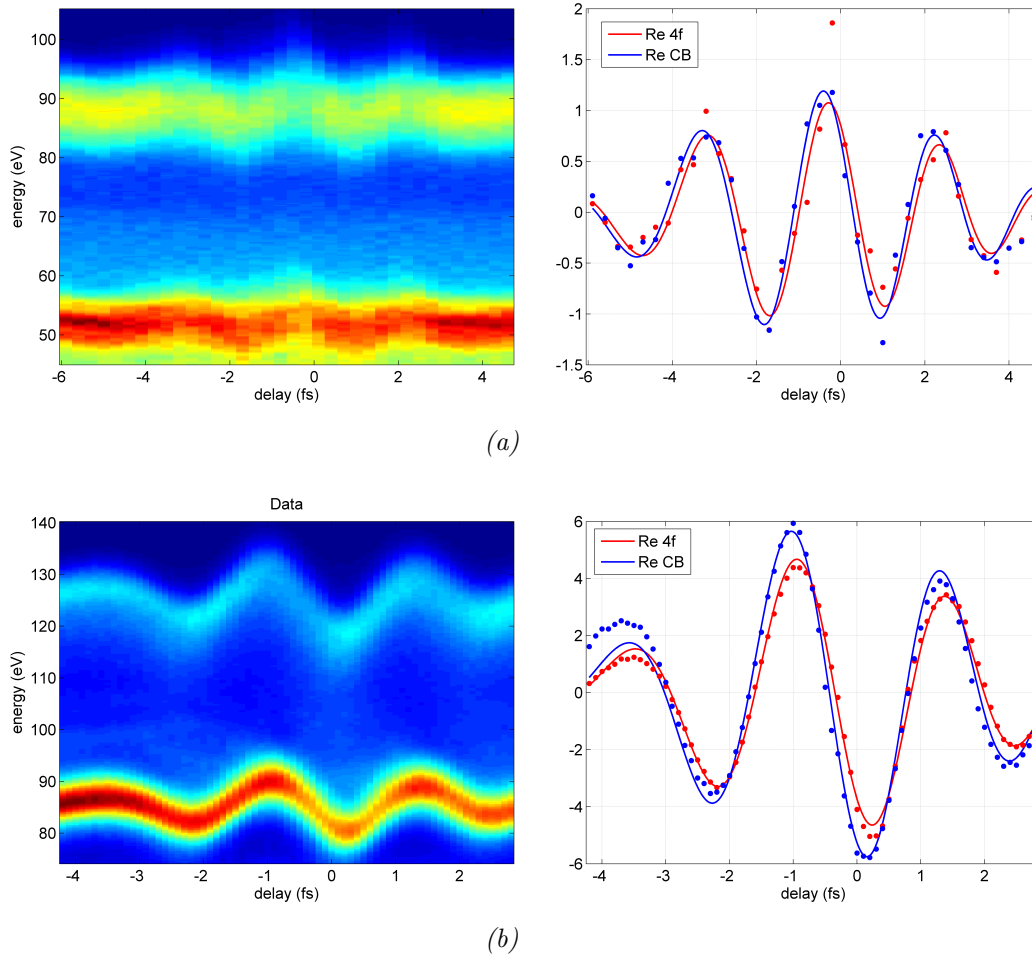


Figure 6.8.: Measured and fitted spectrograms (gaussian peak fit) of Re(0001) at a XUV photon energies of $E_C = 93.5 \text{ eV}$, $\Delta_E = 6.8 \text{ eV}$ (a) and $E_C = 129.5 \text{ eV}$, $\Delta_E = 5.8 \text{ eV}$ (b).

effect of the final state and of the exact electronic properties of the system on the dynamics of the photoemission process seems therefore highly probable.

6.2.2. Simulation of the influence of the XUV photon energy with density functional theory

So far, several theoretical concepts explaining the origin of the measured delay rely

on the different spatial extension of the initial state wavefunctions [10, 9]. In these published calculations, the delay occurs as a consequence of the localisation of the $4f$ electrons and the complete delocalisation of the conduction band electrons. A final state in a high-lying conduction band of the crystal is not included in these models. In order to quantify the possible influence of the crystal lattice on the timing between the two photoelectron peaks, the band structure of both systems was calculated with DFT, and the group velocity of the final states was estimated based on these results. In contrast to the initial calculations done in [7], where only the direction along the surface normal was considered, the complete first Brillouin zone is sampled in the present work. Deviations from the numbers published in [7] result both of the different sampling area and different approximations made in the DFT calculations. Additionally, the maximum group velocity of each energy region was used to calculate the time delay in the publication, whereas here it is the mean group velocity.

The band structure of tungsten was computed using the WIEN2k package [71]. The system was simulated with the experimentally determined lattice constants, see chapter 6.1 for details. An LAPW-basis set with local orbitals was used, electron exchange and correlation were treated within the generalised gradient approximation [74]. All electrons with a binding energy of more than 95 eV were considered to be completely confined to the core. This way, the $4f$ electrons are fully implemented in the calculation. The next neighbour distance in tungsten is 2.74 Å, the muffin-tin radius was set to 1.32 Å to minimise the interstitial region where only plane waves are used. The irreducible wedge of the first Brillouin zone was sampled with 816 \vec{k} -points. This number is usually considered to be very high. However, as we are interested not only in the energy eigenvalues but especially in the curvature of the potential surface a much denser mesh than in other calculations is required, where usually a number of ≤ 500 is used [72]. The energy and charge convergence criteria in the SCF cycle were set to 0.01 eV and 0.01 e . The calculated band structure agrees well with data published by N. E. Christensen [85].

In a first step, the complete irreducible wedge was sampled to find possible vertical transitions. All vertical transitions within the bandwidth of the XUV pulse between occupied states below the Fermi-energy and unoccupied states above the vacuum level were considered, no selection rules or transition probabilities were applied in this method. In a second step, the \vec{k} -vectors lying within the detection cone of the TOF detector, defined by its acceptance angle ϑ_{det} , were selected:

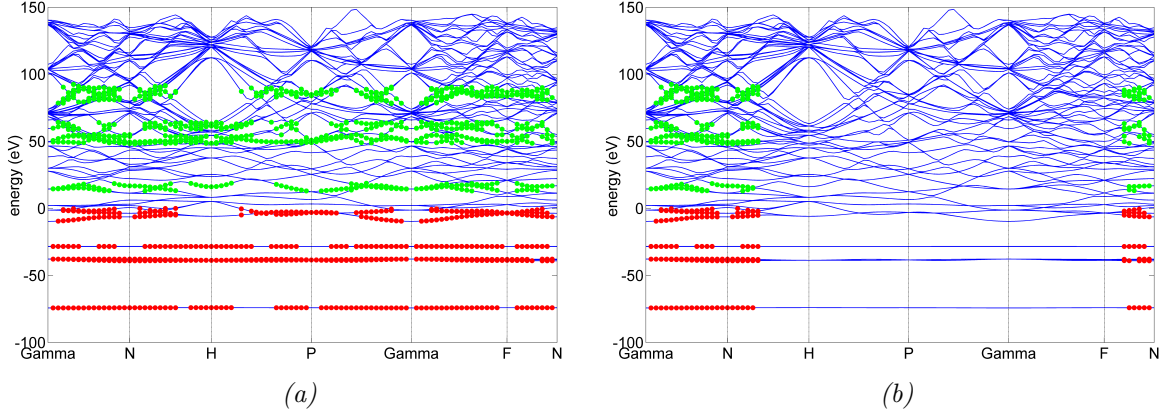


Figure 6.9.: Possible transitions in tungsten using a 90 eV XUV pulse with 6 eV bandwidth (a) and detected \vec{k} -vectors assuming an acceptance angle of 22° (b).

$$\sin \vartheta_s(\vec{k}) \cdot \sqrt{\frac{E(\vec{k})}{E(\vec{k}) - W}} < \sin \vartheta_{det} \quad (6.1)$$

Figure 6.9 shows the computed band structure along high symmetry directions in the irreducible wedge with all possible vertical transitions assuming a 90 eV pulse with a bandwidth of 6 eV. The initial states are indicated with red dots, the final states with green ones. The orientation of the (110) surface normal corresponds to the direction Gamma-N in reciprocal space. Photoelectrons are excited within almost the complete first Brillouin zone. No final states for the conduction band electrons can be found around H due to a large gap in the high-lying band structure. Photoemission from a crystal with a (100) surface can therefore be used to test the result of the DFT calculation in an easy way. The distribution of the detected \vec{k} -vectors in the first Brillouin zone is visualised as well. An acceptance angle of $\pm 22^\circ$ was assumed in this calculation, corresponding to the maximum acceptance angle of the detector when the electrostatic lens is in use. The distribution shows a narrow cone along Γ -N, indicating that mostly electrons with a large crystal momentum along the surface normal can be detected.

The resulting \vec{k} -vectors and their corresponding energy eigenvalues and group velocities were divided into two groups depending on their initial state being in a 4*f* state or the conduction band. The energy eigenvalues and the group velocities of each group were

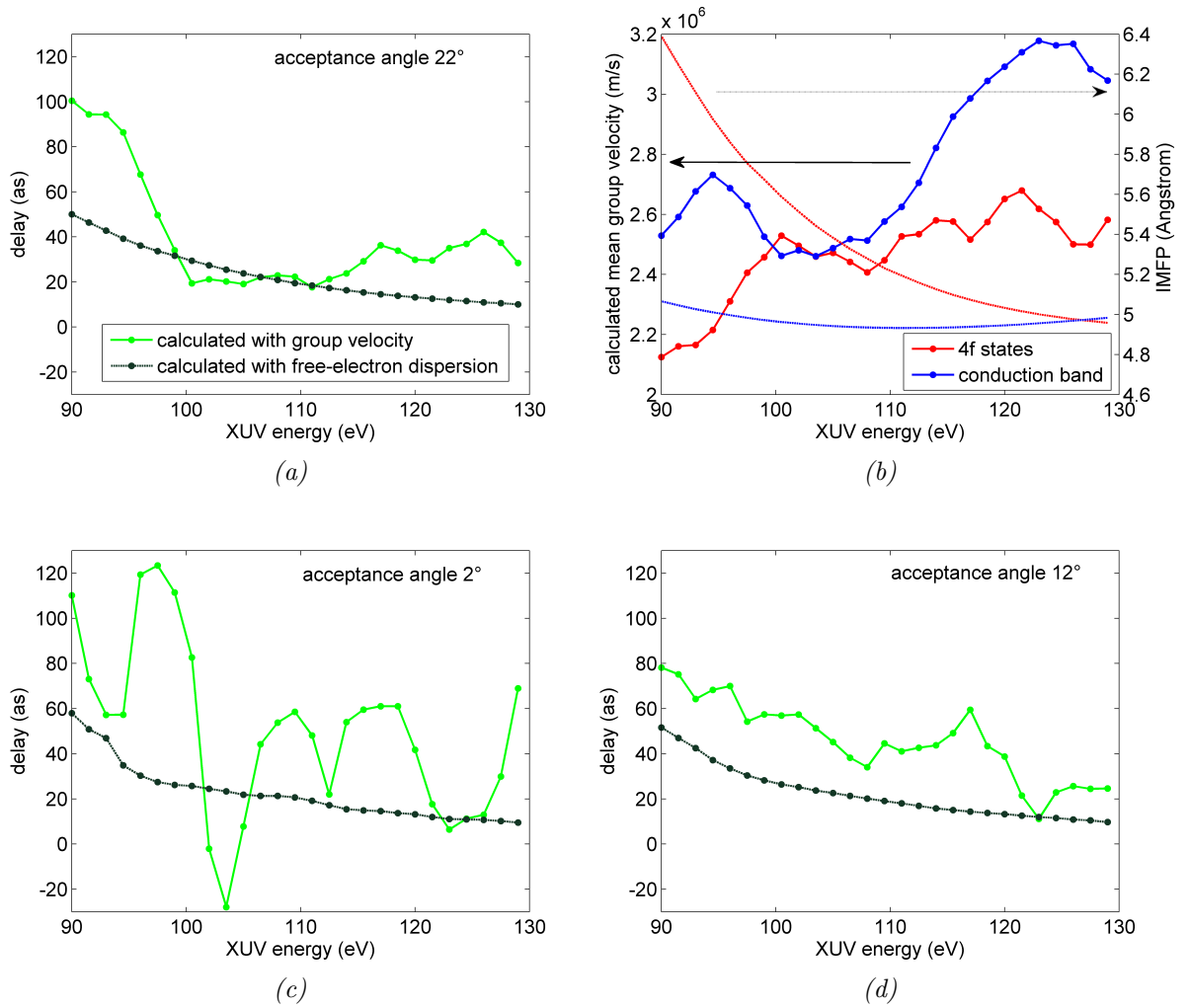


Figure 6.10.: Calculated time delay between $W(110)$ CB and 4f states as a function of XUV energy and of the acceptance angle of the detector (a, c, d) and calculated mean group velocities and inelastic mean free paths of CB and 4f states as a function of XUV energy at an acceptance angle of 22° (b).

averaged according to their weights in the first Brillouin zone. The average energy was used to calculate the inelastic mean free path of the electrons in the crystal via the TPP-2 formula [22, 23]. Within this formula, tabulated values of the atomic mass, the mass density and the number of valence electrons were used [76]. Instead of the tabulated values numbers from expanding the dielectric function can be used in the

TPP-2 expression as well. This results in a slight shift of $0.5 - 1 \text{ \AA}$ of the IMFP, but in no significant difference in the obtained time delays. The time delay between $4f$ and conduction band electrons was calculated as run-time difference, using the average group velocity, v_g , to get the time delay δt_{BS} depending on the crystal band structure, and using the free-electron like velocity to get the classical time delay, δt_{class} .

$$\begin{aligned}\delta t_{BS} &= \frac{\lambda(E_1)}{v_{g1}} - \frac{\lambda(E_2)}{v_{g2}} \\ \delta t_{class} &= \sqrt{\frac{m}{2}} \left(\frac{\lambda(E_1)}{\sqrt{E_1}} - \frac{\lambda(E_2)}{\sqrt{E_2}} \right),\end{aligned}\quad (6.2)$$

where the indices 1, 2 refer to the $4f$ states and the conduction band, respectively, and the quantities E_1 , E_2 and v_{g1} , v_{g2} are calculated as mean final state energies and group velocities inside the crystal. The group velocity is calculated via

$$\vec{v}_{group}(\vec{k}) = \frac{e}{\hbar} \vec{\nabla}_k \cdot E(\vec{k}), \quad (6.3)$$

averaging is done not only within the energy interval of interest but also over the whole first Brillouin zone. The results using a 6 eV broad XUV pulse and an acceptance angle of 22° are displayed in figure 6.10 (a). The calculations reproduce the overall trend of decreasing delay at high XUV energies and also show a significant drop of the delay as seen in the measurements. The dispersion of the crystal potential surface in the area surrounding the surface normal is substantial. The lower panel in figure 6.10 shows the same calculation with different acceptance angles of 2° and 12° . Comparing the two observable acceptance angles, 2° and 12° , which correspond to zero lens voltage and a value of $\approx 600 \text{ V}$, one sees that the delay gets significantly altered at all energies. Measurements done at 93.5 eV photon energy where spectrograms were recorded with and without the electrostatic lens of the TOF detector did not give a significant result due to the high noise in the datasets without lens, a downshift of the delay to 60 as without lens can be expected from the DFT calculations. At 130 eV, the delay is expected to increase to 70 as. However, measurements at high photon energies without lens are not feasible. Due to the extremely low countrate in the conduction band an integration time which is at least 20 times larger than with lens would be necessary, resulting in a total acquisition time of 10 hours for one spectrogram. An easier way to probe the high dispersion is to investigate a different crystal orientation. A tungsten (100) surface could be used to test both the calculated bandgap and the angular dependence of the delay.

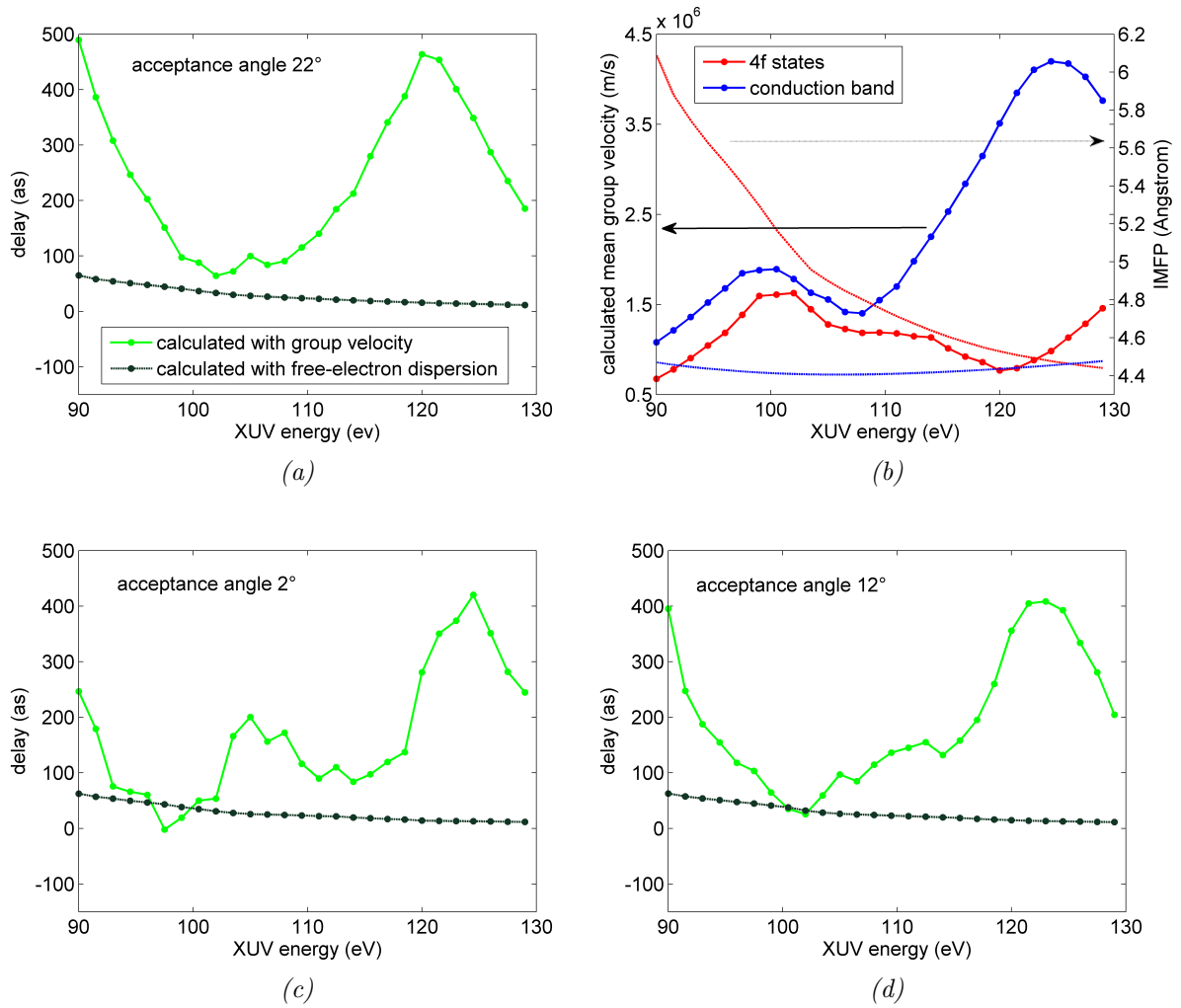


Figure 6.11.: Calculated time delay between $Re(0001)$ CB and 4f states as a function of XUV energy and of the acceptance angle of the detector (a, c, d) and calculated mean group velocities and inelastic mean free paths of CB and 4f states as a function of XUV energy at an acceptance angle of 22° (b).

The measurements above 100 eV were done with a different bandwidth of the XUV pulse. This alters both initial and final state of the photoemission process and could particularly influence the behaviour of the conduction band electrons. The calculations were therefore repeated with a 4 eV broad pulse. No significant change in the results could be seen.

The same algorithm was applied to rhenium. Again, a LAPW-basis with local orbitals was used, the energy cut for core electrons and the muffin-tin radius were set to the same value as in tungsten. The irreducible wedge was sampled with 1450 \vec{k} -points. The mesh was set denser because a more complicated band structure is expected due to the additional valence electron and the high spin-orbit coupling in rhenium. The results of the calculations are given in figure 6.11. In contrast to tungsten, the DFT simulations fail to explain the observed delay in rhenium. Although the trend of decreasing delay is visible also in the computed results at 93 and 130 eV, the expected delays are much higher than the measured ones. It is not clear what causes this large discrepancy. One possible source is the DFT calculation itself: The positions of unoccupied states are known to be only approximate if they are calculated with DFT. One way to verify the calculated band structure is to compare the eigenvalues with inverse photoemission experiments. Unfortunately, no inverse photoemission has been reported on rhenium so far.

In summary, the XUV dependence of the measured delay shows that an influence of the final states on the measured delay should be taken into account. Results from DFT calculations confirm a strong, non-trivial dependence of the group velocity on the exciting XUV photon energy. However, the calculated values, which are presented here, might have to be shifted along the energy axis due to the inaccuracy of DFT calculations of unoccupied states. Measurements on different surface planes, angularly resolved measurements, and experiments with different acceptance angles of the detector should be carried out to get further understanding of the factor the band structure plays in photoemission. The significant different delays measured in tungsten and rhenium at the same excitation energies strengthen the argument that sample properties have to be taken into account explicitly in theory models.

6.2.3. Measurements of the influence of the probing NIR intensity

One crucial point in interpreting streaking data of solid state systems is the influence of the NIR pulse inside the sample. The penetration depth of the electrical field in tungsten is on the order of 100 Å [11], the laser is not significantly attenuated on a length scale of the sampling depth of the current streaking experiments. It can therefore alter the electronic properties of the conduction band electrons prior to their photoionisation and can affect the transport of conduction band and $4f$ electrons to the crystal surface.

The measured time delay between two photoelectrons is derived from the modulation of

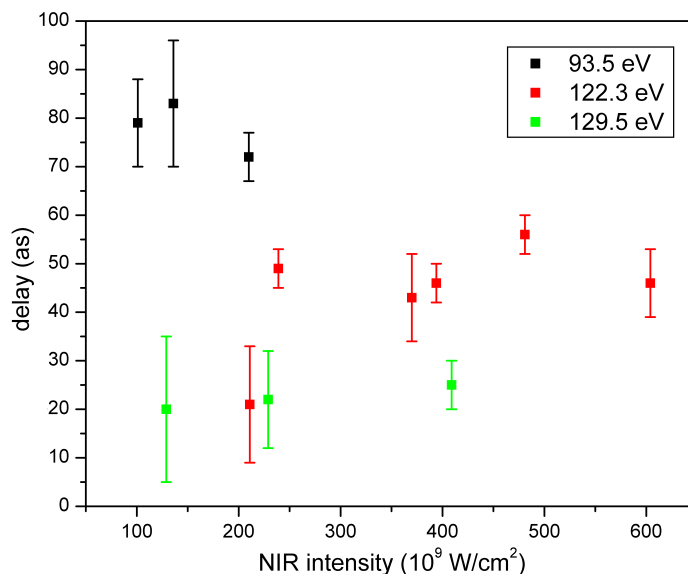


Figure 6.12.: Measured time delay between of $W(110)$ $4f$ electrons with respect to CB electrons as a function of NIR intensity at different XUV energies.

their kinetic energy due to the laser field. This depends only on the normal component of the electrical field. In the stationary limit of the Fresnel equations, the streaking field gets refracted at the crystal surface and is bent towards the surface normal. A light field incident on the sample under Brewster's angle (75.6° for tungsten, 73.1° for rhenium, [47]) will be refracted to an angle of 14° in tungsten and 16° in rhenium. This reduces the component of the streaking field along the surface normal to 6% of the field strength in vacuum in tungsten and to 8% in rhenium. Although these values allow to neglect the influence of the NIR pulse inside the sample, the Fresnel equations are not valid in the first layer of a metal [86, 87]. There, the electrical field exhibits a longitudinal component as well, which can induce changes in the probed electronic system. In theoretical calculations, the amount of the longitudinal component varies depending on how the surface barrier is modeled [86, 87]. Measurements which could help to estimate the order of magnitude of the effect are so far not known. Furthermore, it is not clear if any of these models is valid on an attosecond timescale because they rely on steady-state descriptions of the dielectric response of the system. Observed properties like chirp, duration, central frequency and escape time of the electron wave packet might therefore be correlated to the applied NIR field strength.

In order to estimate the effect of the streaking field on the measured delay, the obtained time delays between conduction band and $4f$ electrons in tungsten are displayed in figure 6.12 as a function of NIR intensity. The presented data at $E_C = 130.8$ eV were obtained by E. Bothschafter and S. Neppl. The intensity of the NIR pulse was calculated with the results of the spectrogram algorithm, where the vector potential was assumed to have a gaussian envelope with a cosine-like modulated carrier (see chapter 6.1 for details). Although it was found empirically that the retrieval gives systematically too high intensities by $\approx 20\%$ for synthetically generated data, other parameters, especially the delay, are not affected by this. The absolute numbers of the NIR intensity therefore might have to be shifted to lower values. The peak fit was not used here because the two traces are fitted with two independent field amplitudes, resulting in an unsystematic scattering of the NIR intensity. Nevertheless, the overall trend could also be reproduced with the peak fits.

The datasets used to calculate the points in figure 6.12 were obtained on different days. Any systematic drifts which could affect the result if the measurements were done directly one after the other can therefore be fully excluded. Only the measurements on tungsten were considered for this parameter scan. The datapoints form three bunches at different delays, depending on the exciting XUV energy. A very weak trend of a decrease of the delay at 130 eV can be seen, but the error bars still allow for a constant behaviour. At 93.5 eV and 122.3 eV no significant effect of the NIR intensity on the measured delay can be identified at all. The reason for the significant outlier at 122.3 eV with a delay of only 21 as is not known. In summary, it is clear that the NIR intensity does not have a strong influence on the measured delay within an interval of $100 - 600 \cdot 10^9 \text{ W/cm}^2$. This interval can be extended to $\approx 50 \cdot 10^9 \text{ W/cm}^2$ if the peak fit is employed to evaluate datasets with a very low streaking amplitude.

This confirms that it is a good approximation to neglect the streaking effect of the NIR field inside the metal, the measured delay originates from properties of the examined crystal and does not carry information about the probing field. The attosecond transient recorder can be applied to metallic single crystals to perform time-resolved measurements on the attosecond scale without perturbing the probed system. The result could further indicate that the Fresnel equations are already a good approximation in the first layers extending 5 \AA inside the crystal and that the longitudinal component of the electrical field plays only a minor role compared to the transverse one.

6.2.4. Measurements of the influence of the sample temperature

Our model predicting the relative time delay between two photoelectrons relies on transport of the photoexcited electron in the crystal. The semi-classical escape depth, which is assigned to an electron within this model is limited by inelastic scattering in the sample. As already pointed out, its main component is scattering with valence electrons near the Fermi edge. Phonon scattering is less dominant at high excitation energies [17], also interactions with the lattice are expected to be too slow to have an influence on an attosecond experiment. The electron-electron scattering could be influenced by the sample temperature. Above 0 K the Fermi-Dirac distribution gets softened at the Fermi energy in a region of $\approx 1 \cdot k_B T$. Although the occupation probability at an energy of 0.5 eV above the Fermi edge is only on the order of a few percent if the sample temperature rises to 1000 K, it is not directly clear which influence this can have on the measured delay. In order to specify the effect of an increase of the sample temperature, its value was set to 700 K at an excitation energy of 93.5 eV and to 40 and 700 K at 122.3 eV in several streaking measurements. No effect on the delay could be found within the error bars of the measurements. This confirms that phonon scattering does not play a role on the observed time scales and that the softening of the Fermi edge does not alter the scattering rate of the electrons.

6.3. Absolute delay between core state electrons in rhenium covered with a monolayer of xenon

First experiments to reference the absolute escape time of photoelectrons by growing a monolayer of a rare gas on top of a single crystal were done on a combined system of a rhenium (0001) surface with a monolayer of xenon. Xenon has two high-lying energy levels, $5p$ and $5s$, at binding energies of 13 and 23 eV, and a deeper lying core state, $4d$ at 69.5 eV. A spectrum recorded at an XUV photon energy of 129.5 eV with a coincident NIR pulse at 6 fs delay is displayed in figure 6.13. Three peaks can be resolved: A broad feature consisting of the rhenium conduction band and the Xe $5p$, and the two deeply bound core states of Re and Xe. The $5s$ level of xenon is not visible because of its small cross section [84] and because satellite peaks of the conduction band caused by the XUV mirror mask the weak signal (see appendix B for a reflectivity curve). These satellites also explain the broad shoulder towards low energies of the conduction band. The Re

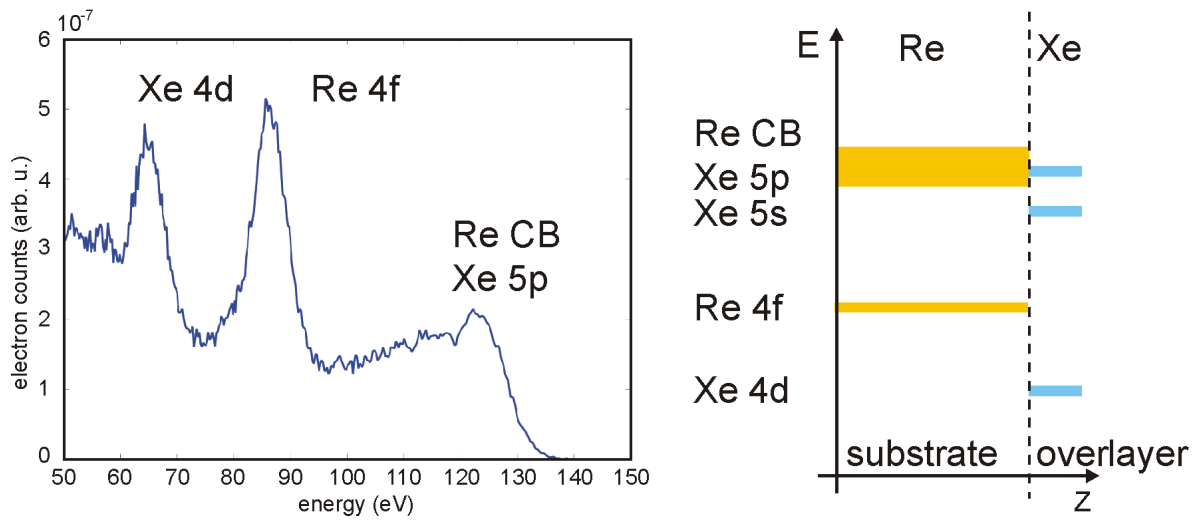


Figure 6.13.: Spectrum and energy scheme of a single monolayer of xenon on a rhenium substrate. The spectrum was recorded at a photon energy of $E_C = 129.5$ eV, $\Delta_E = 5.6$ eV.

$4f$ and Xe $4d$ states can be clearly resolved, at the Xe $4d$ peak already the exponential shape of the ATI background is visible. As the relative delay in the clean metals was insensitive to the background subtraction, it was omitted here as well.

6.3.1. Simulation of the combined system with density functional theory

The concept of referencing the timing of the substrate electrons with an adlayer relies on the weak interaction between the rare gas atoms and the rhenium atoms. Although xenon interacts with other atoms only via the van-der-Waals force, the exact mechanisms of physisorption on a metal site were under debate for a long time: Due to the large polarisability and the large van-der-Waals constants of xenon it was not clear whether any charge transfer is taking place in the adsorption process [88, 89]. A strong electronic coupling would severely influence both adlayer and substrate, a comparison of the delay between Xe and Re electrons to the one measured in a clean substrate would get more complicated. In order to justify the approach of an isolated adlayer, DFT calculations on the combined system were carried out.

The geometry of a single xenon layer on a rhenium (0001) surface is not known exactly. Measurements and simulations on other hcp surfaces indicate that xenon adsorbs in a $\sqrt{3} \times \sqrt{3} R(30)$ geometry on top sites of the substrate [90]. This geometry was simulated, the spacing between the Xe atoms and the Re substrate was set to 3 Å (estimation via hard spheres), this geometry was not allowed to relax during the DFT algorithm. The complete system was simulated as a quasi-2D slab of 13 Re atoms with one Xe atom on top and 15 Å of vacuum between subsequent slabs. For the Re substrate the bulk geometry was assumed.

LAPW with local orbitals were used as basis set, the cut between fully treated valence states and confined cores states was set to 95 eV, the muffin-tin radius was set to 2.5 Å. The irreducible wedge of the first Brillouin zone was sampled with 21 \vec{k} -points. The unit cell of the combined system is extended over more than 40 Å in z-direction, resulting in an extremely flat Brillouin zone which can be sampled with one \vec{k} -value ($= 0$) in that direction. This significantly reduces the required size of the \vec{k} -mesh.

The WIEN-package does not include a specific van-der-Waals interaction, the bonds of xenon are known to be over- (LDA) or underestimated (GGA) by $\approx 3 - 15\%$ [91]. Test simulations of bulk xenon and of xenon monolayers in different geometries confirmed this assumption and reproduced published results [91]. As the calculations of the combined system are not used to derive any energy levels or band structure effects, but should only qualitatively test the interaction between the adlayer and the substrate, the GGA was chosen to find a lower bound of possible interactions.

In order to be able to identify the influence of the Xe-Re interaction, the two systems were simulated individually as quasi-2D slabs as well. The parameters of the SCF cycle were identical to the ones of the combined system. The left panel of figure 6.14 shows the calculated valence density of the Xe monolayer (top) and the first five layers of the Re substrate (bottom) in an energy interval of $-11 - 0$ eV with respect to the Fermi level, the spatial resolution was set to 0.2 Å. The electron distribution of adjacent Re atoms overlaps, indicative of non-directional bonding in metals. The break of symmetry due to the surface has an effect only on the first and second layer. The electrons of the topmost layer are pushed to the side because the bond along the surface normal has to be redistributed. The second layer is almost unperturbed, the electron density of the third layer already displays the same symmetry as the bulk. No deviation from radial symmetry can be seen in case of the xenon monolayer. Any lateral interaction is not visible in these plots. The DOS, plotted in figure 6.15 (a), however, indicates that

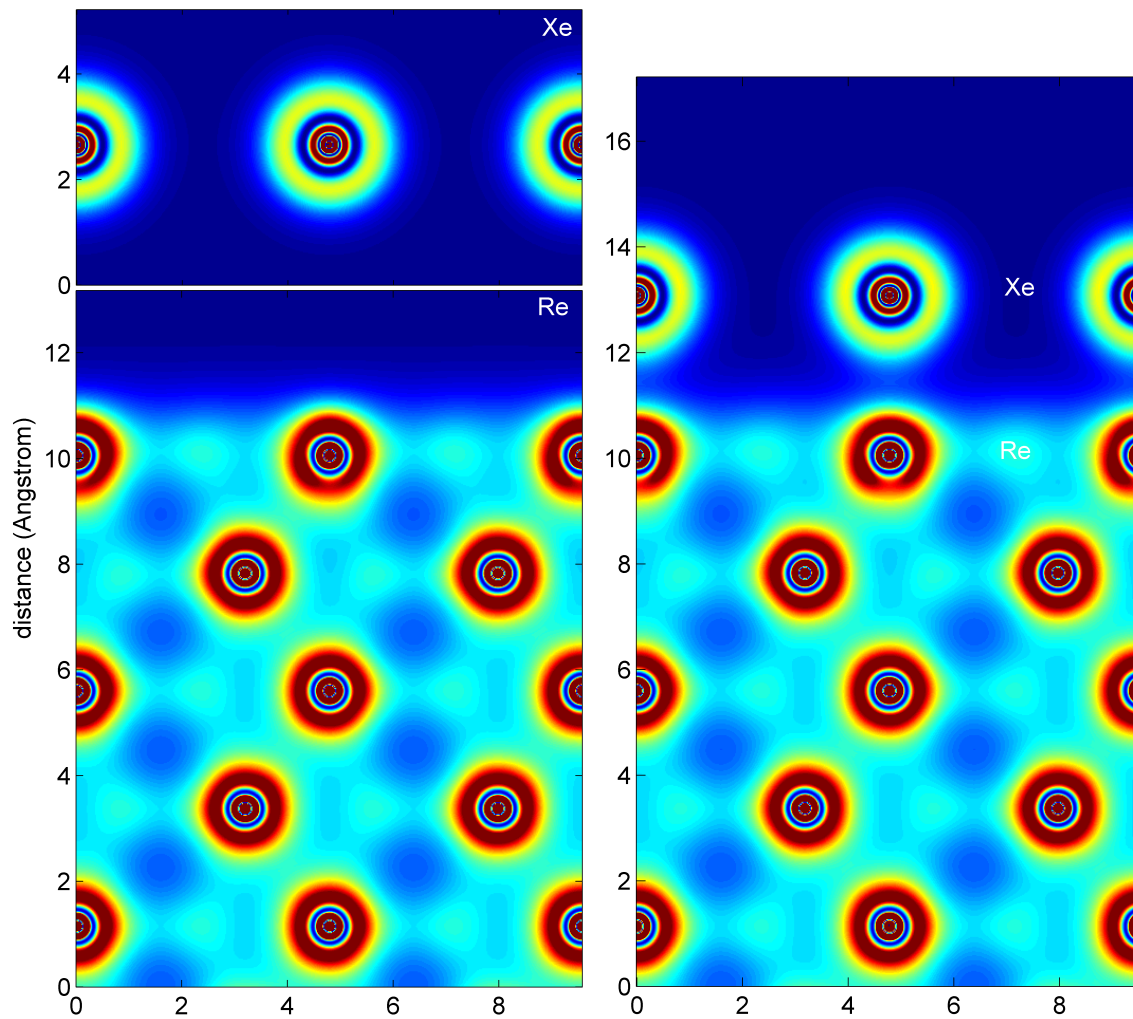


Figure 6.14.: Calculated valence electron density of an isolated xenon monolayer and a rhenium slab (left) and of the combined system (right).

a lateral interaction is present. The xenon $5p$ -states are broadened to almost 0.5 eV . Broadening of these states was also found in closer packed monolayers [91] while the s -states are not influenced. The DOS of the rhenium slab reproduces the 3D result very well. Deviations can be attributed to the behaviour of the topmost atoms.

The valence electron density of the combined system shows the expected behaviour: A weak dipole is formed between the top rhenium layer and the xenon atoms, the rhenium conduction band electrons are pushed even more outside the slab, the radial symmetry

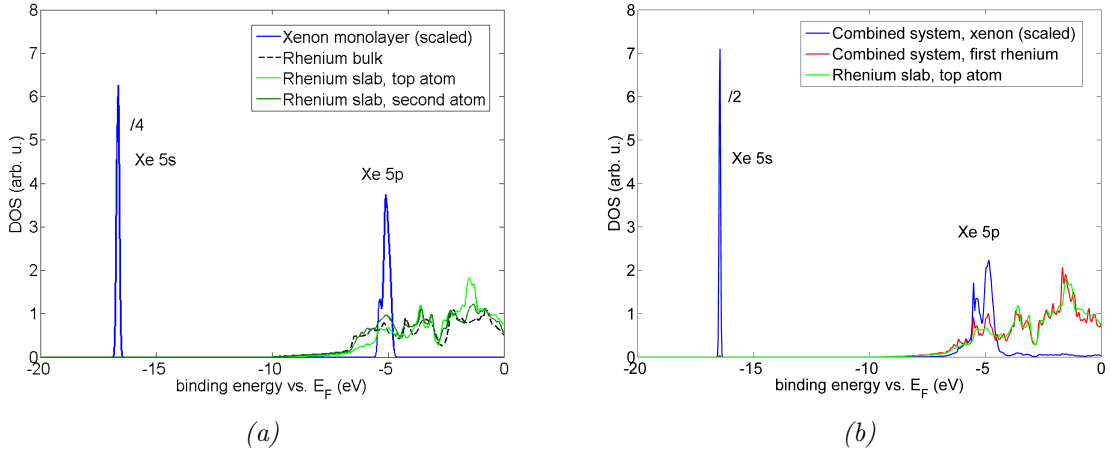


Figure 6.15.: Calculated density of states of an isolated xenon monolayer and a rhenium slab (a) and of the combined system (b).

of the xenon electron distribution is perturbed. Although all these effects have only a very weak effect on the overall valence electron distribution, the DOS of the combined system is significantly altered, as displayed in figure 6.15 (b). The xenon states are downshifted, which is a consequence of the equalisation of the Fermi levels. The $5p$ states are significantly broadened to almost 1.5 eV, they are polarised by the metal surface and form the van-der-Waals bond with the substrate. The DOS of the topmost rhenium atom displays a lot of oscillations, indicative of a strong modification of the valence bands. Although the main features of the isolated system are reproduced, the behaviour deviates from the clean system in the region where the states of the two atoms overlap. As DFT is not able to exactly reproduce the van-der-Waals interaction, details of the calculation parameters are known to slightly modify the obtained simulation results. Still, the qualitative behaviour was found to be correct [91], and the simulations can be used to evaluate the interaction between the rare-gas overlayer and the metal substrate. The calculation shows that the valence bands are significantly modified by the Xe-Re interaction and that using these states to draw conclusions on the clean system is not trivial. The core states are not perturbed by the bonding mechanism, their energy levels remain the same. In a first approximation, measurements on the combined system can therefore be used directly to characterise the timing of the core states.

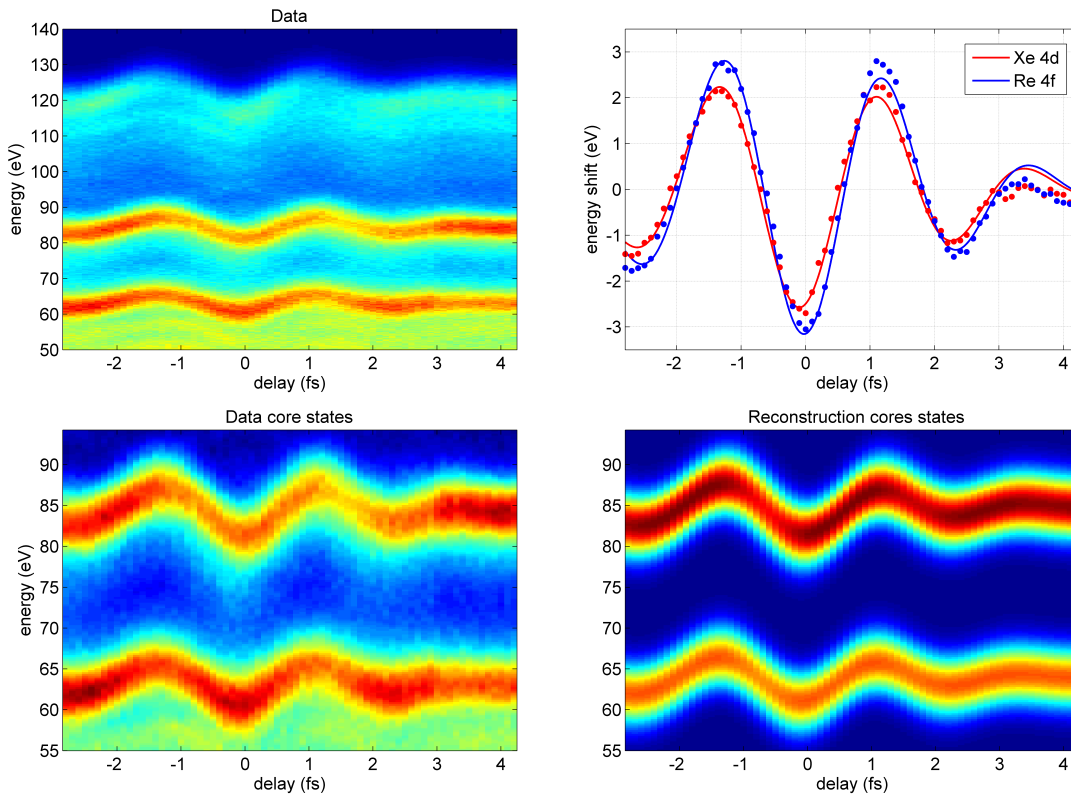


Figure 6.16.: Measured spectrogram displaying all electronic states and peak fit of the Re and Xe core states (upper panel) at an XUV energy of $E_C = 129.5$ eV, $\Delta_E = 5.6$ eV. Data and reconstruction of the core states (lower panel).

6.3.2. Measurements of the absolute delay

Figure 6.16 shows a complete spectrogram of the combined system recorded at an XUV energy of $E_C = 129.5$ eV, $\Delta_E = 5.6$ eV. The integration time per delay step was 30 s, the delay between the XUV and NIR pulses was varied in steps of 100 as, the sample was cooled down to 40 K after preparing the Xe monolayer. Three peaks, xenon 4d, rhenium 4f, and conduction band, are clearly resolved during the whole measurement. The fringes between the conduction band and the Re core state are due to XUV satellites caused by side-peaks of the multilayer mirror. These fringes cannot be seen in the measurements on clean Re because of the smaller cross section of the conduction band electrons [84]. The Xe 4d count rate is comparable to the Re 4f peak (including the background) and does not change during the measurement. Reasonable streaking amplitudes of $\approx \pm 0.5$ eV to \approx

± 3 eV could be achieved (corresponding to a NIR intensity of ≈ 30 to $\approx 600 \cdot 10^9$ W/cm²), at higher intensities, the Xe $4d$ states get obscured by ATI electrons. The Xe layer was found to be stable also at intensities larger than $600 \cdot 10^9$ W/cm².

The conduction band of the combined system displays a large apparent chirp, resulting from the overlap of the rhenium and xenon states. As displayed in figure 6.15, the xenon $5p$ state lies at the lower edge of the rhenium conduction band. The two peaks overlap in the photoelectron spectrum due to the bandwidth of the XUV. Any temporal shift between those two is still visible as an asymmetry in the streaking trace. The core states are well separated and carry a slight positive chirp, similar to the uncovered rhenium crystal measured at the same XUV photon energy. The xenon core states display an additional asymmetry, the trace gets broader at low kinetic energies. The FWHM of the peak fitting routine using a gaussian on a second-order polynomial background oscillates between 5 eV to 6.5 eV. This broadening is symmetric with respect to the maxima and minima of the oscillating streaking trace and cannot be attributed to a chirp. The reason of this broadening is so far unclear.

To extract the timing between the referencing level and the substrate, only the core states are used. The valence states can in principle be disentangled by fixing the energy levels to the ones of the isolated systems, uncovered rhenium and a multilayer of xenon respectively. Any chemical shift introduced by the physisorption of the rare gas on the metal substrate is too small to be relevant in this context here. However, the analysis turns out to be inaccurate due to the satellite peaks of the XUV mirror. Additionally, the changed DOS does not allow for a direct comparison with the clean metal system. Therefore, we restrict our discussion to the core states. The results of a gaussian fit on a second-order polynomial and of the spectrogram retrieval are displayed in the top right and in the lower panel of figure 6.16. Both methods reproduce the overall behaviour of traces very well. The intensity of the Xe $4d$ peak returned by the retrieval is too low compared to the shown measured dataset, the same behaviour can be observed with other datasets as well. The reason for this is not clear, probably it is a result of the increased ATI background. The extracted time delay is insensitive to the background, the results obtained with the retrieval algorithm agree very well with results of peak fits, which partly include the background.

The timing between the Xe $4d$ and Re $4f$ states was found to be 63 ± 2 as, the xenon atoms are first. The error is the statistical error of the fitting algorithm of the retrieval. A direct comparison to the delay between conduction band and $4f$ states in the

uncovered Re crystal of 86 as would indicate that the Xe core state is emitted after the Re conduction band. This comparison is invalid as it does not account for the inelastic mean free path of the rhenium electrons. The IMFP in solid Xe calculated with the TPP-2 formula is on the order of 4.5 \AA at 60 eV, similar to the IMFP in Re at 85 eV. The influence of the changed DOS was not considered here, as these values should only serve as an estimate of the order of magnitude. Additionally, it should be noted that the IMFP of Xe varies in literature between 3.65 and 17 \AA depending on the method it is obtained [92]. To be consistent with the rest of this thesis, the TPP-2 formula was used. The overlayer of xenon shifts the average escape depth of both rhenium electrons almost to the top layer of the substrate. This is supported by first results from analysis methods which include the conduction band region. It is found that the delay between the two rhenium states is significantly reduced compared to the clean metal, indicating that the transport in the substrate is less important.

This interpretation implies that xenon forms a dense layer where the rhenium electrons can scatter. The simulated $\sqrt{3} \times \sqrt{3} R(30)$ geometry contradicts this. The xenon atoms almost do not interact laterally due to their large separation. Therefore, a “residual” contribution to the delay due to transport in the rhenium crystal is highly probable.

The influence of the NIR streaking field has also be taken into account in a different way. The refractive index of solid xenon can be estimated to be on the order of 1.44 at 700 nm [93, 94], an estimate of the absorption could not be found. If the adsorbed xenon atoms are modeled as dielectric layer, the Fresnel equations can be applied in a first approximation to calculate the field strength. Taking into account the reflected and transmitted components at the vacuum-xenon and xenon-rhenium interface, $n_{Re} = 3.84 + 2.89i$ [47], the NIR field in the xenon layer is found to be on the order of 77% of the vacuum strength. The streaking therefore starts already at the xenon-rhenium interface. The time delay cannot be attributed to transport through the xenon layer.

To clarify the physical origin of this delay, additional measurements are necessary. The geometry of the rare gas layer has to be investigated to be able to estimate its influence on inelastic electron scattering. This influence can also be tested by using sub-monolayer coverages. The delay should increase with decreasing number of adsorbed atoms. Any “residual” transport in the rhenium substrate can be tested via angular resolution. An “inherent” time delay, which could be attributed to different electron correlations of the two different atoms like in the gas phase [95], should show no dependence on the angle of

detection, different surface orientations of the substrate should also give the same result.

These first experiments show that attosecond streaking of a combined system of a rare gas layer and a metal substrate is feasible. The stability of the layer allows for high quality measurements which result in a first estimate of the absolute timing of photoemission in solid state systems. Further work on the involved bonding and multi-electron interactions mechanisms are necessary to obtain a complete picture of the relevant processes.

7. Conclusions and outlook

Within this thesis, electronic transport effects following photoexcitation in various condensed matter systems were systematically investigated employing the streaking technique. To carry out these measurements, a novel, versatile experimental setup was designed and commissioned. The new beamline allows for high harmonic generation with a tuneable cut-off region, isolated attosecond pulses with central energies between 90 and 130 eV could be produced. This interval can still be extended by using different target gases and changing the focussing length of the NIR pulse.

In order to achieve UHV conditions necessary for photoelectron spectroscopy, an effective differential pumping scheme was devised, which is capable of maintaining a pressure gradient of 12 orders of magnitude between the harmonics' target and the solid state sample. Two loadlocks permit easy exchange of samples and XUV mirrors without breaking vacuum.

A sophisticated preparation system allows for cleaning the investigated solid state samples as well as for controlled layer growth of different materials. Standard techniques like LEED, thermal desorption, or XPS were incorporated to characterise the samples. Several electron detectors can be mounted to the beamline at the same time, the detector of interest is brought into the measuring position with a rotational feedthrough, this system offers angular resolution as well. A number of experimental conditions like NIR intensity, XUV flux, angle of incidence, angle of detection, or sample temperature can be varied easily during the experiment. A gas target is included for reference measurements.

Using this setup, it was demonstrated that the attosecond transient recorder is an excellent method to measure delayed photoemission in several condensed matter systems. As shown in chapter 6, the probing NIR pulse is not affecting the measured time delay in metal single crystal. An influence of the probing pulse on the investigated system could have been possible due to the large penetration depth of more than 100 Å of the laser field in the metal sample [11] and, in particular, the unknown exact field strength and polarisation direction in the first few atomic layers of the system [86, 87]. The

System XUV energy	W(110)			Re(0001)		
	measured	calculated		measured	calculated	
		classical	DFT		classical	DFT
93 eV	78 ± 10 as	42 – 47 as	57 – 94 as	124 ± 36 as	54 as	78 – 308 as
122 eV	44 ± 3 as	12 – 13 as	6 – 35 as	–	13 – 15 as	351 – 454 as
130 eV	22 ± 11 as	10 as	25 – 70 as	86 ± 8 as	11 – 12 as	186 – 245 as

Table 7.1.: Summary of measured and simulated time delays after photoexcitation between conduction band and 4f core state electrons in tungsten and rhenium. In all cases, the conduction band electrons escape earlier than the 4f electrons. The range of calculated delays is due to a variable acceptance angle of the electron detector in the calculation (see fig. 6.10 and 6.11). The XUV photon energies were rounded for this table.

measured time delay was found to be independent of the applied NIR intensity in a range of $100 - 600 \cdot 10^9 \text{W/cm}^2$. This establishes the streaking technique as the currently only method capable of resolving processes on a sub-femtosecond scale in real time.

Systematic investigation of the time delay between photoelectrons from metal single crystals reveals a significant dependence on both the XUV photon energy and the investigated material. The results are summarised in table 7.1. The dynamics responsible for this effect therefore neither rely solely on a material constant nor are exclusively dependent on the impinging XUV field. A possible influence of an overlap of the plasmon loss of the metal with one of the photoelectron peaks on the observed delay, as pointed out in [11], could be ruled out by comparing two different materials.

It can be shown that the measured delays as a function of XUV photon energy differ significantly from classical calculations. This indicates strongly that electron dynamics after photoexcitation should not be modelled as ballistic transport. Several theoretical models which explain the delay quantummechanically and rely on the different spatial extension of the initial state wavefunction [10, 9], include the influence of the XUV photon energy mainly via the electron IMFP. As the measured delays show a behaviour different from the IMFP, these models fail to explain the observed effect, and a considerable contribution of the final states to the observed dynamics is highly probable. A model

utilising DFT simulations of the investigated systems was employed in this thesis, which calculates electron transport in a high-lying band structure. The photoemission process is treated within the three-step-model [8], the observed delay is explained via different transport times and velocities of the photoelectrons in the sample. This model is able to explain the results obtained on tungsten, but fails in case of rhenium (see table 7.1). The reason for this is not clear, it cannot be excluded that the DFT calculations show some inaccuracy. We propose therefore to use tungsten single crystals with different surface orientations to test the influence of final states on the delay. Any masking of the underlying physics due to different XUV pulse properties or different electron escape depths can be fully excluded this way. Furthermore, the band structure calculations can be easily tested.

Additional information can be gained if the detection angle is varied: The calculated DFT results predict a strong modification of the delay depending on the acceptance angle of the detector. Although this angle cannot be modified, the direction of detection can provide access to this angular dependence. If the acceptance angle of the TOF detector is approximated with $\pm 12^\circ$, a variation of the detection angle $\pm 20^\circ$ with respect to the surface normal should enable one to capture an angular dependence of the delay. In case of an angle of 20° to the surface normal, the longitudinal component of the NIR streaking field pointing along the detector axis is less than 7% of the complete field and can therefore be expected not to have a significant influence on the result and can still be neglected.

Still, any influence of the NIR pulse on the electronic structure of the investigated system cannot be fully excluded without additional measurements. The conduction band states might get modified by the strong electrical field of the few-cycle laser pulse. This modification should manifest itself in a broadening of the photoelectron peak depending on the intensity of the NIR pulse different from the broadening of the core electron signal. Reference measurements done in the gas phase can be used to characterise the core state peaks, contributions due to propagation in the material can be excluded this way. A systematic investigation of line shape and chirp of the conduction band electron wave packets as a function of NIR intensity can then provide insight into NIR-dependent modifications of the system.

All streaking measurements in this thesis were done in a parallel geometry, where the laser electrical field and the electron detector are aligned along the same axis. This results in the strongest modulation of the photoelectrons' kinetic energy and enables to

neglect the influence of the NIR streaking field inside the solid. In case the polarisation of the NIR (and accordingly of the XUV pulse) is rotated by 90° , the effect of the NIR field on the photoelectrons has to be taken into account already inside the sample, at the instant electrons are excited by the XUV pulse. Comparing those results with measurements from this thesis offers an insight into the excitation time and escape depth of the photoelectrons. In this orthogonal geometry, the modulation of the kinetic energy governed by the acceptance angle of the electron detector, the timing information is encoded in the width of the photoelectron peaks.

Another approach of quantifying the electronic transport effect is to investigate the emission time delay in systems which have a controlled thickness. Controlled layer growth of an adsorbate allows for artificially controlling the escape depth of photoelectrons. This was pursued in the PhD-work of S. Neppl, details will be given there.

In a second type of experiment, the absolute emission time of photoelectrons could be referenced to a signal originating from a monolayer of a rare gas adsorbed on top of the investigated metallic substrate. A proof-of-concept experiment carried out on Xe adsorbed on Re demonstrated that high-quality streaking data can be obtained from such a system. The delay between Xe $4d$ and Re $4f$ states was found to be 63 ± 2 as at an XUV photon energy of 129.5 eV, where the Xe electrons escape first.

So far, only the timing between core states can be accurately measured because the valence states cannot be resolved energetically. Additionally, DFT calculations indicate electronic mixing of the valence states of substrate and adlayer. In order to quantify the influence of the van-der-Waals binding on the two sub-systems, high-resolution synchrotron measurements have to be carried out. The exact adsorption sites of the adsorbate atoms have to be investigated with electron diffraction methods in order to be able to simulate the correct geometry. These measurements are necessary to completely characterise the investigated system. Additional streaking measurements with varying NIR intensity yield information on the influence of the probing pulse on the investigated combined system of a rare gas monolayer on a metal single crystal substrate.

In summary, measurements with attosecond resolution in real-time provide valuable insight into elementary electronic response processes which were accessible only indirectly so far. In near future, streaking measurements, which were shown to be an excellent method to probe ultrafast electronic processes in condensed matter systems, will answer basic questions not only on electronic transport but also on the rise time of charge screening, the time scale of electron transfer between two strongly coupled systems, or

the duration of plasmon formation. Having these answers at hand will lead to a deeper understanding of condensed matter physics and on the long term will also drive industrial applications operating at the single electron limit.

A. TOF detector calibration

The data presented in this thesis were recorded with a time-of-flight detector (TOF), which collects data in the time domain. In the simplest case of a detector without any accelerating electrical fields the conversion to kinetic energy (in eV) is done via

$$E_{kin0} = \frac{m}{2e} v^2 = \frac{m}{2e} \frac{d^2}{t^2}. \quad (\text{A.1})$$

The driftlength d is usually determined by detecting Auger lines because their energies do not depend on the excitation energy and can be looked up in reference tables. However, the TOF detector which was used for the present work exhibits a post-acceleration stage, where a high voltage of 2.4 kV is applied over a distance of 7 cm to accelerate electrons on the multi-channel-plate detector. This post-acceleration stage artificially alters the apparent driftlength of the electrons depending on their initial kinetic energy. The apparent length of the post-acceleration stage differs by 2 cm for 50 and 130 eV electrons, if the stage is modeled as a plane-parallel capacitor. This leads to distortions of the initial conversion between time and energy. The effect is even larger, if the electrostatic lens of the detector is employed to enhance the signal within a certain energy window. In order to get a proper conversion relation between time and energy, results of simulated electron trajectories inside the TOF detector (SIMION [96] results provided by the manufacturer) were used to correct equation (A.1). The deviation between actual kinetic energy and calculated kinetic energy was put into an additional term E_{shift} which depends on the lens voltage $lensV$ and on the non-corrected kinetic energy. This shift was then subtracted from the non-corrected energy relation.

$$E_{kin} = \frac{m}{2e} \frac{d^2}{t^2} - E_{shift}(lensV, E_{kin0}(d, t)) \quad (\text{A.2})$$

Examples of E_{shift} for different lens voltages are displayed in figure (A.1). With this method, the true driftlength is not known exactly. The assumed distance is irrelevant because any deviations are compensated with E_{shift} . The agreement between spectra

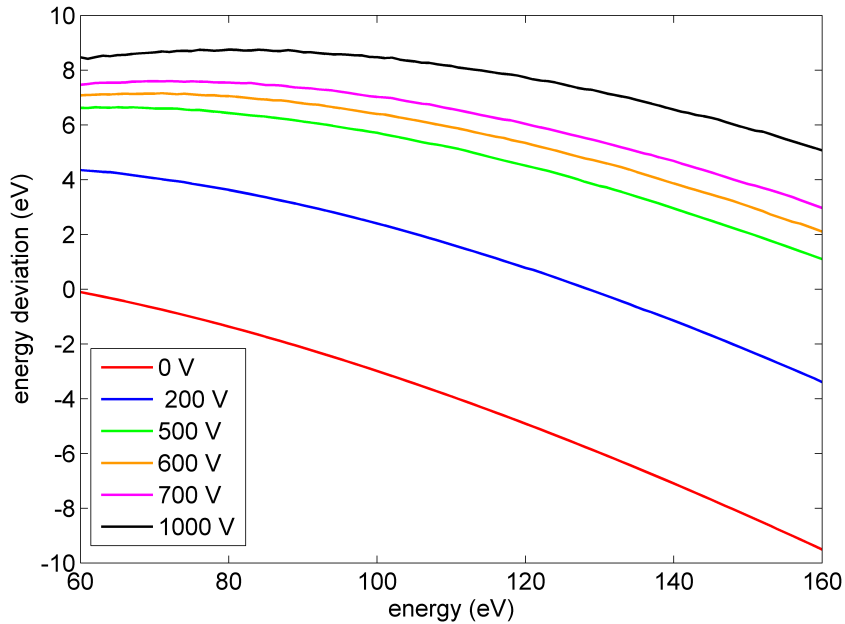


Figure A.1.: Simulated deviations of the calculated kinetic energy from its actual value for different lens voltages.

recorded without lens and with lens is sufficiently good, leading to deviations of peak positions with and without lens of less than 1 eV.

Once the conversion to kinetic energy is done, the amplitudes of the data points have to be scaled according to the conversion function. The absolute inverse of the first time derivative of equation (A.2) is used as the scaling factor. Figure (A.2) shows raw data and energy converted and scaled data of a clean W(110) sample recorded with an 4 eV broad XUV pulse at 130.8 eV, no lens was used to collect this dataset. Comparisons to synchrotron measurements (see figure 6.3) show also good agreement.

As mentioned above, the electrostatic lens enhances the electron signal only in a certain window, depending on the applied lens voltage. The enhancement over this window is usually not uniform. Especially at the edges peaks might get distorted. The spectra have therefore be corrected for this transmission function. The transmission was simulated using the electron trajectories obtained with SIMION. Figure A.3 shows the result at a lens voltage of 650 V. The red curve is the simulated transmission function. It displays an almost flat plateau between 70 and 140 eV with a linear rising edge at its low energy side

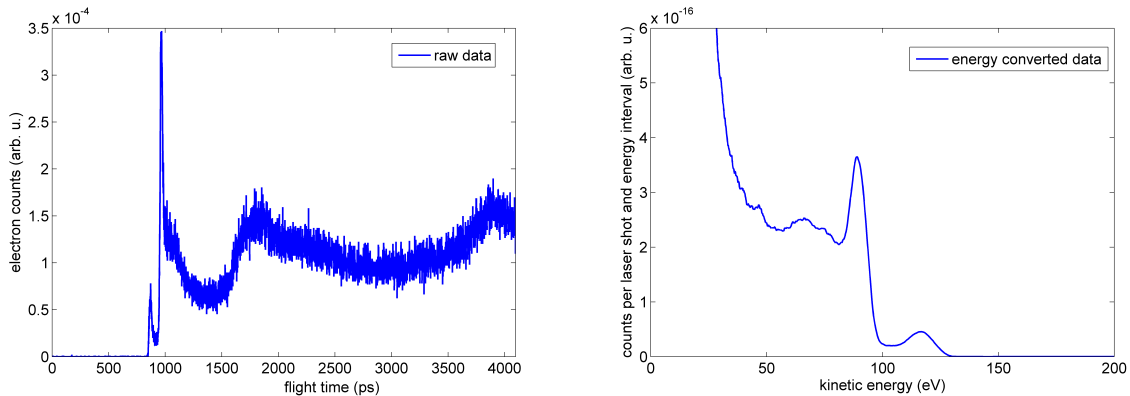


Figure A.2.: Raw and energy converted time-of-flight photoelectron spectra of clean W(110).

and an exponentially decaying falling edge at its high energy side. The steep cut-offs at 60 and 160 eV indicate the boundaries of the simulation. The black curve is a measured transmission function, using a W(110) sample. The green curve is a gaussian fit of the simulated transmission function. All graphs are normalised to their maximum value to make comparison easier.

Figure A.3 shows a W(110) spectrum corrected for with the simulated transmission function and its gaussian fit discussed above. The light blue spectrum was recorded with a lens voltage of 650 V, no corrections for the transmission was made. The red graph was obtained using the simulated transmission function, and the green one using the fit of the simulated transmission function. A reference spectrum recorded without lens is plotted in black. All graphs are normalised to the maximum of the $4f$ peak. The red graph obtained with the simulated transmission function displays a too weak conduction band, and the peak is slightly too low in energy. The plateau of the transmission function has a small positive slope, resulting in a downscaling of the high energy peaks. The conduction band of the green curve, where the gaussian fit of the simulated function was used, is still slightly too weak, but the peak positions of both $4f$ and conduction band states match the spectrum without lens within an interval of less than 0.8 eV. This fit seems to be the most accurate model of the transmission function.

To further analyse this approach, streaking spectrograms were compared using no transmission function and the last fit discussed above. In figure (A.4), the same spectrogram of W(110) is plotted using no transmission function (a), and the fitted

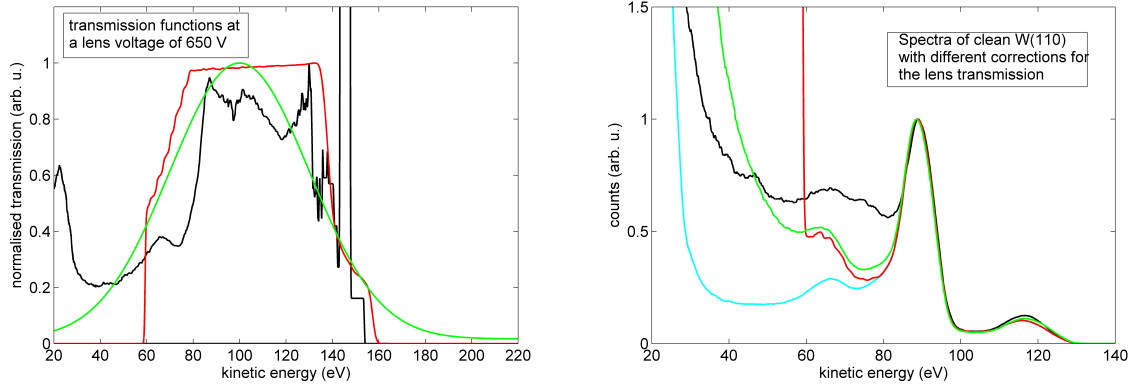


Figure A.3.: Simulated, calculated and measured transmission functions, and photoelectron spectra of clean $W(110)$ with different transmission functions applied.

simulated one (b). No distortion of the peaks can be identified by eye in the left hand figure. The conduction band in the right hand figure is stronger than in the uncorrected dataset because the weaker enhancement of the lens in that region is compensated by the transmission function. Figure A.4 (c-e) finally shows the shape of the NIR vector potential and the amplitude and width of the $4f$ and conduction band states of the above spectrograms. The graphs in the left panel were obtained fitting the peaks of the spectrogram without transmission function, the graphs in the right hand panel were obtained fitting the peaks of the spectrogram corrected for with the fitted simulated transmission function. If the window of the lens function was cutting the peaks in the left hand panel, the peak amplitude should oscillate in phase with the NIR vector potential. Both peak amplitudes however oscillate with the double frequency of the vector potential and show a correlation with the peak width. This change of amplitude and width is due to the streaking process, as was explained in chapter 2. If the transmission function is introduced, the overall behaviour stays the same, as displayed in the right hand panel. The quality of the fits increases slightly. The measured time delay turned out to be insensitive to the transmission functions. As the simulations extend only over a range of 60 to 160 eV and an extrapolation of the data did not provide any new information relevant for this work, no transmission function was included. However, the procedure described here is applicable whenever the peak shape is of interest.

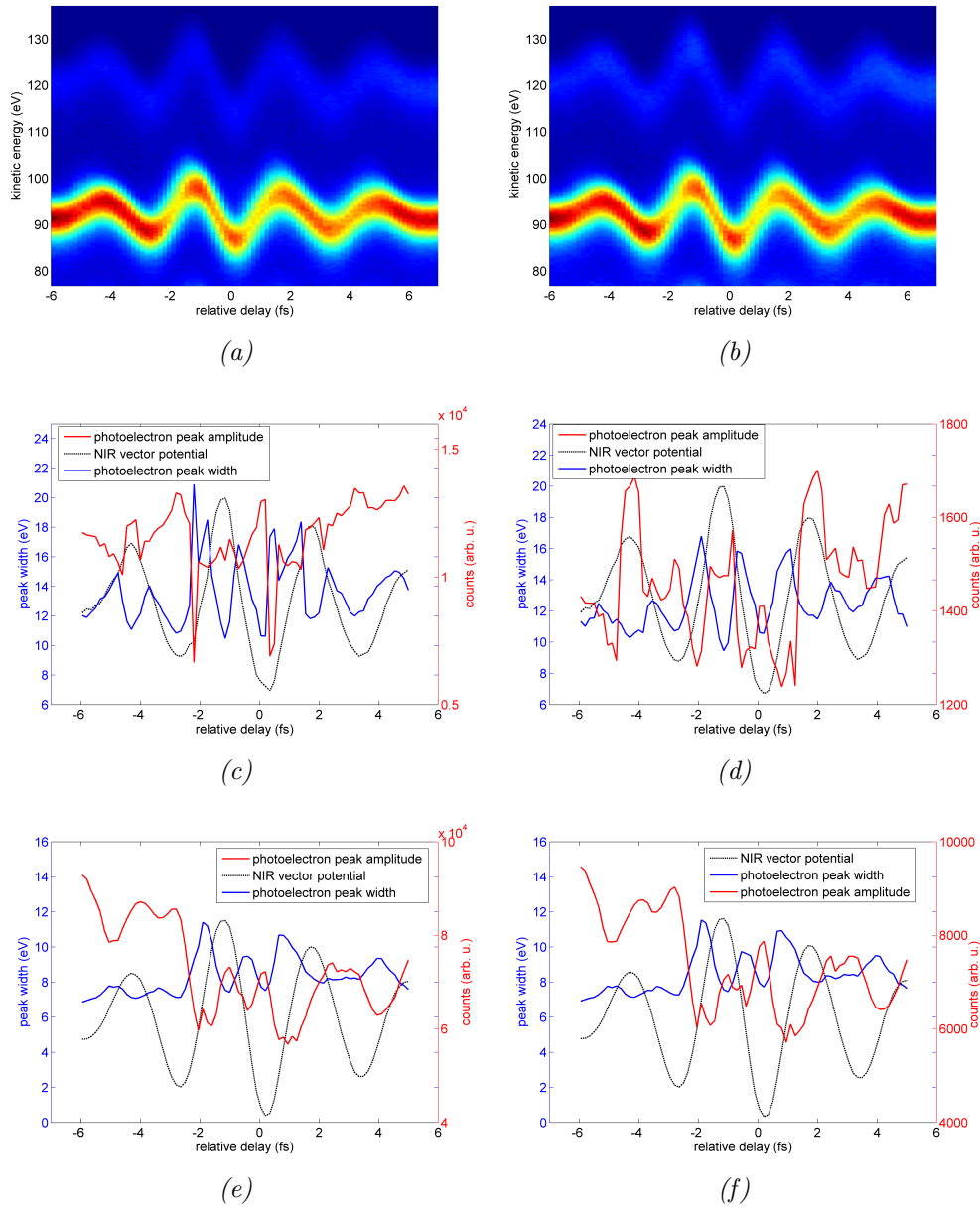


Figure A.4.: Spectrograms of clean $W(110)$ with different transmission functions applied: no transmission included (a), Gaussian fit of the simulated transmission function (b). Peak width and peak amplitude of the conduction band and $4f$ states of clean $W(110)$ using no transmission function (c, e) and a gaussian fit of the simulated transmission function (d, f)

B. XUV mirrors and filters

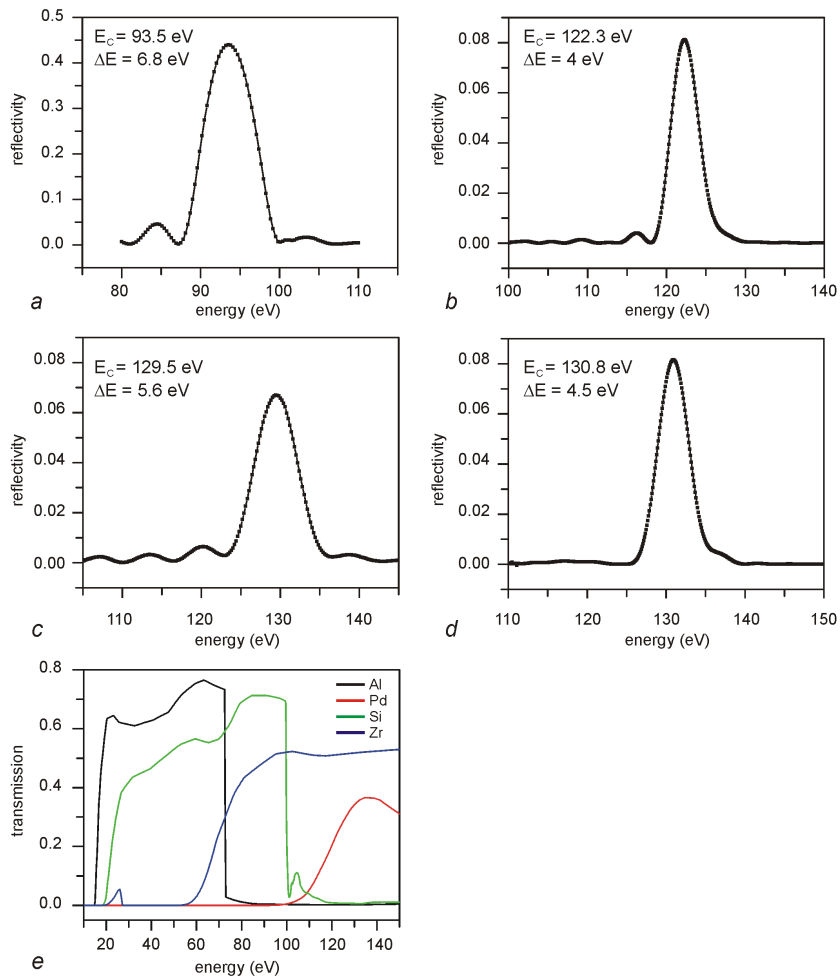


Figure B.1.: Design curves of used XUV mirrors (a - d, courtesy of M. Hofstetter), the central energy is denoted with E_C , the bandwidth with ΔE , and XUV transmission of metal foils (200 nm thickness each) (e).

Bibliography

- [1] URL http://nobelprize.org/nobel_prizes/chemistry/laureates/1999/...zewail-lecture.pdf.
- [2] E. Knoesel, A. Hotzel and M. Wolf. *Ultrafast dynamics of hot electrons and holes in copper: Excitation, energy relaxation, and transport effects*. Phys. Rev. B, **57**(20), 12812–12824 (1998).
- [3] A. Fohlisch, P. Feulner, F. Hennies, A. Fink, D. Menzel, D. Sanchez-Portal, P. Echenique and W. Wurth. *Direct observation of electron dynamics in the attosecond domain*. Nature, **436**(7049), 373–376 (2005).
- [4] A. Borisov, D. Sanchez-Portal, R. Muino and P. Echenique. *Building up the screening below the femtosecond scale*. Chem. Phys. Lett., **387**(1-3), 95–100 (2004).
- [5] R. Huber, F. Tauser, A. Brodschelm, M. Bichler, G. Abstreiter and A. Leitenstorfer. *How many-particle interactions develop after ultrafast excitation of an electron-hole plasma*. Nature, **414**(6861), 286–289 (2001).
- [6] J. Berakdar. *Publication in preparation*.
- [7] A. L. Cavalieri, N. Mueller, T. Uphues, V. S. Yakovlev, A. Baltuska, B. Horvath, B. Schmidt, L. Bluemel, R. Holzwarth, S. Hendel, M. Drescher, U. Kleineberg, P. M. Echenique, R. Kienberger, F. Krausz and U. Heinzmann. *Attosecond spectroscopy in condensed matter*. Nature, **449**(7165), 1029–1032 (2007).
- [8] C. N. Berglund and W. E. Spicer. *Photoemission studies of copper + silver - theory*. Phys. Rev. A, **136**(4A), 1030–& (1964).
- [9] A. K. Kazansky and P. M. Echenique. *One-Electron Model for the Electronic Response of Metal Surfaces to Subfemtosecond Photoexcitation*. Phys. Rev. Lett., **102**(17), 177401–177404 (2009).

- [10] C.-H. Zhang and U. Thumm. *Attosecond photoelectron spectroscopy of metal surfaces*. Phys. Rev. Lett., **102**(12), 123601–1 –123601–4 (2009).
- [11] C. Lemell, B. Solleder, K. Tokesi and J. Burgdoerfer. *Simulation of attosecond streaking of electrons emitted from a tungsten surface*. Phys. Rev. A, **79**(6), 062901–062907 (2009).
- [12] URL http://www.mpq.mpg.de/cms/mpq/en/news/press/archiv/2007/...07_10_25.html.
- [13] F. Krausz and M. Ivanov. *Attosecond physics*. Rev. Mod. Phys., **81**(1), 163–234 (2009).
- [14] M. Fiess. *submitted*. Rev. Sci. Instrum. (2010).
- [15] A. Einstein. *Über einen die Erzeugung und Verwandlung des Lichtes betreffenden heuristischen Gesichtspunkt*. Annalen der Physik, **322**, 132 (1905).
- [16] A. Zangwill. *Physics at Surfaces*. Cambridge University Press (1988).
- [17] S. Hüfner. *Photoelectron Spectroscopy*. Springer Verlag (1996).
- [18] C. J. Powell, A. Jablonski, S. Tanuma and D. R. Penn. *Effects of elastic and inelastic electron-scattering on quantitative surface-analyses by AES and XPS*. J. Electron. Spectrosc., **68**, 605–616 (1994).
- [19] P. Dirac. *The question theory of the emission and absorption of radiation*. P. R. Soc. Lond. A-Conta., **114**(767), 243–265 (1927).
- [20] G. D. Mahan. *Theory of photoemission in simple metals*. Phys. Rev. B, **2**(11), 4334–4350 (1970).
- [21] J. Pendry. *Theory of Photoemission*. Surf. Sci., **57**(2), 679–705 (1976).
- [22] S. Tanuma, C. Powell and D. Penn. *Calculations of electron inelastic mean free paths for 31 materials*. Surf. Interface Anal., **11**(11), 577–589 (1988).
- [23] S. Tanuma, C. Powell and D. Penn. *Calculations of electron inelastic mean free paths. 2. Data for 27 elements over the 500-2000-eV range*. Surf. Interface Anal., **17**(13), 911–926 (1991).

-
- [24] H. Lüth. *Surfaces and Interfaces of Solids*. Springer Verlag (1993).
- [25] P. J. Feibelman and D. E. Eastman. *Photoemission spectroscopy - correspondence between quantum-theory and experimental phenomenology*. Phys. Rev. B, **10**(12), 4932–4947 (1974).
- [26] P. Bruhwiler, O. Karis and N. Martensson. *Charge-transfer dynamics studied using resonant core spectroscopies*. Rev. Mod. Phys., **74**(3), 703–740 (2002).
- [27] J. Schnadt, P. Bruhwiler, L. Patthey, J. O’Shea, S. Sodergren, M. Odelius, R. Ahuja, O. Karis, M. Bassler, P. Persson, H. Siegbahn, S. Lunell and N. Martensson. *Experimental evidence for sub-3-fs charge transfer from an aromatic adsorbate to a semiconductor*. Nature, **418**(6898), 620–623 (2002).
- [28] H. Petek and S. Ogawa. *Femtosecond time-resolved two-photon photoemission studies of electron dynamics in metals*. Prog. Surf. Sci., **56**(4), 239–310 (1997).
- [29] M. Weinelt. *Time-resolved two-photon photoemission from metal surfaces*. J. Phys.-Condens. Mat., **14**(43), R1099 (2002).
- [30] P. Echenique and J. Pendry. *Existence and detection of Rydberg states at surfaces*. J. Phys. C solid state, **11**(10), 2065–2075 (1978).
- [31] I. Shumay, U. Hofer, U. Thomann, W. Wallauer and T. Fauster. *Lifetimes of image-potential states on Cu(100) and Ag(100) measured by femtosecond time-resolved two-photon photoemission*. Phys. Rev. B, **58**(20), 13974–13981 (1998).
- [32] H. Petek, M. Weida, H. Nagano and S. Ogawa. *Real-time observation of adsorbate atom motion above a metal surface*. Science, **288**(5470), 1402–1404 (2000).
- [33] URL <http://www.fhi-berlin.mpg.de/pc/electrondynamix/lab/2PPE.htm>.
- [34] E. Goulielmakis, M. Schultze, M. Hofstetter, V. S. Yakovlev, J. Gagnon, M. Uiberacker, A. L. Aquila, E. M. Gullikson, D. T. Attwood, R. Kienberger, F. Krausz and U. Kleineberg. *Single-cycle nonlinear optics*. Science, **320**(5883), 1614–1617 (2008).
- [35] F. Reiter, U. Graf, M. Schultze, W. Schweinberger, H. Schröder, N. Karpowicz, A. M. Azzeer, R. Kienberger, F. Krausz and E. Goulielmakis. *Generation of sub-3 fs pulses in the deep ultraviolet*. Opt. Lett., **35**(13), 2248–2250 (2010).

- [36] R. Kienberger, E. Goulielmakis, M. Uiberacker, A. Baltuska, V. Yakovlev, F. Bammer, A. Scrinzi, T. Westerwalbesloh, U. Kleineberg, U. Heinzmann, M. Drescher and F. Krausz. *Atomic transient recorder*. Nature, **427**(6977), 817–821 (2004).
- [37] L. Miaja-Avila, C. Lei, M. Aeschlimann, J. L. Gland, M. M. Murnane, H. C. Kapteyn and G. Saathoff. *Laser-assisted photoelectric effect from surfaces*. Phys. Rev. Lett., **97**(11), 113604–1 – 113604–4 (2006).
- [38] L. Miaja-Avila, G. Saathoff, S. Mathias, J. Yin, C. La-o vorakiat, M. Bauer, M. Aeschlimann, M. M. Murnane and H. C. Kapteyn. *Direct measurement of core-level relaxation dynamics on a surface-adsorbate system*. Phys. Rev. Lett., **101**(4), 046101–1 – 046101–4 (2008).
- [39] T. Gallagher. *Above-threshold ionization in low-frequency limit*. Phys. Rev. Lett., **61**(20), 2304–2307 (1988).
- [40] P. Corkum, N. Burnet and F. Brunel. *Above-threshold ionization in the long-wavelength limit*. Phys. Rev. Lett., **62**(11), 1259–1262 (1989).
- [41] J. Itatani, F. Quere, G. Yudin, M. Ivanov, F. Krausz and P. Corkum. *Attosecond streak camera*. Phys. Rev. Lett., **88**(17), 173903–173906 (2002).
- [42] M. Drescher, M. Hentschel, R. Kienberger, M. Uiberacker, V. Yakovlev, A. Scrinzi, T. Westerwalbesloh, U. Kleineberg, U. Heinzmann and F. Krausz. *Time-resolved atomic inner-shell spectroscopy*. Nature, **419**(6909), 803–807 (2002).
- [43] M. Kitzler, N. Milosevic, A. Scrinzi, F. Krausz and T. Brabec. *Quantum theory of attosecond XUV pulse measurement by laser dressed photoionization*. Phys. Rev. Lett., **88**(17), 173904–173907 (2002).
- [44] E. Goulielmakis, M. Uiberacker, R. Kienberger, A. Baltuska, V. Yakovlev, A. Scrinzi, T. Westerwalbesloh, U. Kleineberg, U. Heinzmann, M. Drescher and F. Krausz. *Direct measurement of light waves*. Science, **305**(5688), 1267–1269 (2004).
- [45] Y. Mairesse and F. Quere. *Frequency-resolved optical gating for complete reconstruction of attosecond bursts*. Phys. Rev. A, **71**(1), 011401–011404 (2005).

-
- [46] J. Gagnon, E. Goulielmakis and V. S. Yakovlev. *The accurate FROG characterization of attosecond pulses from streaking measurements*. Appl. Phys. B, **92**(1), 25–32 (2008).
- [47] E. Palik. *Handbook of Optical Constants*. Academic Press Inc (1991).
- [48] J. C. Baggesen and L. B. Madsen. *Theory for time-resolved measurements of laser-induced electron emission from metal surfaces*. Phys. Rev. A, **78**(3), 032903–032909 (2008).
- [49] E. Granados, D. W. Coutts and D. J. Spence. *Mode-locked deep ultraviolet Ce:LiCAF laser*. Opt. Lett., **34**(11), 1660–1662 (2009).
- [50] URL http://upload.wikimedia.org/wikipedia/commons/4/48/...Commercial_laser_lines.svg.
- [51] A. L. Cavalieri, E. Goulielmakis, B. Horvath, W. Helml, M. Schultze, M. Fiess, V. Pervak, L. Veisz, V. S. Yakovlev, M. Uiberacker, A. Apolonski, F. Krausz and R. Kienberger. *Intense 1.5-cycle near infrared laser waveforms and their use for the generation of ultra-broadband soft-x-ray harmonic continua*. N. J. Phys., **9**, 242–253 (2007).
- [52] J. Seres, E. Seres, A. Verhoef, G. Tempea, C. Strellil, P. Wobrauschek, V. Yakovlev, A. Scrinzi, C. Spielmann and F. Krausz. *Source of coherent kiloelectronvolt X-rays*. Nature, **433**(7026), 596 (2005).
- [53] P. Corkum. *Plasma perspective on strong-field multiphoton ionization*. Phys. Rev. Lett., **71**(13), 1994–1997 (1993).
- [54] M. Lewenstein, P. Balcou, M. Ivanov, A. LHuillier and P. Corkum. *Theory of high-harmonic generation by low-frequency laser fields*. Phys. Rev. A, **49**(3), 2117–2132 (1994).
- [55] A. de Bohan, B. Piraux, L. Ponce, R. Taieb, V. Veniard and A. Maquet. *Direct and indirect pathways in strong field atomic ionization dynamics*. Phys. Rev. Lett., **89**(11), 113002–113005 (2002).
- [56] A. de Bohan, P. Antoine, D. Milosevic and B. Piraux. *Phase-dependent harmonic emission with ultrashort laser pulses*. Phys. Rev. Lett., **81**(9), 1837–1840 (1998).

- [57] A. Baltuska, T. Udem, M. Uiberacker, M. Hentschel, E. Goulielmakis, C. Gohle, R. Holzwarth, V. Yakovlev, A. Scrinzi, T. Hansch and F. Krausz. *Attosecond control of electronic processes by intense light fields*. Nature, **421**(6923), 611–615 (2003).
- [58] E. Constant, D. Garzella, P. Breger, E. Mevel, C. Dorrer, C. Le Blanc, F. Salin and P. Agostini. *Optimizing high harmonic generation in absorbing gases: Model and experiment*. Phys. Rev. Lett., **82**(8), 1668–1671 (1999).
- [59] G. Tempea, M. Geissler, M. Schnurer and T. Brabec. *Self-phase-matched high harmonic generation*. Phys. Rev. Lett., **84**(19), 4329–4332 (2000).
- [60] B. Horvath. *Generation, characterization and sub-cycle shaping of intense, few-cycle light waveforms for attosecond spectroscopy*. Ph.D. thesis, Ludwig-Maximilians Universität München (2009).
- [61] S. Planas, N. Mansur, C. Cruz and H. Fragnito. *Spectral narrowing in the propagation of chirped pulses in single-mode fibers*. Opt. Lett., **18**(9), 699–701 (1993).
- [62] R. Shelton, L. Ma, H. Kapteyn, M. Murnane, J. Hall and J. Ye. *Phase-coherent optical pulse synthesis from separate femtosecond lasers*. Science, **293**(5533), 1286–1289 (2001).
- [63] T. Fuji, J. Rauschenberger, A. Apolonski, V. Yakovlev, G. Tempea, T. Udem, C. Gohle, T. Hansch, W. Lehnert, M. Scherer and F. Krausz. *Monolithic carrier-envelope phase-stabilization scheme*. Opt. Lett., **30**(3), 332–334 (2005).
- [64] L. Xu, C. Spielmann, A. Poppe, T. Brabec, F. Krausz and T. Hansch. *Route to phase control of ultrashort light pulses*. Opt. Lett., **21**(24), 2008–2010 (1996).
- [65] M. Uiberacker, T. Uphues, M. Schultze, A. J. Verhoef, V. Yakovlev, M. F. Kling, J. Rauschenberger, N. M. Kabachnik, H. Schroeder, M. Lezius, K. L. Kompa, H. G. Muller, M. J. J. Vrakking, S. Hendel, U. Kleineberg, U. Heinzmann, M. Drescher and F. Krausz. *Attosecond real-time observation of electron tunnelling in atoms*. Nature, **446**(7136), 627–632 (2007).
- [66] E. Magerl, S. Neppl, A. L. Cavalieri, B. E., S. M., T. Uphues, M. Hofstetter, U. Kleineberg, B. J.V., D. Menzel, F. Krausz, R. Ernstorfer, R. Kienberger and

-
- P. Feulner. *A flexible apparatus for attosecond photoelectron spectroscopy of solids and surfaces*. submitted to Review of Scientific Instruments (2011).
- [67] N. Nakano, H. Kuroda, T. Kita and T. Harada. *Development of a flat-field grazing-incidence XUV spectrometer and its application in picosecond XUV spectroscopy*. Appl. Opt., **23**(14), 2386–2392 (1984).
- [68] T. Kita, T. Harada, N. Nakano and H. Kuroda. *Mechanically ruled aberration-corrected concave gratings for a flat-field grazing-incidence spectrograph*. Appl. Opt., **22**(4), 512–513 (1983).
- [69] M. Hofstetter. *Publication in preparation*.
- [70] M. Wutz. *Handbuch Vakuumtechnik: Theorie und Praxis*. Vieweg und Teubner Verlag (2006).
- [71] P. Blaha, K. Schwarz, G. Madsen, K. D and J. Luitz. *WIEN2k, An Augmented Plane Wave + Local Orbitals Program for Calculating Crystal Properties*. Technische Universität Wien, Austria (2001).
- [72] S. Cottenier. *Density Functional Theory and the family of (L)APW-methods: a step-by-step introduction*. Instituut voor Kern- en Stralingsfysica, K.U.Leuven, Belgium) (2002). URL http://www.wien2k.at/reg_user/textbooks.
- [73] P. Hohenberg and W. Kohn. *Inhomogeneous electron gas*. Phys. Rev., **136**(3B), B864–B871 (1964).
- [74] J. Perdew, K. Burke and M. Ernzerhof. *Generalized gradient approximation made simple*. Phys. Rev. Lett., **77**(18), 3865–3868 (1996).
- [75] N. Smith. *Inverse photoemission*. Rep. Prog. Phys., **51**(9), 1227–1294 (1988).
- [76] D. R. Lide (editor). *CRC Handbook of Chemistry and Physics*. Taylor & Francis (2009).
- [77] J. F. Moulder, W. F. Stickle, P. E. Sobol and K. D. Bomben. *Handbook of x-ray photoelectron spectroscopy*. Perkin-Elmer Corp. (1992).
- [78] URL <http://surfexp.fhi-berlin.mpg.de/SXinput.html>.

- [79] M. Bode, S. Krause, L. Berbil-Bautista, S. Heinze and R. Wiesendanger. *On the preparation and electronic properties of clean W(110) surfaces*. Surf. Sci., **601**(16), 3308–3314 (2007).
- [80] R. Musket, W. McLean, C. Colmenares, D. Makowiecki and W. Siekhaus. *Preparation of atomically clean surfaces of selected elements - a review*. Applic. surf. sci., **10**(2), 143–207 (1982).
- [81] T. Engel and R. Gomer. *Adsorption of inert gases on tungsten - measurements on single crystal planes*. J. Chem. Phys., **52**(11), 5572–& (1970).
- [82] K. Ishizuka. *Field emission microscopic observations of the adsorption of oxygen, nitrogen, hydrogen, carbon monoxide and xenon on rhenium*. J. Res. Inst. Catalysis, Hokkaido Univ., **15**, 95–110 (1967).
- [83] D. Shirley. *High-resolution X-ray photoemission spectrum of valence bands of gold*. Phys. Rev. B, **5**(12), 4709–4714 (1972).
- [84] J. Yeh and I. Lindau. *Atomic subshell photoionization cross-sections and asymmetry parameters - 1- Z - 103*. Atom. data nucl. data, **32**(1), 1–155 (1985).
- [85] N. Christensen and B. Feuerbacher. *Volume and surface photoemission from tungsten. 1. Calculation of band-structure and emission-spectra*. Phys. Rev. B, **10**(6), 2349–2372 (1974).
- [86] A. Georges. *Calculation of surface electromagnetic fields in laser-metal surface interaction*. Opt. Commun., **188**(5-6), 321–331 (2001).
- [87] P. Feibelman. *Microscopic calculations of electromagnetic-fields in refraction at a jellium-vacuum interface*. Phys. Rev. B, **12**(4), 1319–1336 (1975).
- [88] B. Narloch and D. Menzel. *Structural evidence for chemical contributions in the bonding of the heavy rare gases on a close-packed transition metal surface: Xe and Kr on Ru (001)*. Chem. Phys. Lett., **270**(1-2), 163–168 (1997).
- [89] P. Bagus, V. Staemmler and C. Woll. *Exchangelike effects for closed-shell adsorbates: Interface dipole and work function*. Phys. Rev. Lett., **89**(9), 096104–1 –096104–4 (2002).

-
- [90] R. Diehl, T. Seyller, M. Caragiu, G. Leatherman, N. Ferralis, K. Pussi, P. Kaukasoina and M. Lindroos. *The adsorption sites of rare gases on metallic surfaces: a review*. J. Phys.-Condens. Mat., **16**(29, Sp. Iss. SI), S2839–S2862 (2004).
- [91] M. Springborg. *Structural and electronic properties of Xe*. J. Phys.-Condens. Mat., **12**(48), 9869–9883 (2000).
- [92] F. Amar, J. Smaby and T. Preston. *Simulating the photoelectron spectra of rare-gas clusters*. J. Chem. Phys., **122**(24), 244717 – 244724 (2005).
- [93] J. Phillips. *Ultraviolet absorption of insulators .4. Rare-gas solids*. Phys. Rev., **136**(6A), 1714–1721 (1964).
- [94] A. Hitachi, V. Chepel, M. Lopes and V. Solovov. *New approach to the calculation of the refractive index of liquid and solid xenon*. J. Chem. Phys., **123**(23), 234508–234513 (2005).
- [95] M. Schultze, M. Fiess, N. Karpowicz, J. Gagnon, M. Korbman, M. Hofstetter, S. Neppl, A. L. Cavalieri, Y. Komninos, T. Mercouris, C. A. Nicolaides, R. Pazourek, S. Nagele, J. Feist, J. Burgdoerfer, A. M. Azzeer, R. Ernstorfer, R. Kienberger, U. Kleineberg, E. Goulielmakis, F. Krausz and V. S. Yakovlev. *Delay in Photoemission*. Science, **328**(5986), 1658–1662 (2010).
- [96] D. Dahl. *SIMION for the personal computer in reflection*. Int. J. Mass Spectrom., **200**, 3 (2000).

Data archiving

The raw data used for obtaining the results can be found on the Data Archive Server (DAS) at the Max Planck Institute for Quantum Optics, Division for Attosecond Physics. Here, the utilised source files and MATLAB routines are listed according to the displayed figures in this thesis. The MATLAB routines are commented wherever the code is not self-explanatory.

Figure 4.4

High Harmonic Spectrum (from logbook 11.2.2009)

data	<code>raw_data\HHG_spec\XUV_spectrum.dat</code> <code>raw_data\HHG_spec\Zr_950nm.txt</code>
routine	<code>Matlab\HHGspectrum.m</code>

Reflectivity curve of grating from Hitachi:

`raw_data\HHG_spec\Hitachi_GratingSpecs.pdf`

Figure 5.1

Synthetically generated spectrograms and COM fits

data	<code>raw_data\Synthetic_Data\delay_au.txt</code> <code>raw_data\Synthetic_Data\lin_energy_axis_au.txt</code>
parameter file	<code>raw_data\Synthetic_Data\Parameters.m</code>
routine	<code>Matlab\Synthetic.m</code>

Figure 6.3

XUV only spectra of clean W(110)

data	<code>raw_data\W_spectrum\opt_spectrum_W2.asc</code> (taken on 100314)
------	--

	raw_data\W_spectrum\A944.txt (Bessy data)
parameter file	raw_data\scan_files\scan_100314 lensV = 0, smoothwidth = 21
routine	single_spec.m, read in second file manually

Figure 6.4

streaking of W(110), cuts at three different delaysteps

data	raw_data\100314\scan09
parameter file	raw_data\scan_files\scan_100314
routine	Matlab\Norm_Spectrogram.m

Figure 6.5

streaking of W(110) at different XUV energies

data	raw_data\090203\scan15
	raw_data\100219\scan22
	raw_data\100314\scan09
parameter file	raw_data\scan_files\scan_090203
	raw_data\scan_files\scan_100219
	raw_data\scan_files\scan_100314
routine	Matlab\Norm_Spectrogram.m
	Matlab\AS3_TOF_20100713.m

Figure 6.6laser vector potential fits from streaking of W(110)
same as 6.5**Figure 6.7**

XUV dependence of relative delay in W and Re

data	raw_data\090201\scan5
	raw_data\090203\scan13
	raw_data\090203\scan15 (W 90 eV)
data	raw_data\091216\scan07

```

raw_data\091216\scan08
raw_data\100219\scan21
raw_data\100219\scan22
raw_data\100220\scan12
raw_data\100220\scan28 (W 120 eV)
data raw_data\100314\scan09
raw_data\100315\scan09
raw_data\100315\scan25 (W 130 eV)
data raw_data\090420\scan03 (Re 90 eV)
raw_data\090610\scan05 (Re 130 eV)
parameter file raw_data\scan_files\scan_090201
raw_data\scan_files\scan_090203 (W 90 eV)
parameter file raw_data\scan_files\scan_091216
raw_data\scan_files\scan_100219
raw_data\scan_files\scan_100220 (W 120 eV)
parameter file raw_data\scan_files\scan_100314
raw_data\scan_files\scan_100315 (W 130 eV)
parameter file raw_data\scan_files\scan090420 (Re 90 eV)
raw_data\scan_files\scan_090610 (Re 130 eV)
routine Matlab\Norm_Spectrogram.m
Matlab\AS3_TOF_20100713.m

```

Figure 6.8

streaking and laser vector potential fits from streaking of Re(0001) at different XUV energies

```

data raw_data\090420\scan03
raw_data\090610\scan05
parameter file raw_data\scan_files\scan_090420
raw_data\scan_files\scan_090610
routine Matlab\Norm_Spectrogram.m
Matlab\AS3_TOF_20100713.m

```

Figure 6.9

Bandstructure and possible transitions in W(110)

```

data raw_data\Wien2k\W_solid5\W_solid.spaghetti_ene_100.txt

```

routine Matlab\BS_sampling.m

Figure 6.10

calculated delay in solid W along (110)

data raw_data\Wien2k\W_solid5\W_solid5_matlab.energy
 raw_data\Wien2k\W_solid5\W_solid5_matlab.klist
 raw_data\Wien2k\W_solid5\KPoint_Relation.txt
 raw_data\Wien2k\W_solid5\KPoint_Orig.txt
 routine Matlab\K_points_W_1405.m

Figure 6.11

calculated time delay in solid Re along (0001)

data raw_data\Wien2k\Re_solid\Re_solid_matlab.energy
 raw_data\Wien2k\Re_solid\Re_solid_matlab.klist
 routine Matlab\New_Kpoints_Re_0516.m

Figure 6.12

NIR dependence of relative delay in W
 same as figure 6.7, without Re data

Figure 6.13

Spectrum of Re with monolayer of Xe

data raw_data\090610\scan01 delaystep 51
 parameter file raw_data\scan_files\scan_090610
 routine Matlab\Norm_Spectrogram.m
 Matlab\AS3_TOF_20100713.m

Figure 6.14

valence e-density of Re, Xe

data raw_data\Wien2k\Re_7layers\01\super.rho
 raw_data\Wien2k\Re_7layers\01\header_super.rho
 raw_data\Wien2k\Xe_layer2\super.rho
 raw_data\Wien2k\Xe_layer2\header_super.rho
 raw_data\Wien2k\ReXe_7\super.rho
 raw_data\Wien2k\ReXe_7\header_super.rho
 routine Matlab\edensity_3files.m

Figure 6.15

DOS of Re, Xe

data	raw_data\Wien2k\Re_solid\Re_solid_dos1eV.txt
	raw_data\Wien2k\Re_7layers\01\super.dos1ev
	raw_data\Wien2k\Xe_layer2_dos1ev_orig.txt
	raw_data\Wien2k\ReXe_7\ReXe_7_dos1ev_orig.txt
routine	plot data with any program

Figure 6.16

streaking of Re/Xe system

data	raw_data\090610\scan03
parameter file	raw_data\scan_files\scan_090610
routine	Matlab\Norm_Spectrogram.m
	Matlab\AS3_TOF_20100713.m

Acknowledgments

The results presented in this thesis were made possible by the continuous effort of many people, and I will try to give all of them credit here.

Ferenc Krausz and Reinhard Kienberger provided the scientific environment at MPQ, Peter Feulner coordinated the work carried out at TUM. All three of them contributed to the scientific discussion with their remarkable experience.

The design and assembly of the AS3-beamline was an enormous project, there were a lot of people involved in all stages. Thorsten Uphues introduced me to CAD design and UHV techniques. Peter Feulner and Stefan Neppel devised the concepts of the UHV experimental and preparation chambers. The complete manipulator, temperature control, preparation and characterisation schemes were designed and provided by them. The double-mirror-stack was designed by Elisabeth Bothschafter and Ralph Ernstorfer. Hanns Peter Schönauer and Karl Eberle did the technical drawings of the experimental and preparation chambers. Tom Strobl and his team of the machine shop of MPQ manufactured most of the parts used in the beamline, they were indispensable especially whenever we were in need of instant replacement or repair of essential parts of the experimental setup. Michael Stanislawski did the programming of all necessary Labview routines.

During the measurements, the laser system was maintained by Adrian Cavaliere, Elisabeth Bothschafter, and Ralph Ernstorfer. Stefan Neppel took care of sample preparation and cleaning. Data collection was done by the complete team in various manning, the datapoints of tungsten at 130.8 eV were obtained by Elisabeth Bothschafter and Stefan Neppel.

All XUV-multilayer mirrors were designed and manufactured by Michael Hofstetter.

Markus Fiess, Oliver Herrwerth, and Adrian Wirth gave us technical support during beamtime whenever we were short on pellicle-filters, foils, heating tapes or other essential equipment.

Nick Karpowicz provided idea and code of the retrieval algorithm. Vladislav Yakovlev,

Justin Gagnon and Michael Korbman were helpful in discussions of possible methods of data analysis and their underlying physics.

Besides all persons mentioned above, Alexander Buck, Casey Chew Soo Hoon, Yunpei Deng, Mohammed Hassan, Patrick Heissler, Rainer Hörlein, Balint Horvath, Michael Jobst, Kiki Kosma, Lauryna Lötscher, Tom Metzger, Jens Osterhoff, Tim Paasch-Colberg, Alexander Schwarz, and Jasper Werhan gave me a good time.

Curriculum vitae

Personal data

Name	Elisabeth Veronika Magerl
Date and place of birth	January 17th 1981, Vienna, Austria
Citizenship	Austrian
Marital status	Single

Education

1991 – 1999	Secondary school in Vienna Graduation with distinction
1999 – 2006	Student at the Vienna University of Technology Branch of study: Technical physics Major field of study: Laser physics Diploma thesis at the institute of photonics: <i>Optical Spectroscopy of Single Self-Assembled Indium-Arsenide/ Gallium-Arsenide Quantum Dots</i> Supervisor: Prof. Karl Unterrainer
June 29th 2006	Graduation with distinction
Since November 2006	PhD student at the Max Planck Institute of Quantum Optics, Garching Supervisor: Prof. Ferenc Krausz
Since May 2007	Member of the International Max Planck Research School on Advanced Photon Science (IMPRS-APS)

Teaching

2001 – 2004	Teaching assistant in physics at the Vienna University of Technology
-------------	---

Working practice

July/August 2001	Trainee at Siemens AG Österreich Working field: Radiation patterns of patch antennas
August/September 2002	Trainee at Siemens AG Österreich Working field: Electromagnetic wave propagation at the surface of the human body for body-area networks
August/September 2003	Trainee at Siemens AG Österreich Working field: Electromagnetic wave guiding in common materials